nature communications

Article

https://doi.org/10.1038/s41467-023-43727-9

Flexible, scalable, high channel count stereo-electrode for recording in the human brain

Received: 30 December 2022

Accepted: 14 November 2023

Published online: 17 January 2024

Check for updates

Keundong Lee[1,10], Angelique C. Paulk[2,3,10], Yun Goo Ro[1,10], Daniel R. Cleary[1,4], Karen J. Tonsfeldt[1,5], Yoav Kfir[6,7], John S. Pezaris[6,7], Youngbin Tchoe[1], Jihwan Lee[1], Andrew M. Bourhis[1], Ritwik Vatsyayan[1], Joel R. Martin[1], Samantha M. Russman[1], Jimmy C. Yang[6,7], Amy Baohan[6,7], R. Mark Richardson[6,7], Ziv M. Williams[6,7], Shelley I. Fried[6,7], U. Hoi Sang[1], Ahmed M. Raslan[8], Sharona Ben-Haim[4], Eric Halgren[9], Sydney S. Cash[2,3] & Shadi. A. Dayeh[1] ✉

Over the past decade, stereotactically placed electrodes have become the gold standard for deep brain recording and stimulation for a wide variety of neurological and psychiatric diseases. Current electrodes, however, are limited in their spatial resolution and ability to record from small populations of neurons, let alone individual neurons. Here, we report on an innovative, customizable, monolithically integrated human-grade flexible depth electrode capable of recording from up to 128 channels and able to record at a depth of 10 cm in brain tissue. This thin, stylet-guided depth electrode is capable of recording local field potentials and single unit neuronal activity (action potentials), validated across species. This device represents an advance in manufacturing and design approaches which extends the capabilities of a mainstay technology in clinical neurology.

Brain disorders severely interfere with quality of life and can lead to major socioeconomic disparities[1,2]. A major therapeutic approach for a wide variety of neuropsychiatric diseases involves invasive recordings from both the cortex and subcortical structures and/or direct electrical neuromodulation of those structures. For treating medically intractable epilepsy, for example, it is commonplace for recordings to be made using stereotactically placed electrodes (sEEG or depth electrodes). Similarly, electrodes of this type are used to target the thalamus, substantia nigra and other subcortical structures for the control of seizures, Parkinson's disease, and essential tremor as well as a growing number of other disorders[3–13]. Future applications of these electrodes could be to understand memory disorders and assist in memory restoration[14–16] while other uses could be the development of brain computer interfaces to restore movement and communication in the setting of trauma, amyotrophic lateral sclerosis and stroke[17]. Electrodes of this type are implanted through small openings in the skull and penetrate the brain parenchyma at varying depths depending on the surgical target, and allow for subcortical recordings and, sulcal depth evaluation, with deep structural reach that is not attainable by surface electrodes. Currently, arrays of electrodes are hand-assembled 0.8–1.27 mm diameter cylinders comprised of 8–16 contacts each 1.5–5 mm in length.

[1]Integrated Electronics and Biointerfaces Laboratory, Department of Electrical and Computer Engineering, University of California San Diego, La Jolla, CA 92093, USA. [2]Department of Neurology, Harvard Medical School, Boston, MA 02114, USA. [3]Center for Neurotechnology and Neurorecovery, Department of Neurology, Massachusetts General Hospital, Boston, MA 02114, USA. [4]Department of Neurological Surgery, University of California San Diego, La Jolla, CA 92093, USA. [5]Department of Obstetrics, Gynecology, and Reproductive Sciences, Center for Reproductive Science and Medicine, University of California San Diego, La Jolla, CA 92093, USA. [6]Department of Neurosurgery, Harvard Medical School, Boston, MA 02114, USA. [7]Department of Neurosurgery, Massachusetts General Hospital, Boston, MA 02114, USA. [8]Department of Neurological Surgery, Oregon Health and Science University, Portland, OR 97239, USA. [9]Department of Radiology, University of California San Diego, La Jolla, CA 92093, USA. [10]These authors contributed equally: Keundong Lee, Angelique C. Paulk, Yun Goo Ro. ✉e-mail: sdayeh@ucsd.edu

The manufacture of clinical electrode arrays has only incrementally advanced since their initial development in the early 1950s because of the limitations in hand assembly and wiring of these implantable devices. In addition, the construction of these electrodes limits their spatial resolution; they are only able to record local field potentials (LFPs) over relatively large areas (e.g., multiple mm) and are unable to record from small, discrete neuronal populations, let alone individual neurons (e.g., action potential activity). A variety of modifications of this electrode have been used to record highly local sites in the brain. For example, platinum-iridium microwires extruding from the tip of depth electrodes enable recording of single and multi-unit activity from up to 9 microwires[18]. This configuration only allows recording from the tip. Dixi Medical has produced a depth electrode with extensible microwires from the body of the array (personal communication with Dixi Medical). Neither of these approaches allows more than a few channels to be recorded, neither afford grid-like high spatial resolution in that developing a spatial map of multiple action potential sites of origin is not possible, and the devices are still handmade. Other electrodes that can record single units from the human brain and afford high-resolution spatial mapping of single-cell activity include the Utah array[19] and Neuropixels[20,21] with up to hundreds of channels[22,23]. These devices, currently used in research, are limited by the silicon (Si) manufacturing technology and the brittleness of Si. They are also currently only able to access superficial cortical layers of the brain in humans, though there are advances in these devices enabling recording from deeper structures used in non-human primates[24].

To increase the spatial resolution and channel count of electrodes that can record from either the lateral gray matter or deep brain structures, recent engineering approaches have focused on rolling or adhering conformable and photolithographically defined polyimide electrodes around or on medical-grade tubing used in clinical depth electrodes[25–28]. Previous research has well-established the transformation of thin-film electrodes to depth electrodes and demonstrated successful high-quality recording chronically[27]. However, these hybrid integration approaches impose a limitation on the size of the electrode such that the starting diameter is pre-determined by the clinical depth electrode diameter.

To address these various limitations and go well beyond current capabilities, we developed an entirely different manufacturing method for thin-film electrodes enabling reproducible, customizable, and high throughput production of electrodes (1) to be implanted in the operating room using similar brain implant techniques to standard clinical depth electrodes, and (2) to reach deep brain structures and achieve high spatial resolution and channel count with a much thinner electrode body. This advanced manufacturing process exploits (1) titanium (Ti) sacrificial layers employed in the microfabrication of free-standing microelectromechanical system (MEMS) devices. A stylet inserted where the Ti sacrificial layer is removed assists in hardening and implanting the depth electrode—similar to the standard clinical SEEG electrode implantation procedures—and is subsequently removed. (2) This MEMS process is implemented on relatively large ($18 \times 18\ cm^2$) glass substrates (Fig. 1a) allowing us to produce multiple copies of the SEEG devices using materials that are typical for the manufacturing of display screens. Therefore, this unique manufacturing method of thin-film based and clinical-grade depth microelectrode array, termed a micro-stereo-electro-encephalography (μSEEG) electrode, enables flexibility in design, scalability afforded by the display screen manufacturing, which is cost-effective, and does not involve manual assembly typical for standard SEEG electrodes. The μSEEG dimensions can be made custom for application-based contact spacing and channel count. Here, we illustrate the flexibility of our design by manufacturing and testing μSEEG electrodes ranging from a few millimeters to tens of centimeters long, 1.2 mm wide, and 15 μm thick. The manufacturing is compatible with electrode materials that can be used to produce microscale electrode contacts with low electrochemical impedance. We demonstrate the μSEEGs with two low-impedance contact materials: (1) the platinum nanorod (PtNR) contact technology (Fig. 1b) we developed[29,30] and (2) the poly(3,4-ethylenedioxythiophene) polystyrene sulfonate (PEDOT:PSS) electrode technology[31–34] to record broadband neuronal activity including single units (action potentials) and LFPs in rats, pigs, non-human primates (NHPs), and humans. We also test and demonstrate the flexibility of the manufacturing process, which can involve either polyimide or parylene C as the device substrate, both of which are biocompatible. This newly integrated μSEEG electrode induced less tissue damage than cylindrical clinical electrodes in a 2-week rat implant ($n = 1$). Such a flexible, high channel count system paves the way for expanded and more efficacious neuronal recordings and neuromodulation across the spectrum of neuropsychiatric diseases.

Results

Manufacturing μSEEG electrodes

To fabricate μSEEG electrodes, we first coated the glass substrate with a sacrificial polyimide layer and followed by the deposition of titanium etch-mask layer that was patterned with circular openings (Supplementary Fig. 1). The circular openings were used to etch the 1st PI layer that were deposited on top of this layer. At the end of the fabrication process, the entire device layer was flipped, and O_2 plasma was used to create an array of holes in the 1st PI layer. During this process, the titanium etch-mask layer protected the first polyimide layer, except for the circular openings. We then coated the glass substrate with two polyimide layers (1st and 2nd PI layer) and an interleaved Ti sacrificial layer (Fig. 1c). When the sacrificial titanium layer is dissolved in a later stage in the process, the two polyimide layers form the structural enclosure (sheath) for the insertion of the stainless-steel stylet. Above the second polyimide layer, we deposited and patterned the metal trace layer with 10 nm/250 nm chromium/gold stack (deposited and patterned twice for a total trace thickness of 520 nm). Both the width and spacing of the metal traces are 3 μm. As it approaches the connectorization where the PCB is attached, the width of the metal traces expands to 20 μm and its spacing becomes 5 μm. After metallization, a film of platinum–silver alloy was deposited to form the PtNR contacts. The μSEEG electrode has advantages in its form factors including channel count, contact size, and impedance over the previously reported electrodes due to the advanced MEMS technique employed in the fabrication process (Supplementary Table 1)[25–28]. This was followed by a top-most polyimide layer (3rd PI layer, Fig. 1c) coating. The next step involved exposing the microcontacts and defining the electrodes. To achieve this, we induced holes in the 3rd PI layer to expose the platinum–silver alloy films. Simultaneously, we etched the shape of the electrode and additional larger holes (Fig. 1d) into the polyimide layer for mechanical stabilization of the stylet. A nitric acid (HNO_3) etch at 60 °C dissolved the silver from the platinum–silver alloy and exposed the PtNR contacts (Supplementary Fig. 1). The resulting structure is then peeled off from the substrate, flipped, and temporarily adhered to another host glass substrate. At this point, the very first sacrificial polyimide layer was etched by O_2 plasma exposing the titanium etch-mask layer that was pre-patterned with circular openings. Continuation of the O_2 plasma etching through the circular openings drilled through the 1st PI layer, which exposed the titanium sacrificial layer underneath. A final buffered oxide etching dissolved the titanium layers (both sacrificial and etch-mask layer) after which the device is rinsed with flowing deionized water.

The stylet is inserted through the mechanical stabilization holes (Fig. 1d) and the sheath formed by the two polyimide layers (Fig. 1e) to the tip of the electrode (Fig. 1f, g; stylet insertion process illustrated in Supplementary Fig. 2). At the very tip of the electrode, an array of holes was etched in the 1st PI layer around the sacrificial layer (marked with a red arrow in Fig. 1h). As the 2nd PI layer is coated to fill these holes, the

interface between the 1st and 2nd PI layers has effectively a larger surface area than a planar one and as a result, better adhesion between the 1st PI layer and the 2nd PI layer is established. The greater mechanical stability afforded by the array of holes prevents the stylet from piercing through the tip when the stylet reaches this interface (Supplementary Fig. 3). The tip of the stylet is mechanically polished to a rounded shape to minimize damage during insertion (Supplementary Fig. 4).

The μSEEG electrode was manufactured with a U-shaped neck between the electrode array proper and a continuation of the thin film, providing additional length for the metal traces. Once the straight edges of the U-shaped electrode are flipped, the total length of the μSEEG electrode becomes 28 cm, on par with the length of a standard clinical sEEG electrode (Fig. 1j) but with a total thickness of approximately 15 μm. Overall, the μSEEG electrode after the stylet insertion had ~1/10 the cross-sectional area of a typical clinical depth electrode while matching its length and its ability to reach to deep brain structures (Fig. 1j).

μSEEG electrodes are robust to tearing and can be implanted and extracted without deformation, producing less damage than clinical electrodes

As these devices must be robust for longer-term implant periods, mechanical strength and resilience against tear were assessed using pull measurements with both the μSEEG electrode and, to compare with a clinical lead, on a 1.2-mm diameter PMT depth electrode anchored on two polyurethane tube regions around a Pt contact. The tensile strengths (critical forces) were 1 MPa (16 mN) for the μSEEG electrode and 14 kPa (48 mN) for the PMT electrode (Supplementary Fig. 5). To evaluate the reliability of the μSEEG electrodes for longer-term implant periods, we performed an accelerated aging test and a bending test showing negligible degradation over 150 days with 84,000 cycles of lead bending (Supplementary Fig. 6).

Since electrode and contact integrity should also be maintained during implantation of the μSEEG with the stylet without any deformation or loss of function, an acute implantation was first assessed on a phantom brain model. The displacement of a μSEEG and the surrounding phantom brain medium before and after stylet extraction was less than 10 μm (Supplementary Fig. 7, $N = 6$). Electrochemical impedance spectroscopy before and after stylet insertion showed relatively stable 1-kHz impedances, changing from 33.0 ± 2.5 kΩ to 35.0 ± 3.7 kΩ (Supplementary Fig. 8), indicating that there was no substantial damage to the device during stylet insertion. The electrodes were extracted in these phantom experiments and all animal and human experiments without any mechanical deformations or tears.

Finally, to test the amount of tissue damage caused by these devices, we implanted rats with one chronic μSEEG electrode with 1.89 mm recording length on one hemisphere and a clinical electrode on the other hemisphere for 14 days ($N = 4$ electrodes). Insertion of the μSEEG electrode resulted in decreased astrocyte scarring, as measured by significantly lower GFAP positive area as compared to the clinical electrode as shown in Supplementary Fig. 10. We observed no significant difference in the number of Neun-positive cells surrounding the lesion between the μSEEG and the clinical grid, but there was a small non-significant improvement with the μSEEG electrode (2-way ANOVA, $F(1, 72) = 3.290$, $p = 0.0739$). We also imaged the PtNR μSEEG electrodes upon extraction from the NHP brain and observed minimal changes compared to non-implanted ones, demonstrating the stability of the μSEEG electrode in tissue (Supplementary Fig. 11, $N = 3$).

μSEEG flexible design is scalable for multiple acute and chronic applications

To demonstrate the flexibility in the manufacture, design, and use of μSEEG to record neurophysiologically relevant neural activity in multiple settings and species, we tested devices with working neural recording lengths ranging from 1.89 to 7.65 mm, made from either parylene C or polyimide, with microelectrode contacts composed of either PEDOT:PSS or PtNRs (Fig. 1k, Supplementary Fig. 12, and Supplementary Table 3). We transitioned to all polyimide μSEEG electrodes after we observed that parylene C μSEEG develop cracks in the parylene C layers and in the PEDOT:PSS layers after stylet insertion, whereas polyimide μSEEG did not suffer from any cracks. The crack was caused by mechanical damage to the parylene C layers applied by the stylet during insertion, which then propagated to the PEDOT:PSS layer (Supplementary Fig. 9). In addition, PtNRs contacts did not suffer any delamination from the μSEEG whereas PEDOT:PSS suffered from delamination after stylet insertion in a substantial subset of electrodes, therefore reducing product yield.

All designs used have microelectrode contacts (also called channels, each 30 μm contact diameter for PtNRs and 20 μm contact diameter for PEDOT:PSS) with a center-to-center spacing of 60 μm (Fig. 1k, Supplementary Fig. 12, and Supplementary Table 3). While the diameter of the microcontacts can be adjusted, we have found that a contact diameter of 30 μm provides the most reproducible and optimal results for PtNRs based on our most recent optimization efforts. Therefore, we decided to use 30 μm as a diameter for the PtNR electrodes. We created two short versions: (1) a short 64-channel μSEEG; (2) a short 32-channel μSEEG. The short 64-channel μSEEG includes 64 microelectrode contacts along a recording length of 3.80 mm. Side flaps are incorporated to help with the stabilization of the array upon insertion. This design is intended for use in the intraoperative setting and resembles other microelectrode arrays (often called laminar arrays), which were designed to capture activity across the cortical layers[35]. (Fig. 1k–n, Supplementary Figs. 7 and 8, and Supplementary Table 3). The architecture of this system is formatted for use in smaller animals or in recording from the neocortex of humans or larger animal species—such as for use in a brain computer interface. The short 32-channel μSEEG (Fig. 1k, l, right; Supplementary Fig. 12 and Supplementary Table 3) includes 32 microelectrode contacts along a recording length of 1.92 mm intended for use in chronic recordings in smaller animals.

We also made a longer version designed for accessing deeper structures (simultaneously with lateral cortex) in larger animals. This long μSEEG includes 128 microelectrode contacts at a 60 μm center-to-center spacing along a recording length of 7.65 mm at the tip of the entire array. This configuration most closely resembles clinical depth electrodes (Fig. 1j, o and Supplementary Fig. 12), although the spacing of the contacts or the incorporation of contacts with diameters larger than 100 μm in a future μSEEG design can be varied for specific end use. Our custom acquisition board connects to a 1024-channel electrophysiology control system, provided by Intan Technologies LLC[29]. Depending on the channel counts of the electrode, we utilized 1–8 RHD2164 chips for impedance measurement and for recordings.

μSEEG electrodes record local field potential events both acutely and chronically

To test the capabilities of the μSEEG electrode in capturing relevant neural activity[36] we recorded from the rat barrel cortex in both the acute and chronic settings. Acute recordings from rat S1 cortex under anesthesia were performed with both a surface μECoG array[30] and the 64-channel μSEEG (Fig. 2a–c and Supplementary Figs. 12–15). When contralateral whiskers were selectively deflected by a directed air puff stream, we found LFP voltage responses (z-scored relative to 0.5 s before stimulus delivery) and increases in high gamma power (HGP; power between 65 and 200 Hz) on both the μECoG and μSEEG (Fig. 2d and Supplementary Figs. 14 and 15). At different depths along the μSEEG electrode and at different channels in the μECoG grid, whisker deflection induced significantly greater LFP and HGP responses than baseline (0.5 s before stimulation; Wilcoxon rank-sum test; $p < 0.001$;

https://doi.org/10.1038/s41467-023-43727-9

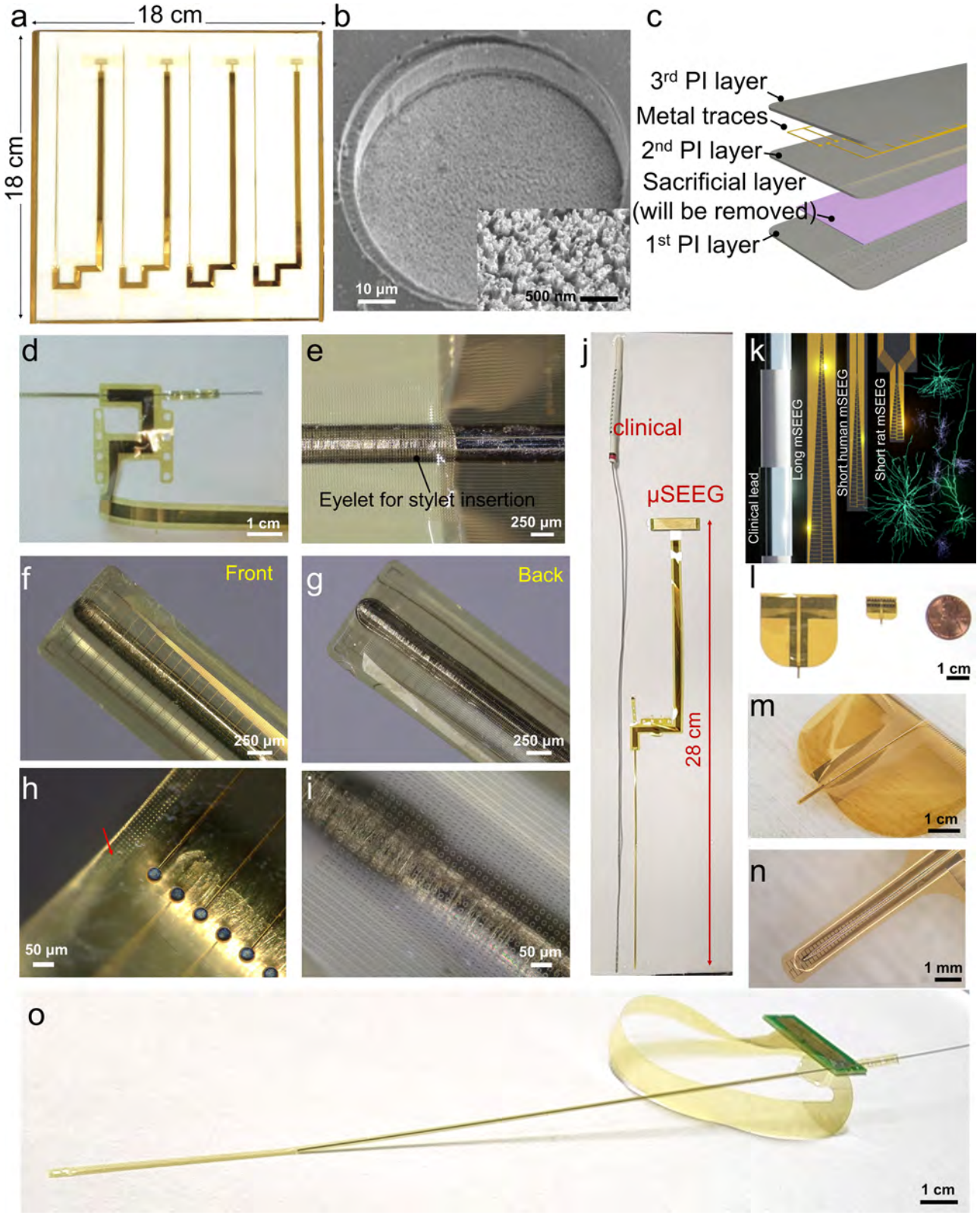

Fig. 1 | μSEEG electrode arrays. a Photograph of a single glass substrate plate with four μSEEG electrodes. **b** Scanning electron microscope (SEM) image of a single PtNR contact; Inset is a magnified image showing the PtNRs. **c** Structural composition of the μSEEG array. **d** Photograph showing the 'neck' of the array where the U-shape pattern is flipped to provide metal trace extension and circular holes are present to stabilize the inserted stainless-steel stylet. **e** Optical microscope (OM) image of the region of insertion of the stylet in the inflatable "sheath" of the μSEEG electrode. OM images of **f** front, **g** back side of the μSEEG electrode. **h**, **i** Magnified OM images at the tip **f** front and **g** back layers. The red arrow indicates the micro-hole arrays that interlock the 1st and 2nd PI layers. **j** Long 128-channel μSEEG electrode and comparison with a clinical electrode. **k** Diagram of the relative scale of human cortical neurons relative to a clinical SEEG lead and μSEEG electrodes[45–47]. **l** Flexibility in manufacturing procedure to produce short 64-channel μSEEG electrodes (left) or short 32-channel μSEEG electrodes (right) and photographs showing **m** overall and **n** tip of the 64-channel μSEEG electrodes. **o** A perspective view of the long μSEEG electrode with partially inserted stylet illustrating the flexibility and slenderness of the electrode body.

https://doi.org/10.1038/s41467-023-43727-9

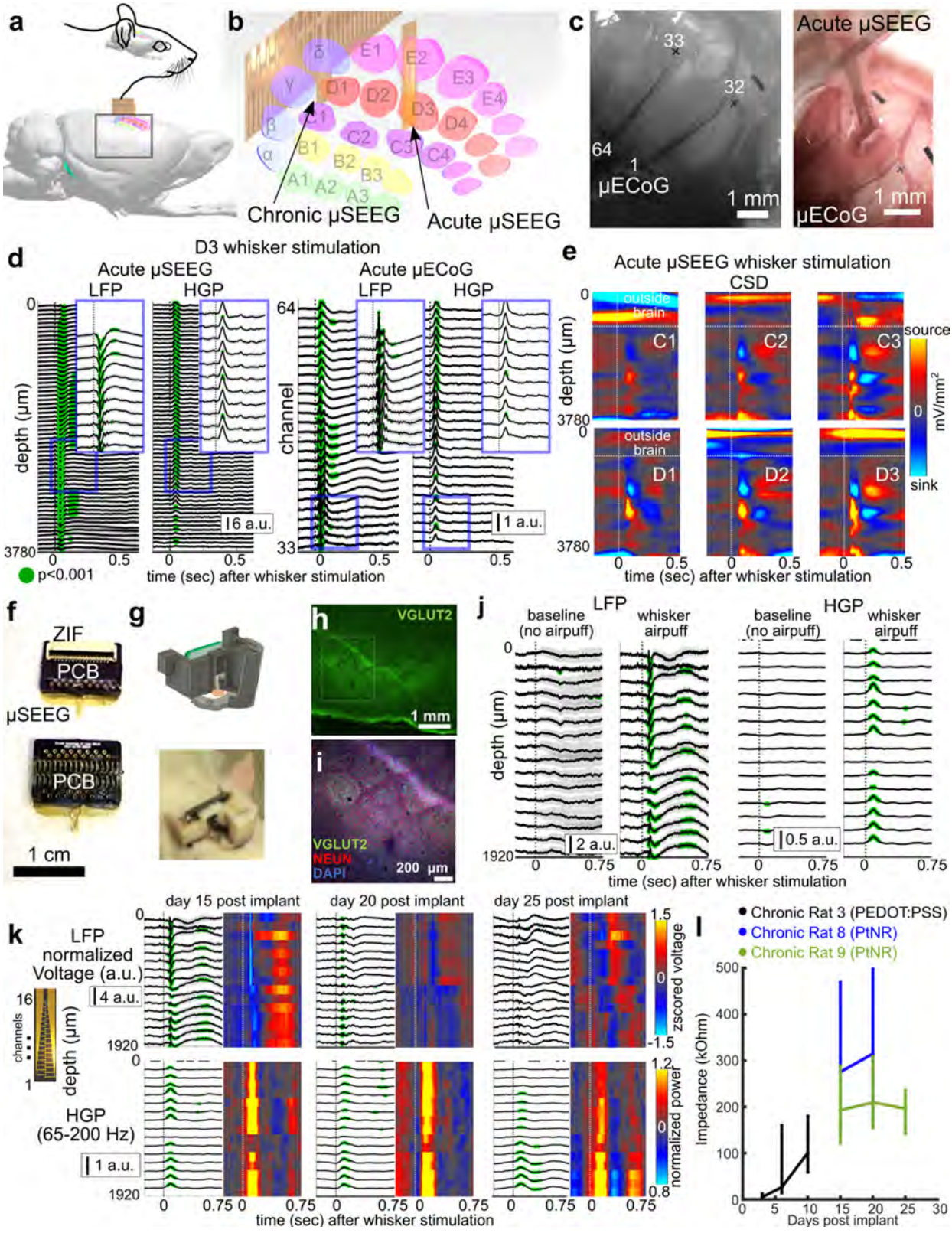

$n = 39$ trials), with some deflections showing reversals in voltages along the depth electrode, also reflected in the current source density (CSD) analysis (Fig. 2e and Supplementary Figs. 16 and 17). Furthermore, we found sensory specificity in the responses, with stronger neural responses (in the LFP, HGP and CSD) with stimulation closer to D3, C3, and even E3 (Fig. 2e and Supplementary Figs. 14–18), allowing us to estimate the location of the electrodes relative to columns of the barrel cortex. The concurrently implanted μECoG surface microelectrode, used to confirm we were recording from the barrel cortex, reflected similar D3, C3, and even E3 whisker-selective voltage and HGP dynamics in response to sensory stimulation (Supplementary Figs. 19–21).

After confirming that μSEEG electrodes could detect sensory stimulation-induced neural activity acutely, we developed a 3D-printed

Fig. 2 | μSEEG electrodes can be used for acute and chronic implantations and recordings. a, **b** Location and 3D reconstruction of possible locations of the acute and chronic implantation of μSEEG electrode devices for recording from the rat barrel cortex[48]. **c** Images of the implanted μECoG electrode (left) and the μSEEG electrode (right). Note some contacts are outside brain tissue on the μSEEG electrode. **d** Example voltage responses across the μSEEG electrode (left) and the μECoG electrode (right) to whisker stimulation at different whisker locations, with the insets zoomed-in views of the voltages and high gamma power (HGP, 65–200 Hz). Green dots indicate a significantly different from 0.5 s before (which is baseline) air puff stimulation to the whisker (Wilcoxon rank-sum test) per channel and across trials. Number of trials >10. **e** Increasing responses as air puff stimulation is closer to the C3 and D3 whiskers as indicated by the current source density (CSD). **f** 32-channel μSEEG electrode for chronic rat recordings and a custom printed circuit board (PCB) with zero-insertion-force (ZIF) connector which electrically connects the device to the recording system via flexible flat cable (FFC). **g** 3D-printed headstage for the 32-channel μSEEG electrode. **h**–**i** Electrode location localization as visualized using histology. **j** Example voltage and high gamma power (65–200 Hz) responses without stimuli (baseline) versus with stimuli (whisker air puff). **k** Responses to air puffs at three different time points post implant in one rat. **l** Impedance measures at 1 kHz across multiple days and multiple rats; vertical bars are standard deviation from average values. For (**d**), (**j**), and (**k**), a.u. arbitrary units in *z*-scored voltage for the LFP and normalized High Gamma Power (HGP).

headstage for a chronic implantable version of the short 32-channel μSEEG electrode (Fig. 2f, g and Supplementary Fig. 22). We implanted the device successfully in nine rats (Supplementary Table 2) with rat barrel cortical responses in three of the nine rats with histological confirmation of the electrode location (Fig. 2g–k). We implanted the devices for 25 days and recorded at three or more time points following implantation to test recording quality and impedance changes over time (Fig. 2f–l). Impedance fluctuated across days per rat but was still low enough to record voltage responses (63.5 ± 49.1 kΩ, 268.0 ± 115.2 kΩ, and 198.0 ± 48.7 kΩ for rat 3, 8, and 9, respectively) across rats and across days post implant (Fig. 2l). We recorded voltage responses and changes in high gamma power with whisker stimulation, which was not evident when performing sham controls (trials with no air puffs; Fig. 2j). Furthermore, we observed similar voltage responses and HGP recorded by functional microcontacts across the days in individual rats (Fig. 2k). This result was confirmed by calculating the correlation between averaged responses across days per channel. In particular, we found that activity during whisker stimulation was more correlated per channel across days (Pearson's linear correlation average rho across channels: 0.2 ± 0.06 (std), maximum average: 0.73 ± 0.10 (std)) compared to sham controls (Pearson's linear correlation average rho across days per channel: 0.17 ± 0.03 (std), maximum average: 0.56 ± 0.13 (std)). These differences were also reflected in the high gamma power measures (Pearson's linear correlation average rho across days per channel: whisker stimulation: 0.33 ± 0.28 (std), maximum average: 0.70 ± 0.15 (std); sham controls: 0.21 ± 0.07 (std), maximum average: 0.54 ± 0.04 (std)).

μSEEG electrodes acutely record stimulus and anesthesia-induced dynamics across species

Demonstrating that μSEEG electrodes can be used to record clinically relevant dynamics in the human brain requires both scaling up the devices for use in recording from larger brains as well as demonstrating that μSEEG electrodes record clinically and neurologically relevant neural dynamics[37,38]. A major goal was to test the μSEEG while modeling settings and paradigms that could be used in acute or chronic clinical mapping of activity[6,39]. Therefore, we recorded neural activity using the short 64-channel μSEEG in three different settings: (1) from the somatosensory cortex in an anesthetized pig, (2) in an anesthetized NHP in the operating room, and (3) in the operating room from human cortex preceding tumor resection (Fig. 3, Supplementary Fig. 12, and Supplementary Table 2).

Intraoperative clinical mapping often involves the use of stimulation to delineate functional (eloquent) tissue and connectivity. To model this paradigm, we stimulated the pig spinal cord with a bipolar stimulator and recorded with the μSEEG in the pig cortex to map responsiveness and connectivity. We recorded changes in neural activity across cortical layers in the somatosensory cortex induced by direct electrical stimulation in the spine using the short 64-channel μSEEG electrode, stimulating with currents ranging from 200 to 6000 μA (Fig. 3a–c). We found significantly increasing voltage responses with increasing injected current per channel ($p < 0.001$; Kruskal–Wallis test; Fig. 3a and Supplementary Fig. 23). The response waveforms varied between the different contacts, including a field reversal approximately in the middle of the implanted electrode. This field reversal was most obvious at stimulation currents >800 μA (green dots, Fig. 3b, significantly above a baseline taken 0.5 s before stimulation, Wilcoxon rank-sum test). When we plotted the largest absolute voltage deflections from baseline, we found a clear division in the voltage between the deeper contacts and the superficial contacts. This high-resolution laminar distribution of the responses was also reflected in differences in oscillatory power across the cortical layers. We found gamma (30–55 Hz; $p = 0.0056$ for 6000 μA) power in the more superficial contacts (Kruskal–Wallis multiple comparisons test; Fig. 3c and Supplementary Fig. 23). We also found response timing differences, with the time to voltage peak and HGP peak shorter in middle and superficial contacts (resulting in a Pearson's linear correlation between peak timing and channel number: voltage- rho = −0.11; $p < 0.0001$; HGP- rho = −0.04; $p = 0.03$) with the trend reversed with the peak beta power (beta power- rho = 0.04; $p = 0.03$; Fig. 3c and Supplementary Fig. 23). In other words, the μSEEG electrode recorded stimulation-induced activity with cortical layer-specificity at a spatial resolution (60 μm contact to contact pitch) not possible with current clinical leads (resolution on the scale of millimeters; Supplementary Fig. 12).

In a second intraoperative paradigm, we recorded neural activity across cortical layers in the visual cortex of an anesthetized NHP using the short 64-channel μSEEG electrode. We found ongoing anesthesia-related burst suppression, which could be detected using automatic approaches along the depth electrode[40] (Fig. 3d and Supplementary Fig. 24). As shown in previous preparations and other species, we found a gradient of activity across the array, with more detected bursts early in the recording and even relative to suppression epochs (as represented by the burst-suppression ratio) in more superficial contacts[40] (Supplementary Fig. 24). This resulted in high negative correlation values between electrode depth into the tissue and detected bursts over 300 s ($r = -0.73$; $p = 0.0021$; Pearson's linear correlation; Supplementary Fig. 24).

Finally, in a true test of the translational feasibility of the μSEEG, we acutely implanted short 64-channel μSEEG electrodes in the left middle temporal gyrus in two separate human patient participants (Figs. 1f and 3e–g and Supplementary Video 1) undergoing temporal lobe resection for clinical reasons. With each participant, we inserted a single 64-channel short μSEEG devices into the tissue, which the clinical team determined would be resected. The recordings were brief (10 min) yet we were able to record ongoing spontaneous activity. In one case, the participant was under general anesthesia and there was clear evidence of anesthesia-induced burst suppression in the recordings (HS1), also detected through an automatic algorithm[40] (Fig. 3e). Like in the NHP, the number of detected bursts was increased in more superficial contacts, resulting in a correlation between depth (into the tissue) and burst detections of $r = -0.5927$ ($p = 0.0023$; Pearson's linear correlation, over 300 s of recording). Notably, we also found the thin film component of the electrode device, once implanted, would move with the brain tissue movement, indicating the device

https://doi.org/10.1038/s41467-023-43727-9

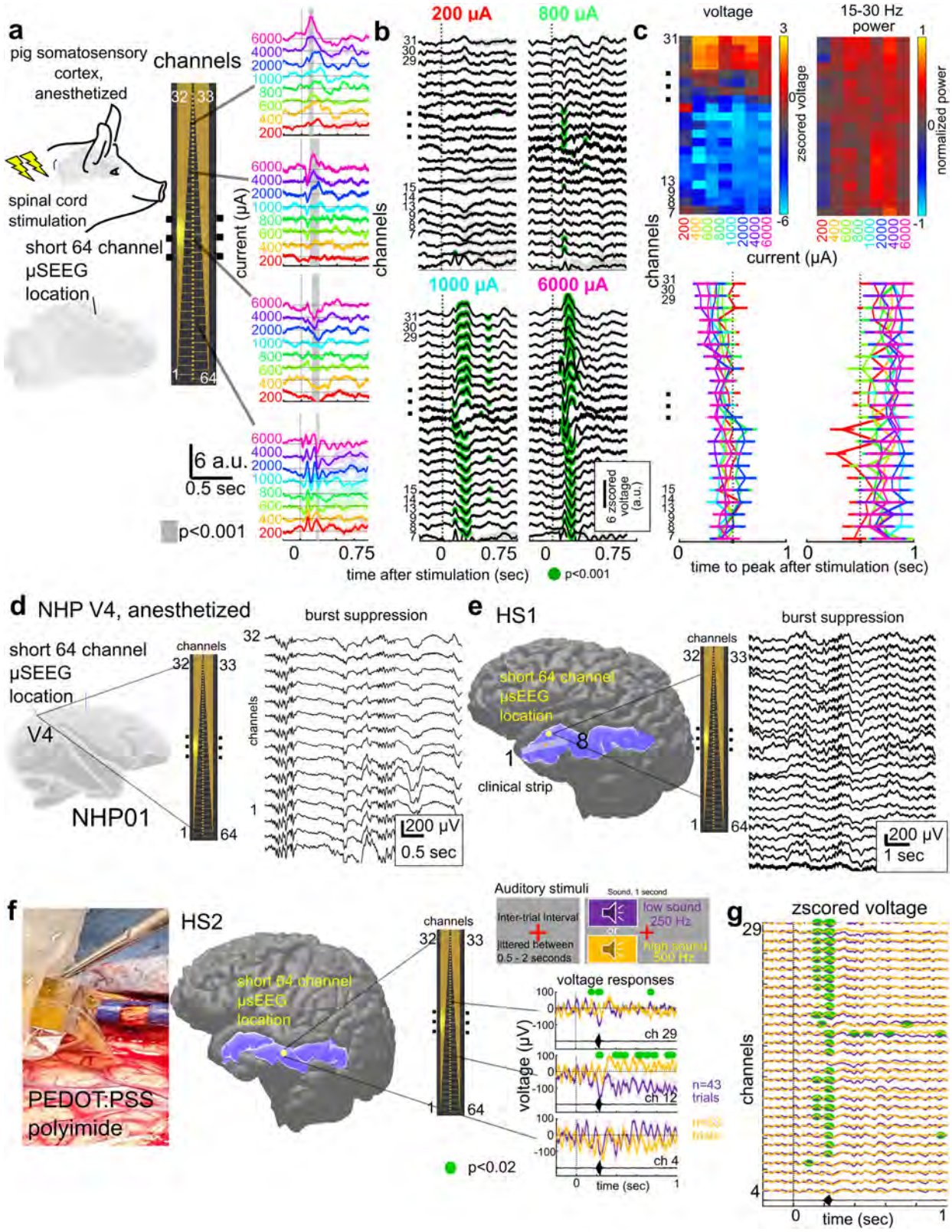

is light enough to move with the recording medium (Supplementary Video 1).

In the second recording, the participant was awake under monitored anesthesia care (MAC) and listened to low and high auditory cues (HS2; see Materials and Methods; Fig. 3f, g). The neural responses were significantly different between low and high tones in the z-scored voltage values and in HGP at the onset of the sound ($p < 0.02$, corrected for multiple comparisons; Wilcoxon rank-sum test). Furthermore, there were more significant differences in the responses between low and high sounds in superficial array contacts (Fig. 3g).

μSEEG electrodes detect single-unit cortical activity

A key purpose of the μSEEG electrode is to offer advantages over current clinical depth electrodes including increased spatial resolution

Fig. 3 | Stimulated neural activity and ongoing clinically relevant neural dynamics can be recorded acutely using the short 64-channel μSEEG electrode. **a** Direct electrical stimulation of the spinal cord during acute short μSEEG recording from the pig cortex. Gray bar indicates significantly different between current steps, Wilcoxon rank-sum test. **b** Voltage responses along the electrode depth with more responses significantly different to baseline (0.5 s before stimulation) occurring more with higher current levels (green dots, Wilcoxon rank-sum test). **c** Top: two-dimensional heat map of the largest voltage deflection from baseline per channel and per current step (left) and the maximum peak in beta (15–30 Hz) power oscillations (right). Bottom: time to peak voltage (left) and peak beta band power (right) after stimulation per channel and current step. Gray dotted line indicating 0.5 s after stimulation. **d** Acute implant of the short μSEEG electrode into V4 in an anesthetized NHP and ongoing evidence of burst suppression. **e**–**g** Acute implantation of short μSEEG electrodes into left anterior temporal lobe middle temporal gyrus (highlighted in blue) to be resected in the course of clinical treatment in two participants, HS1 and HS2 with a photograph of the implant, a three-dimensional reconstruction of each participants' brain and the relative location of the μSEEG electrode (yellow dot) with a zoomed in inset view of the 64 channels as implanted. **e** Spontaneous ongoing activity with burst suppression along the electrode depth. **f** Auditory responses to low and high tones presented at random in sequence with varying jitter times while recording activity in the lateral temporal lobe. Green dots indicating $p < 0.02$ significant difference between low and high tones, Wilcoxon rank-sum test. **g** Differences in the responses varied across the depth of the electrode. *Z*-scored voltage responses at multiple channels at different depths averaged across trials. Green dots indicating $p < 0.02$ significant difference between low and high tones, Wilcoxon rank-sum test. For (**a**) and (**b**), a.u. arbitrary units in *z*-scored voltage for the LFP and normalized High Gamma Power (HGP).

as well as increased neural resolution. To test whether the μSEEG device can record neural activity at multiple depths in the brain closer to the scale of the human brain, we designed and built the long μSEEG electrode (Figs. 1 and 4 and Supplementary Fig. 12). The 128-channel long μSEEG electrode was built to most resemble clinical depth electrodes with a working recording length of 7.65 mm at the tip of the electrode that is, overall, 28 cm long, 1.2 mm wide, and 15 μm thick which would allow insertion and recording from deeper brain structures. The electrode contacts in this design are concentrated at the tip of the device with inter-contact distances of 60 μm. To test if we could record single neuron activity at depth, we recorded neural dynamics in an NHP that was awake but resting and viewing flickering light-emitting diodes (LEDs)[29] to test for visual responses. The long μSEEG electrode was held by a microelectrode microdrive (see Materials and Methods; Supplementary Fig. 25) to drive the microelectrode to multiple depths from the surface of the cortex within an implanted chamber (Fig. 4a). Along the trajectory moving toward the thalamus, we stopped and recorded at three different depths to examine spiking activity in the cortex as well as in white matter (Fig. 4b). At depths 1 and 2, we found we could record spikes which clustered into single-unit and multi-unit activity (MUA) (depth 1: 1 MUA cluster, 4 single-unit clusters; depth 2: 5 MUA clusters, 31 single-unit clusters; Fig. 4c–e), which we determined by examining the autocorrelation of the spike times and the waveform consistently through time using Kilosort[41]. We did not find any identifiable single-unit activity at depth 3, we were likely mostly in white matter at that depth (depth 3: 13 MUA clusters; Fig. 4f, g). The units and MUA clusters were distributed at different distances and locations along the 128 contacts of the long μSEEG with a range of spike rates, most of which were around 2 Hz (Fig. 4h). Finally, we found the waveform measures show that the units sampled at depths 1 and 2 were clustered in amplitude, the peak-trough ratio, and spike duration measures compared to the MUA clusters found at depth 3 (Fig. 4i). In other words, these clusters are more likely single-unit activity or putative neurons since they were detected while the recording contacts were in cortex but not while in white matter.

Discussion

We developed a μSEEG electrode that is implanted with a stylet inserter similar to clinical SEEG electrodes, but can be tailored in its range of depth to sample cortical and or deep structures in the brain (or both). This advanced μSEEG electrode can record broadband spontaneous and evoked neurophysiological activity including LFP, CSD and single/multi-unit activity across a variety of species including humans and across entire depths of the brain. While the μSEEG construction is robust, it induced less apparent tissue damage than clinical SEEG electrodes. The layout, shape, and size of the μSEEG electrode could be generated with customizable designs (Fig. 1k–n) by leveraging established display screen fabrication techniques on large glass wafers. Fabrication on glass wafers also promises excellent scalability. Glass panels used in the manufacture of displays use plates a few square meters in area indicating that large number of arrays can be manufactured even if the arrays are long. Furthermore, the high resolution of lithographic capability can achieve 1.2 μm for both metal line and space (L/S) of flat panel displays[42]. Therefore, the number of contacts can be increased well beyond 128 channels presented here importantly afforded at a much lower manufacturing cost than clinical and other research depth electrodes. A 240 sq. in. monitor has a retail price of nearly $100 with active transistors and light-emitting diodes. The same area can be used to manufacture at least 20 μSEEG electrodes, pointing to significantly lower costs than current clinical SEEG electrodes (>$1000 per electrode) when manufactured at scale. This cheaper advanced manufacturing approach and the added spatial resolution and sensitivity to cellular activity in a smaller form factor can advance our ability to study and treat the human brain and will help broaden the access of the technology to underserved communities and other brain diseases.

One potential limitation of these designs is cross-talk among the channels. While we have not definitively quantified cross-talk in the recordings, we observed a strong common-mode signal on all contacts that we subtracted in order to delineate CSD dynamics. One of the possible reasons for the common-mode signal would be recording the same neural activities, given the narrow spacing of the electrodes (60 μm). In addition, we observed that the location of the reference contact also affects the amount of common signal captured. If inter-channel cross-talk is a substantial issue, future designs could involve distributing the metal traces in separate polymer layers. Another limitation concerns connectorization. Current connectors do not match typical clinical standards. Improving the back-end of the devices is an area of active development. Furthermore, the current design includes contacts facing only one direction along the electrode length. Future designs can involve developing multiple directional contact sampling. Finally, additional optimizations regarding the stylet diameter and the placement of the microcontacts could enhance the capabilities of single-unit recording even after the stylet is retracted. This would prevent the electrode from deflating, ensuring that the microcontacts remain in close proximity to the neural tissues. This can be achieved either by reducing the diameter of the stylet or by positioning the microcontacts along the edge of the electrode.

Nevertheless, advantages include the size and shape of the electrodes as well as the capabilities of the devices. For instance, the width of the μSEEG was still destructive to brain tissue, unlike ultraflexible nanoelectronic probes[43]. However, a human-grade electrode that can reach 10 cm deep into the brain with 128 contacts necessitated the stylet-guided μSEEG design, especially with stimulation considerations where the metal traces need to be sufficiently wide to reduce serial resistances and associated potential drops that compromise the long-term electrode stability. Lastly, the μSEEG can also offer stimulation with favorable stimulation characteristics with PtNRs compared to clinical SEEG electrodes. We prepared PtNR electrode contacts with 1 mm diameter to test how PtNR compares with clinical electrodes in

https://doi.org/10.1038/s41467-023-43727-9

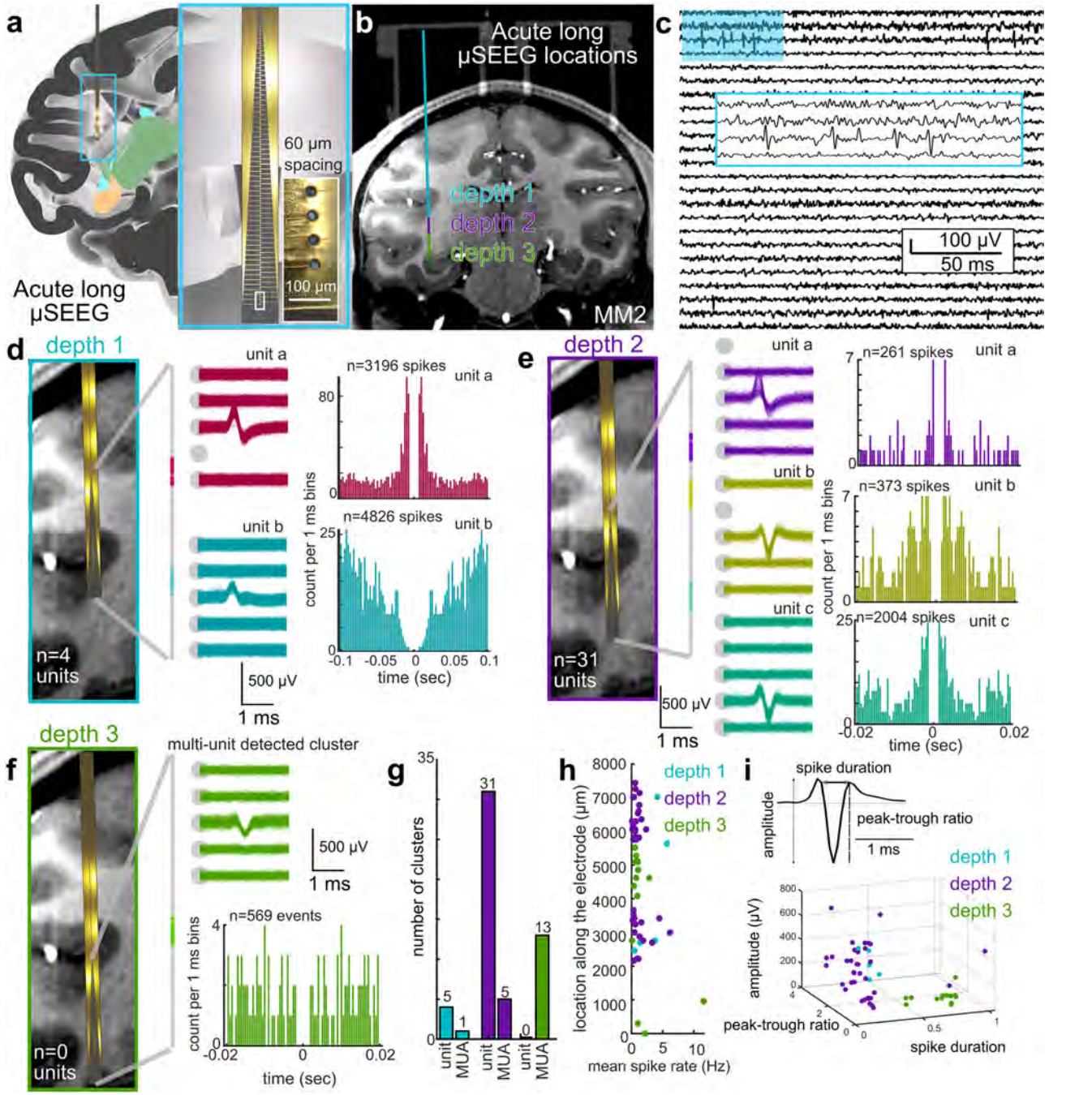

Fig. 4 | Single-unit activity could be recorded using long μSEEG electrodes. **a** Three-dimensional reconstruction of the locations of the long μSEEG inserted at multiple depths into the parietal lobe, temporal lobe, and deeper into the tissue, with a zoomed-in view of the microelectrodes in the long μSEEG[49,50]. **b** MRI with the overlaid CT (chambers above) and the three putative long μSEEG depths in the brain. **c** Example recording from the second depth to show single-unit spiking activity (filtered to between 300 and 6000 Hz). **d**, **e** Example single units recorded at electrode depth 1 (**d**) and depth 2 (**e**) showing overlaid waveforms and the autocorrelation of the spike times. **f** Single-unit activity was not observed at depth 3 which seemed to be in white matter, but possible MUA was recorded at depth 3. **g** Numbers of detected single units and MUA clusters. **h** Location-detected clusters relative to the mean spike rates for the different depths. Each dot is a cluster (which can represent single units or MUA). **i** Spike waveform measures of single units and MUA waveforms showing separation of events detected at depths 1 and 2 versus 3.

delivering stimulation in saline (Supplementary Fig. 26). In addition to manufacturing variable contact sizes with this approach, the PtNR contacts at a 1 mm diameter offer smaller voltage transients and higher electrochemical safety limits when delivering direct electrical stimulation than clinical electrodes of similar surface areas (Supplementary Fig. 26). Stimulation and recording contacts can be distributed uniformly or in clusters across the length of the μSEEG. Thus, the μSEEG can offer micro- and macro-stimulation capability for use in future deep brain stimulation (DBS) or direct electrical stimulation application.

In conclusion, these μSEEG electrodes provide an innovative approach enabling recording across the entire depth of the human brain with greater resolution than ever achieved before. The smaller volume of the μSEEG electrode and its compatibility with procedures used in clinical practice paves the way to increasing our understanding of brain diseases and offering unique and clinical interventions.

Methods

μSEEG fabrication

Polished and cleaned soda lime glass plates were used as substrates. A release layer of Micro-90 diluted with deionized water was spin-coated onto the glass. A sacrificial 5-μm-thick polyimide layer (PI-2611, HD MicroSystems) was then deposited. This layer would later separate the device layers from the glass plate. A Ti hard mask was formed for net layer formation, followed by standard lithography, descum, metal deposition, and lift-off processes. The Ti hard mask contained via patterns for hole arrays and a rectangular shape for a sheath. Next, another polyimide layer was applied, serving as the sacrificial bottom layer with holes. A Ti sacrificial layer was deposited to act as an etch-stop layer. Adhesion between the layers was increased by patterning hole arrays. The 1st PI layer was then selectively etched, and the photoresist layer was removed. Afterward, the glass substrate underwent baking, and a 2nd PI layer was applied. Metal traces were formed on the 2nd PI layer, composed of Cr/Au (10/250 nm). This process was repeated to create double-layered metal leads. A PtAg alloy was selectively formed on the micro-contact recording sites. A Ti capping layer was added to prevent oxidation. A 3rd polyimide layer was applied, followed by a Ti hard mask. Etching processes exposed the Ti layer deposited during Ti hard mask for net layer formation on the sacrificial PI layer. Another photolithography and etching process was applied to open via holes for recording sites and contact pads. The exposed PI layers were etched, and a Ti passivation layer and parylene C were deposited to protect PI layers against dealloying. The Ti passivation layer and parylene C layers were then patterned and etched selectively on the recording site regions to expose the PtAg alloys. Dealloying of PtAg alloys was performed. Then, the parylene C and Ti passivation layers were removed. The electrodes were delaminated from the glass substrate. The delaminated electrode was transferred onto another carrier glass wafer. Hole arrays were formed on the 1st PI layer by etching through the sacrificial PI layer and the Ti hard mask for net layer formation. The Ti hard mask for net layer formation and Ti sacrificial layers were dissolved in BOE, and the electrode was rinsed with DI water.

Rat experiments

The rat experiments were conducted with approval from the University of California San Diego Institutional Animal Care and Use Committee (protocol # S19030). All rats (Sprague-Dawley) were all male, and 3 months old. Acute in vivo electrophysiological recordings were performed on the rat primary somatosensory "barrel" cortex (S1) with the μECoG electrode and the μSEEG electrode. The rat was anesthetized and craniotomy was performed under isofluorane anesthesia. The body temperature of the rat was maintained at 37 °C with a heating pad. Craniotomy and dura removal were performed over the right barrel and surrounding cortical region. Following electrode placement, the rat was transitioned to ketamine/xylazine anesthesia for recording. Tactile stimulation was performed by delivering air puffs to the whisker pad. Air puffs were pressure-injected through a glass micropipette using a PV830 pneumatic picopump (World Precision Instruments, Inc.) with 1 s pulses ($n > 10$ trials per location). The contralateral (left) whiskers with respect to the recording sites were deflected by air puff (±2 mm). First, the whole contralateral whiskers (multi-whisker) were stimulated. Then single whiskers (C1-3, D1-3, E1-4) were stimulated by placing the pipette as close as possible to each whisker to avoid deflection of the neighboring whiskers. Recording data were collected for 60 s for each whisker.

Pig experiments

The pig experiments were conducted with approval from the University of California San Diego Institutional Animal Care and Use Committee. The pigs (Yucatan) were all female, and 7-month-old. The pigs were induced with isoflurane and intubated. After anesthesia, the pig was positioned in a stereotaxic frame in a prone position. Vital signs were closely monitored, including heart rate, blood pressure, $EtCO_2$, respiratory rate, and blood oxygenation. The surgical site on the cranium was focused on the motor cortex of the frontal lobe and the somatosensory cortex of the parietal lobe. A skin incision (2–4 inches long) was made, followed by a unilateral craniotomy using a high-speed surgical drill. The removed bone created a window of approximately 25 mm × 15 mm. The underlying dura was cut and moved towards the sagittal sinus. The cortex was hydrated with a normal saline solution. A sterile multielectrode implant was then placed on the surface of the exposed cortex. After placement, the electrode ribbon (less than 1 cm in width) was connected to an Intan recording controller. For spinal exposure, a midline incision and laminectomy were performed to sufficiently expose the target thoracolumbar enlargement of the spinal cord. Following laminectomy, a longitudinal incision was made in the dura, allowing for the exposure of the spinal cord. Spinal cord stimulation was carried out using a handheld Ojemann stimulator with two ball tips (Radionics Inc., Burlington, MA) spaced 0.5 cm apart. Isoflurane anesthesia was discontinued after completion of surgical procedures and replaced with IV Propofol for the duration of the stimulation testing.

NHP experiments

The experimental procedures on rhesus macaques were conducted in compliance with the Guide to the Care and Use of Laboratory Animals. Measures were taken to minimize discomfort, and the Institutional Animal Care and Use Committee at Massachusetts General Hospital oversaw and approved all procedures. The study involved testing μSEEG electrodes in two scenarios: (1) recording from a short μSEEG in an anesthetized NHP in the operating room for visual cortical dynamics, and (2) recording from a long μSEEG in an awake NHP with the electrode lowered through an implanted chamber using a standard Microdrive.

In the first setting, recordings were obtained from an adult male rhesus macaque (age 11) under general endotracheal anesthesia with isoflurane. A craniotomy was performed over the visual cortex, and the short μSEEG electrode was carefully implanted. Signals were recorded using a custom Intan Recording System.

For the awake NHP preparation, another adult male rhesus macaque (age 14) was implanted with two recording chambers to access different brain regions. A Microdrive was attached to allow insertion through the dura. Trajectories were determined by mapping Microdrive depths to preoperative magnetic resonance imaging (MRI) and postoperative CT scans. The electrode was lowered to record neural activity at three different depths. No noticeable adverse behavioral effects were observed before or after electrode implantation or removal. Recordings of the long μSEEG utilized a 1024-channel Intan Recording system with a specialized device for recording thin film microelectrodes.

Human tests

The study involved intraoperative recordings on two participants undergoing neurosurgery at Massachusetts General Hospital (MGH). The research had received approval from the Massachusetts General Brigham (formerly Partners) Institutional Review Board. These participants, aged 28 and 46, one female and one male, were already scheduled for a craniotomy for various clinical neurophysiological monitoring purposes, including mapping motor, language, and sensory regions, as well as tissue removal for epilepsy treatment. Both individuals provided voluntary, informed consent, understanding that their clinical care would remain unaffected and they could withdraw from the study at any time without impacting their treatment. These patients were originally scheduled for left anterior temporal lobe surgery for epilepsy or tumor treatment. The option for research recordings was considered only after the decision to proceed with

surgery was confirmed. Neither participant was in a medically unstable condition or in need of urgent surgery. The participants were not monetarily compensated for their involvement. All decisions were made in consultation with the treating neurosurgeon and clinical team. Patients lacking decision-making capacity were not included, as determined by the primary clinical team or physician. The time allocated for research recording for each subject was limited to minimize risk. Participants also consented to the sharing of de-identified neural data.

Reporting summary

Further information on research design is available in the Nature Portfolio Reporting Summary linked to this article.

Data availability

All data obtained in this study are either presented in the paper and the Supplementary Materials or deposited in open database. Animal brain recording data is available on OpenNeuro (https://openneuro.org/ at Accession Number ds004819) and human brain recording data could be accessed at Data Archive BRAIN Initiative (DABI) (https://dabi.loni.usc.edu/ at https://doi.org/10.18120/dn61-9y73) using the iEEG BIDS format[44]. To visualize the locations in 3D in the non-human primate and rodent brains, we used the Scalable Brain Atlas with the Calabrese atlas (https://scalablebrainatlas.incf.org/ ; exported into Blender (https://www.blender.org/). Source Data are provided with this paper.

Code availability

Data were acquired using OpenEphys (http://www.open-ephys.org/) and Intan software (https://intantech.com/RHX_software.html). Most of the data were extracted and processed using MATLAB (Mathworks, Natick, MA). Custom MATLAB code (version R2021a) are available in GitHub (https://github.com/Center-For-Neurotechnology/MicrosEEG_Data_Analysis, Zenodo https://doi.org/10.5281/zenodo.10042080). Spike sorting was performed using kilosort 2.5 (https://github.com/MouseLand/Kilosort) with further determination of single units versus multi-unit activity performed in post-processing using Phy (https://github.com/cortex-lab/phy) and then manually curated using in-house MATLAB code to visually inspect the template as well as the waveforms assigned to each cluster. We detected bursts and calculated the burst suppression ratio (BSR) using an automated method (https://github.com/drasros/bs_detector_icueeg). For all clusters, we measured the spike duration, peak-trough ratio, and amplitude measures (Fig. 4; code adapted from https://github.com/jiaxx/waveform_classification).

References

1. Heimans, J. J. & Taphoorn, M. J. Impact of brain tumour treatment on quality of life. *J. Neurol.* **249**, 955–960 (2002).
2. Mitchell, A. J., Kemp, S., Benito-León, J. & Reuber, M. The influence of cognitive impairment on health-related quality of life in neurological disease. *Acta Neuropsychiatr.* **22**, 2–13 (2010).
3. Mueller, W. M. & Morris, G. III Intraoperative and extraoperative identification of eloquent brain using stimulation mapping. *Neurosurg. Clin. North Am.* **4**, 217–222 (1993).
4. Bittar, R. G. et al. Deep brain stimulation for movement disorders and pain. *J. Clin. Neurosci.* **12**, 457–463 (2005).
5. Bronstein, J. M. et al. Deep brain stimulation for Parkinson disease: an expert consensus and review of key issues. *Arch. Neurol.* **68**, 165–165 (2011).
6. Borchers, S., Himmelbach, M., Logothetis, N. & Karnath, H.-O. Direct electrical stimulation of human cortex—the gold standard for mapping brain functions? *Nat. Rev. Neurosci.* **13**, 63–70 (2012).
7. Yamao, Y. et al. Intraoperative dorsal language network mapping by using single-pulse electrical stimulation. *Hum. Brain Mapp.* **35**, 4345–4361 (2014).
8. Lee, B. et al. A single-center experience with the NeuroPace RNS system: a review of techniques and potential problems. *World Neurosurg.* **84**, 719–726 (2015).
9. Trébuchon, A. & Chauvel, P. Electrical stimulation for seizure induction and functional mapping in stereoelectroencephalography. *J. Clin. Neurophysiol.* **33**, 511–521 (2016).
10. Panov, F. et al. Intraoperative electrocorticography for physiological research in movement disorders: principles and experience in 200 cases. *J. Neurosurg.* **126**, 122–131 (2017).
11. Lozano, A. M. et al. Deep brain stimulation: current challenges and future directions. *Nat. Rev. Neurol.* **15**, 148–160 (2019).
12. Ryvlin, P., Rheims, S., Hirsch, L. J., Sokolov, A. & Jehi, L. Neuromodulation in epilepsy: state-of-the-art approved therapies. *Lancet Neurol.* **20**, 1038–1047 (2021).
13. Sui, Y. et al. Deep brain stimulation initiative: toward innovative technology, new disease indications, and approaches to current and future clinical challenges in neuromodulation therapy. *Front. Neurol.* **11**, 1706 (2021).
14. Titiz, A. S. et al. Theta-burst microstimulation in the human entorhinal area improves memory specificity. *Elife* **6**, e29515 (2017).
15. Mankin, E. A. et al. Stimulation of the right entorhinal white matter enhances visual memory encoding in humans. *Brain Stimul.* **14**, 131–140 (2021).
16. Mankin, E. A. & Fried, I. Modulation of human memory by deep brain stimulation of the entorhinal-hippocampal circuitry. *Neuron* **106**, 218–235 (2020).
17. Hochberg, L. R. et al. Reach and grasp by people with tetraplegia using a neurally controlled robotic arm. *Nature* **485**, 372–375 (2012).
18. Fried, I. et al. Cerebral microdialysis combined with single-neuron and electroencephalographic recording in neurosurgical patients. *J. Neurosurg.* **91**, 697–705 (1999).
19. Maynard, E. M., Nordhausen, C. T. & Normann, R. A. The Utah intracortical electrode array: a recording structure for potential brain-computer interfaces. *Electroencephalogr. Clin. Neurophysiol.* **102**, 228–239 (1997).
20. Steinmetz, N. A. et al. Neuropixels 2.0: a miniaturized high-density probe for stable, long-term brain recordings. *Science* **372**, eabf4588 (2021).
21. Jun, J. J. et al. Fully integrated silicon probes for high-density recording of neural activity. *Nature* **551**, 232–236 (2017).
22. Paulk, A. C. et al. Large-scale neural recordings with single neuron resolution using Neuropixels probes in human cortex. *Nat. Neurosci.* **25**, 252–263 (2022).
23. Chung, J. E. et al. High-density single-unit human cortical recordings using the Neuropixels probe. *Neuron* **110**, 2409–2421.e3 (2022).
24. Trautmann, E. M. et al. Large-scale high-density brain-wide neural recording in nonhuman primates. Preprint at *bioRxiv*, 2023.2002.2001.526664 (2023).
25. Chiang, C.-H. et al. Flexible, high-resolution thin-film electrodes for human and animal neural research. *J. Neural Eng.* **18**, 045009 (2021).
26. Abrego, A. M. et al. Sensing local field potentials with a directional and scalable depth electrode array. *J. Neural Eng.* **20**, 016041 (2021).
27. Sellers, K. K. et al. Thin-film microfabrication and intraoperative testing of μECoG and iEEG depth arrays for sense and stimulation. *J. Neural Eng.* **18**, 045014 (2021).
28. Pothof, F. et al. Chronic neural probe for simultaneous recording of single-unit, multi-unit, and local field potential activity from multiple brain sites. *J. Neural Eng.* **13**, 046006 (2016).
29. Ganji, M. et al. Selective formation of porous Pt nanorods for highly electrochemically efficient neural electrode interfaces. *Nano Lett.* **19**, 6244–6254 (2019).

30. Tchoe, Y. et al. Human brain mapping with multithousand-channel PtNRGrids resolves spatiotemporal dynamics. *Sci. Transl. Med.* **14**, eabj1441 (2022).
31. Cui, X. & Martin, D. C. Fuzzy gold electrodes for lowering impedance and improving adhesion with electrodeposited conducting polymer films. *Sens. Actuators A: Phys.* **103**, 384–394 (2003).
32. Khodagholy, D. et al. NeuroGrid: recording action potentials from the surface of the brain. *Nat. Neurosci.* **18**, 310–315 (2015).
33. Ganji, M. et al. Development and Translation of PEDOT: PSS Microelectrodes for Intraoperative Monitoring. *Adv. Funct. Mater.* **28**, 1700232 (2018).
34. Paulk, A. C. et al. Microscale physiological events on the human cortical surface. *Cereb. Cortex* **31**, 3678–3700 (2021).
35. Ulbert, I., Halgren, E., Heit, G. & Karmos, G. Multiple microelectrode-recording system for human intracortical applications. *J. Neurosci. Methods* **106**, 69–79 (2001).
36. Einevoll, G. T. et al. Laminar population analysis: estimating firing rates and evoked synaptic activity from multielectrode recordings in rat barrel cortex. *J. Neurophysiol.* **97**, 2174–2190 (2007).
37. Chari, A., Thornton, R. C., Tisdall, M. M. & Scott, R. C. Microelectrode recordings in human epilepsy: a case for clinical translation. *Brain Commun.* **2**, fcaa082 (2020).
38. Cash, S. S. & Hochberg, L. R. The emergence of single neurons in clinical neurology. *Neuron* **86**, 79–91 (2015).
39. Berger, M. S. & Ojemann, G. A. Intraoperative brain mapping techniques in neuro-oncology. *Stereotact. Funct. Neurosurg.* **58**, 153–161 (1992).
40. Westover, M. B. et al. Real-time segmentation of burst suppression patterns in critical care EEG monitoring. *J. Neurosci. methods* **219**, 131–141 (2013).
41. Pachitariu, M., Steinmetz, N.A., Kadir, S.N., Carandini, M. & Harris, K.D. Fast and accurate spike sorting of high-channel count probes with KiloSort. *Adv. Neural Inf. Process. Syst.* **29**, 4448–4456 (2016).
42. Iwamoto, K. *Novel Patterning Technologies for Semiconductors, MEMS/NEMS and MOEMS 2020*. 11324, 1132405 (International Society for Optics and Photonics, 2020).
43. Luan, L. et al. Ultraflexible nanoelectronic probes form reliable, glial scar–free neural integration. *Sci. Adv.* **3**, e1601966 (2017).
44. Holdgraf, C. et al. iEEG-BIDS, extending the Brain Imaging Data Structure specification to human intracranial electrophysiology. *Sci. Data* **6**, 1–6 (2019).
45. Shi, Y., Kirwan, P. & Livesey, F. J. Directed differentiation of human pluripotent stem cells to cerebral cortex neurons and neural networks. *Nat. Protoc.* **7**, 1836–1846 (2012).
46. Deshpande, A., Mina, E., Glabe, C. & Busciglio, J. Different conformations of amyloid β induce neurotoxicity by distinct mechanisms in human cortical neurons. *J. Neurosci.* **26**, 6011–6018 (2006).
47. Miskinyte, G. et al. Direct conversion of human fibroblasts to functional excitatory cortical neurons integrating into human neural networks. *Stem Cell Res. Ther.* **8**, 1–18 (2017).
48. Egger, R., Narayanan, R. T., Helmstaedter, M., de Kock, C. P. & Oberlaender, M. 3D reconstruction and standardization of the rat vibrissal cortex for precise registration of single neuron morphology. *PLoS Comput. Biol.* **8**, e1002837 (2012).
49. Calabrese, E. et al. A diffusion tensor MRI atlas of the postmortem rhesus macaque brain. *Neuroimage* **117**, 408–416 (2015).
50. Bakker, R., Tiesinga, P. & Kötter, R. The scalable brain atlas: instant web-based access to public brain atlases and related content. *Neuroinformatics* **13**, 353–366 (2015).

Acknowledgements

We are grateful for the technical support from the nano3 cleanroom facilities at UCSD's Qualcomm Institute where the depth electrode fabrication was conducted. This work was performed, in part, at the San Diego Nanotechnology Infrastructure (SDNI) of UCSD, a member of the National Nanotechnology Coordinated Infrastructure, which is supported by the NSF (grant ECCS1542148). We thank Yangling Chou, Aaron Tripp, Fausto Minidio, Daniel J. Soper, and Alexandra O'Donnell for their help in collecting the data.

Author contributions

K.L., A.C.P., Y.G.R., E.H., S.S.C., and S.A.D. initiated the concept and designed the studies. K.L., A.C.P., Y.G.R., D.R.C., K.T., Y.K., J.P., Y.T., J.L., A.M.B., R.V., J.R.M., S.M.R., J.C.Y., A.B., R.M.R., Z.M.W., S.I.F., A.M.R., S.B.H., E.H., S.S.C, and S.A.D. contributed to methodology. K.L., A.C.P., Y.G.R., D.R.C., K.T., Y.K., J.P., Y.T., J.L., A.M.B., R.V., S.M.R., J.C.Y., A.B., R.M.R., Z.M.W., S.I.F., H.S.U., E.H., S.S.C., and S.A.D. contributed to the experiments. K.L., A.C.P., and Y.G.R. led the experiments and collected the overall data. S.A.D., E.H., and S.S.C. contributed to the funding acquisition. S.A.D. and S.S.C. administrated the project. S.A.D., E.H., S.S.C., J.P., M.R., Z.M.W., and S.I.F. supervised the work. A.C.P., K.L., Y.G.R., and S.A.D. co-wrote the paper. K.L., A.C.P., Y.G.R., D.R.C., K.T., Y.K., J.P., Y.T., J.L., A.M.B., R.V., J.R.M., S.M.R., J.C.Y., A.B., R.M.R., Z.M.W., S.I.F., H.S.U., A.M.R., S.B.H., E.H., S.S.C., and S.A.D. provided feedback on the manuscript.

Funding

National Institutes of Health BRAIN® Initiative UG3NS123723-01 (S.A.D.). National Institutes of Health BRAIN® Initiative R01NS123655-01 (S.A.D.). National Institutes of Health NBIB DP2-EB029757 (S.A.D.). National Institutes of Health F32 postdoctoral fellowship MH120886-01 (D.R.C). National Science Foundation Award no. 1728497 (S.A.D.). National Science Foundation CAREER no. 1351980 (S.A.D.). National Science Foundation Graduate Research Fellowship Program no. DGE-1650112 (A.M.B.). MGH—ECOR (S.S.C.). K24-NS088568, R01-NS062092 (S.S.C.). Tiny Blue Dot Foundation (to S.S.C. and A.C.P.). National Institutes of Health BRAIN® Initiative K99 NS119291 (K.J.T.). National Eye Institute R01EY027888 (J.S.P.), William M. Wood Foundation, Bank of America Trustee (J.S.P.)

Competing interests

The authors declare the following competing interests: K.L., Y.G.R., and S.A.D. and the University of California San Diego filed a patent application (#63/584,578, pending) for the manufacture of the novel depth electrodes. A.C.P., D.R.C., Y. T., A.M.R., S.B.H., E.H., S.S.C., and S.A.D. have competing interests not related to this work including equity in Intelecterra Inc. S.A.D. was a paid consultant to MaXentric Technologies. A.M.R. has equity and is a cofounder of CerebroAI. A.M.R. received consulting fees from Abbott Inc and Biotronik Inc. The MGH Translational Research Center has clinical research support agreements with Neuralink, Paradromics, and Synchron, for which S.S.C. provides consultative input. The other authors declare that they have no competing interests.

Additional information

Supplementary information The online version contains supplementary material available at https://doi.org/10.1038/s41467-023-43727-9.

Correspondence and requests for materials should be addressed to Shadi. A. Dayeh.

Peer review information *Nature Communications* thanks Guy McKhann and the other, anonymous, reviewer(s) for their contribution to the peer review of this work. A peer review file is available.

Supplementary Materials for

Flexible, Scalable High Channel Count Stereo-Electrode for Recording in the Human Brain

Keundong Lee[1†], Angelique C. Paulk[2†], Yun Goo Ro[1†], Daniel R. Cleary[1,3], Karen J. Tonsfeldt[1,4], Yoav Kfir[5], John Pezaris[5], Youngbin Tchoe[1], Jihwan Lee[1], Andrew M. Bourhis[1], Ritwik Vatsyayan[1], Joel R. Martin,[1] Samantha M. Russman[1], Jimmy C. Yang,[5] Amy Baohan,[5] R. Mark Richardson,[5] Ziv M. Williams,[5] Shelley I. Fried,[5] Hoi Sang U,[1] Ahmed M. Raslan,[6] Sharona Ben-Haim,[7] Eric Halgren,[8] Sydney S. Cash[2], Shadi. A. Dayeh[1*]

Correspondence to: sdayeh@ucsd.edu

This PDF file includes:

Materials and Methods

1. Study design

Objectives of the study were to: (i) demonstrate implantable thin-film electrodes (μSEEG) produced using reproducible, customizable, and high throughput manufacturing pipeline to be implanted in the brain such as in the operating room using similar brain implant techniques to standard clinical depth electrodes, (ii) use the electrode to record neurophysiologically relevant neural activity in multiple settings and species and; (iii) reach deep brain structures with high spatial sampling resolution and channel count with a much thinner electrode body. Following mechanical and electrochemical characterization of the properties of the new μSEEG devices, we recorded neurophysiological activity in four species (rat, pig, rhesus macaque, and human) under general anesthesia, while awake or under monitored anesthesia care (MAC; **supplementary Table 2**). The primary goal in the physiological recordings was to use sensory (auditory or mechanosensory) or electrical stimulation as well as spontaneous neural activity to determine if the μSEEG devices can record known neurophysiological signatures, whether in the local field potential or the single unit spiking activity (action potentials). All rodent and pig experiments were approved by the UCSD Institutional Animal Care and Use Committee (IACUC) (**supplementary Table 2**). Experimental procedures on rhesus macaques (N=2) were carried out in accordance with the Guide to the Care and Use of Laboratory Animals and approved by the IACUC at Massachusetts General Hospital (MGH; **supplementary Table 2**). We successfully gathered depth recordings of all intended stimulus-evoked activity which included baseline recordings and at least 10 trials per condition (whether injected current level or sensory stimulation). Endpoints for stopping recordings and experiments were determined by the IACUC protocols. For the NHP recordings, we planned to limit μSEEG to 15 minutes-30 minutes for lowering and recording, particularly under anesthesia, to minimize the duration of the case.

Two human participants were recruited to participate in this study at MGH under the Partners Institutional Review Board (now the Mass General Brigham Institutional Review Board which covers MGH). The possibility of conducting research recordings were only discussed with each patient after the decision to proceed with the surgery had been made and following consultation with the treating neurosurgeon and clinical team. Further, we did not enroll patients with clearly impaired decision-making abilities. Both participants were involved voluntarily, provided informed consent, and were informed that participation in the experiment would not alter their clinical treatment in any way and that they could withdraw at any time without altering their clinical care. Finally, case selection and the decision to use the penetrating μSEEG could be inserted into tissue which was identified by the clinical team to be resected during the course of normal clinical care. Data from each participant was de-identified prior to analysis using automatic approaches. In both cases, ongoing spontaneous activity was the control acquiring a baseline recording prior to or throughout the given recording period. Trial numbers for the second participant for the auditory stimulation task within a given subject recording were determined based on a maximum recording time of 15 minutes in the OR setting. We did not include a randomization of subject selection in this study because each recording from each individual was considered a separate dataset. Experimental conditions and a summary of all subjects are presented in **supplementary Table 2**.

Inclusion and analysis of data per experiment was decided based on the following criteria: 1) histological or physiologic confirmation that the electrode was in the targeted barrel cortex in the rodent studies; 2) if the noise level in the recording was low enough to examine neurophysiological signatures. In the former case, we had to reject 6 of 9 rodent implants as the implanted electrodes were not in the rodent barrel cortex. In the latter case of neural activity and noise levels, we were forced to exclude analyses of 2 of the 3 pig recordings due to overwhelming electrical noise. Both the tests performed with humans and non-human primates (NHPs) were included, therefore passing these criteria. Following preprocessing, trial rejection included removing trials with wayward voltage deflections >6 standard deviations from the baseline activity. Overall, only a maximum of 2 or 3 trials were removed per condition across the data sets. These data were not blinded, and we did not include a randomization of subject selection in this study. We did not use power analyses as this particular study involved observational approaches to test the functionality of the devices

2. Fabrication of electrodes

2.1. Long μSEEG fabrication

Supplementary Fig. 1 summarizes the fabrication process of the μSEEG electrode. Polished and cleaned photomask-grade soda lime glass plates (Nanofilm) with dimensions of 7” × 7” × 0.06” were used as substrates for the fabrication. First, a Micro-90 (International Products Corporation) diluted with deionized (DI) water (0.1%) layer was spin-coated on the glass substrate as a release layer for the polyimide electrodes in the last step of the fabrication processes. Subsequently, a sacrificial 5-μm-thick-polyimide (PI-2611 from HD Microsystems) was initially deposited by conventional spin-coating, soft-baking, and curing (340 °C for 3 hrs, 3 °C/min in N_2 ambient) processes. This sacrificial PI layer will serve to separate the device layers, which will be constructed on top of this layer, from the glass plate. Then, a 60-nm-thick Ti hard mask for net layer formation (Ti_{net}) was formed on the sacrificial polyimide layer. The Ti_{net} was proceeded by a standard lithography, descum, metal deposition, and lift-off process using AZ5214E-IR photoresist (MicroChemicals), maskless photolithography system (Heidelberg MLA 150), UV flood exposure system (DYMAX), plasma etcher (Oxford Plasmalab 80), and e-beam evaporator (Temescal). The Ti hard mask contains via patterns with hole arrays with a diameter and a spacing of 5 μm for both, and a 1.5 mm wide and 0.6 mm long rectangular shape for a sheath.

Then, another polyimide layer was spun-coated, soft-baked, and cured at 330 °C for 3 hrs in N_2 ambient following pre-curing of the substrate to dry out any solvent or moisture trapped in the polyimide surface under 340 °C for 3 hrs in N_2 ambient. This polyimide layer is the 1st device layer (1st PI layer) which will be role as the sacrificial bottom layer with net of holes in the final product. Then, a 60-nm-thick Ti sacrificial layer ($Ti_{sacrificial}$) was deposited using same method for the Ti_{net} preparation. The $Ti_{sacrificial}$ also acts as etch-stop layer during the final net formation etching step using O_2 plasma. To increase adhesion between the 1st PI layer and another upcoming polyimide layer (2nd PI layer), hole arrays with a diameter and a spacing of 5 μm for both are patterned along the $Ti_{sacrificial}$ using AZ 1518 (MicroChemicals). Then, the 1st PI layer was selectively etched by O_2 plasma (50 mTorr, 200 W for 7 min), and the photoresist layer was removed by solvent cleaning processes.

After processes on the 1st PI layer, the glass substrate was baked at 330 °C for 2 hrs in N_2 ambient. Then, a 2nd PI layer was coated and cured under 320 °C for 2 hrs in N_2 ambient. Subsequently, metal traces with a width and a spacing of 3 μm for both were formed on the 2nd PI layer. Metal traces were composed of Cr/Au (10/250 nm) and the entire lithography, deposition, and lift-off process was repeated on top of the first metal lead layer to form Cr/Au/Cr/Au (10/250/10/250 nm) traces. This double-patterning process was employed to increase yield and reduce risk of photoresist particles from compromising the thin traces.

After the double-layer metal leads formation, a 30 μm-diameter-PtAg alloy was formed selectively on the individual micro-contact recording sites by photolithography, descum, and PtAg alloy co-sputtering using the maskless photolithography system with NR9-6000 (Futurrex) photoresist, plasma etcher, and DC/RF magnetron sputter (Denton Discovery 18), respectively. A 60-nm-thick Ti capping layer (Ti_{cap}) was deposited on top of PtAg alloys to prevent oxidation in air or under oxygen plasma in the following processes. The detailed fabrication methods and characteristics of PtNRs can be found elsewhere[29, 30]. Notably, this process involves a selective etching of silver in a dealloying process, leaving behind non-toxic platinum.

A 3rd polyimide layer (3rd PI layer) was then coated and cured under 300 °C for 1 hr in N_2 ambient. On top of the 3rd PI layer, a 60-nm-thick-Ti hard mask ($Ti_{outline}$) was deposited and AZ5214E-IR photoresist was coated on top of the $Ti_{outline}$ and patterned to define the outline of the electrodes. Then, SF_6/Ar plasma was used to selectively etch the $Ti_{outline}$ through the photoresist. To accomplish a 1st deep etch step, 3 hrs of O_2 plasma was performed to etch 3rd, 2nd and 1st PI layers until exposing the Ti_{net} on the sacrificial PI layer.

Following the 1st deep etch process, a-8-μm-thick AZ12XT-20PL-10 (MicroChemicals) was spun-coated and patterned to open via holes for recording sites and printed circuit board (PCB) contact pads, and the outline of the electrodes. Then, SF_6/Ar plasma was used to etch Ti_{net} and expose the surface of the 3rd PI layer on the recording sites and the sacrificial PI layers along the outline of the electrodes. Subsequently, the exposed PI layers were etched by O_2 plasma for 1 hr.

To protect PI layers from dealloying process to form PtNRs using nitric acid, a 100-nm-Ti ($Ti_{passivation}$) was conformally deposited using sputtering system and a 1-μm-thick parylene C was additionally coated using a parylene deposition system (Specialty Coating Systems 2010 Labcoter). To open via holes for recording sites, a-8-μm-thick AZ12XT-20PL-10 was spin-coated and patterned again. Then, O_2 plasma and subsequent SF_6/Ar plasma was used to etch the parylene C and Ti layers including the $Ti_{passivation}$ and Ti_{cap} to expose the PtAg alloys. The glass substrate was immersed into 60 °C nitric acid for 2 min for dealloying of PtAg alloys and rinsed in de-ionized (DI) water. The microscopic morphology of the PtNR is shown in the scanning electron microscope (SEM) images (**Fig. 1b**).

The parylene C and $Ti_{passivation}$ were removed by O_2 plasma and 6:1 buffered oxide etchant (BOE), respectively. Then, the glass substrate was immersed in DI water to delaminate the electrodes from the glass substrate with the dissolution of the underlying Micro-90 layer.

The delaminated electrode was then flipped and transferred onto a carrier glass wafer. Following the flip transfer, the net of hole arrays was formed on the 1st PI layer by O_2 plasma removing the sacrificial PI layer and selectively etch the 1st PI layer through the

via openings in the Ti_{net}. The etching time was set longer to obtain clean opening of hole arrays. Note that the 2nd PI layer was protected, during the over etching procedure, by the $Ti_{sacrificial}$ prepared between 1st and 2nd PI layers. Lastly, the Ti_{net} and $Ti_{sacrificial}$ were all dissolved by BOE and the electrode was immersed in DI water for ~6 hrs to rinse any residual BOE.

2.2. Stylet insertion

Medical grade stainless-steel 316 stylets (Ø 125 µm) were used as a shuttle to guide the µSEEG electrode to a target region. The stainless-steel was chosen as a shuttle material over a tungsten rod or a silicon shuttle because of its hydrophilic surface, which helps to avoid adhesion between the hydrophobic polyimide surfaces[1]. These stainless-steel shuttles are the standard stylets used for the implantation of clinical depth electrodes. The stainless-steel stylet was mechanically polished to have smooth surface at its tip to prevent mechanical damages of the µSEEG electrode during the stylet insertion (**supplementary Fig. 4**).

The stylet was inserted through the sheath on the stylet bottom layer and travelled along the space between the stylet upper and bottom layers where the Ti sacrificial layer was etched away. The retractable stylet provides rigidity to the polyimide electrode tip and supports implantation to the cortex without electrode deformation. The stylet insertion procedure is as follows: First, the µSEEG electrode and the stylet was placed on a clean glass substrate (**supplementary Fig. 2a**). Then, the stylet was inserted through the stitch holes to restrict lateral movement of the stylet and the sheath of the electrode (**supplementary Fig. 2b**). To ensure that the stylet is aligned with the center of the µSEEG, the center of the stitch hole arrays is aligned with the center of the sheath. The diameter of each hole is 800 µm, and they are spaced 2 mm apart. **Supplementary Fig. 2c** shows a zoomed-in image of the sheath during stylet insertion. The insertion process was initiated by opening the sheath with support from a tungsten probe. Once the sheath was opened, the stylet was slid into the sheath, and the tungsten probe was gently removed. Subsequently, DI water was sprayed along the electrode strips to open the space between the stylet upper and lower layers. In a few seconds after DI water spraying, the stylet could be travelled along the space (**supplementary Fig. 2d and supplementary Fig. 2e**) and finally reached to the tip of the electrodes (**supplementary Fig. 2f**). **Supplementary Fig. 2g** shows scale of the µSEEG electrode after the stylet insertion and comparison with the clinical electrode indicating that a length of the stylet inserted part of the µSEEG electrode is long enough to access to the deep brain structure. A cross-section view SEM image (**supplementary Fig. 2h**) shows the stylet upper and bottom layers with the stylet in between after recordings from non-human primate (NHP). The tip of the µSEEG electrode was deliberately opened by a razor blade to observe cross-sectional details of the µSEEG electrode with bio-materials remained on. **Supplementary Fig. 2i** displays a cross-section SEM image of the µSEEG electrode after the stylet retraction, showing negligible deformation and suggesting that the stylet insertion and retraction does not cause permanent deformation of the probe sheath. During the stylet insertion, the flexibility of the polyimide allows the µSEEG electrode to adjust its shape, inflating it from two straight lines with a length of 1.24 mm to an oval shape with a longer length of 1.02 mm and a shorter length of 0.25 mm, which corresponds to the diameter of the stylet. This indicates that the stress on the polyimide

is relaxed as the electrode shape changes during stylet insertion. This is also observed under optical microscope (OM) image (**Supplementary Fig. 2e**) showing different light reflection from the edge of the electrode depending on whether the stylet has already been implanted or is yet to be implanted.

2.3. Short µSEEG fabrication

The short 64 channel µSEEG electrode has a large space (flaps) near the interconnection metal leads for surgeon's convenience for electrode handling. It is also designed to bond with anisotropic conductive films (ACF) with commercial off-the-shelf ribbon cables to connect the electrode to the external characterization circuitry (**supplementary Fig. 8a**). The electrode consists of three polyimide (or parylene C) layers to not only passivate metal leads, but also carry the stylet during implantation (**supplementary Fig. 8b**). Au was used to serve sacrificial layer to separate 1st and 2nd polyimide layers for the stylet insertion by dissolving of Au layer using Au etchant (TFA, Transene Company, Inc.). A metal lead layer of Cr/Pt (20/100 nm) was embedded between 2nd and 3rd polyimide layers, but recording electrodes were via-opened. To enhance recording qualities, PEDOT:PSS was electro-deposited on the Cr/Pt recording electrodes. PEDOT:PSS was electrodeposited from 0.01 M 3,4-Ethylenedioxythiophene (EDOT) in 2.0 g per 100 mL Poly(sodium 4-styrenesulfonate) aqueous dispersion under galvanostatic conditions at a potential of 0.9 V versus Ag/AgCl in a three electrode setup, i.e., Ag/AgCl electrode as a reference electrode, a large Pt electrode as a counter electrode, and the Pt contacts on the probes as the working electrodes, at a constant temperature of 27 °C using a Gamry potentiostat (Gamry Interface 1000E; Gamry Instruments). Polymerization was driven for 20 s at current density of 5 mA/cm^2.

After the stylet was inserted in the µSEEG electrode, the large space and bonding pad regions were bent due to strain of the polyimide layers because of its thickness and geometry (**supplementary Fig. 8c**), but it is confirmed that a region for the recording electrodes remained straight with the stylet (**supplementary Fig. 8d**) and PEDOT:PSS electrodes, Cr/Pt metal leads, and polyimide layers are not damaged (**supplementary Figs. 8e** and **8f**). **Supplementary Fig. 8e** also displays a detail of the electrode layout showing hole arrays patterned along the metal leads to help wet etching of the Au sacrificial layer. The diameter and center to center spacing of electrode sites is shown as 20 and 60 µm, respectively (**supplementary Fig. 8f**), and the electrode consisted of 64 channels along 3.80 mm in a laminar manner. The dimension and the number of electrodes can be adjusted based on the target of merit.

Electrochemical impedance spectroscopy (EIS) of the electro-deposited PEDOT:PSS was performed, in 1X phosphate buffer saline (PBS) solution (**supplementary Fig. 8g**). Three electrode configuration i.e., PEDOT:PSS electrodes as the working electrode, Ag/AgCl electrode as a reference electrode, a large platinum electrode as a counter electrode was used. 10 mV root mean square (RMS) sinusoidal signal with zero DC bias were applied and the frequency was swept from 1 Hz to 10 kHz using a Gamry potentiostat (Gamry Interface 1000E; Gamry Instruments). Electrochemical impedance at 1 kHz is commonly used as the benchmark for the characterization of neural electrodes, as this frequency corresponds to spiking activity[2]. The average impedance magnitude of PEDOT:PSS electrodes across 64 channels was 33.0 ± 2.47 kilohms at 1 kHz and their phase indicates their faradaic electrochemical interfaces. After stylet insertion, the

average impedance magnitude maintained similar values of 35.0 ± 3.67 kilohms on 64 channels, still lower and consistent contrast to Pt electrodes (**supplementary Fig. 8h**), indicating that the stylet was successfully inserted between the polyimide layers without any damage to the channel or PEDOT:PSS separation from Pt electrodes. **Supplementary Fig. 8i** displays averaged impedance magnitude at 1 kHz for 7 PEDOT:PSS μSEEG electrodes, before and after stylet insertion. The channel yield before and after stylet insertion is 99.8 ± 0.5 % and 99.3 ± 0.7 %, respectively. The channel yields below reflect the negligible electrode losses during the stylet insertion.

2.4. Surface μECoG fabrication

We fabricated a μECoG electrode array to use during depth recordings to address the location of the barrel cortex before μSEEG implantation. The μECoG electrode array was placed on the region where the barrel cortex is expected to be located and we performed recordings with whisker airpuff stimulation. After we confirmed that the μECoG electrode array captures activities from the whisker airpuff stimulation, the μSEEG was implanted between the columns of the μECoG electrode array. Parylene C was chosen as the surface μECoG electrode material because of its superior conformability and hydrophobic surface which makes stable electrical and mechanical contact with the surface of the cortex[3]. The μECoG electrode is designed to perform dual column recordings while the μSEEG electrode measures intracortical signals between the columns (**Supplementary Figs. 13a and b**). It is also designed to bond with ACF with commercial off-the-shelf ribbon cables to connect the device to the external characterization circuitry (**supplementary Fig. 13a**). The fabrication process of parylene C μECoG electrode was reported elsewhere [4, 5].

First, an anti-adhesion layer, Microo-90 diluted with DI water (0.1 %) was spun-coated on a 4” Si carrier wafer to enable parylene C device release from the Si carrier wafer. A 1st parylene C layer (3 μm) was deposited on top of the anti-adhesion layer by chemical vapor deposition (Specialty Coating Systems 2010 Labcoter). A Cr/Au/Ti (10/100/50 nm) metal lead layer was evaporated and patterned via lift-off process. Cr layer serves as an adhesion layer between Au conduction layer and parylene C. Ti layer was deposited to protect Au layer during later via dry-etching process. A 2nd parylene C insulation layer (3 μm) was deposited. A Ti (50 nm) layer was deposited and patterned via lift-off process on the second parylene C layer as an etch hard mask against O2 plasma etching. The Ti hard mask was patterned to define 1) via openings of the Au electrode sites and bonding pads, 2) shape of the device body and 3) perfusion holes on parylene C layers. Perfusion holes can help minimizing the excessive cerebrospinal fluid (CSF) around the electrode sites[6]. The Ti hard mask and protection layer was removed by BOE and rinsed with DI water, leaving fresh Au surface at the electrode sites. The parylene C device was released from the Si carrier wafer by removing Micro-90 with DI water. The bonding pad region of the probe (Cr/Au) was bonded with ACF and commercial off-the-shelf ribbon cables and additionally encapsulated by kapton tape to prevent saline or CSF leakage (**supplementary Fig. 13c**). To enhance recording qualities, PEDOT:PSS was electrodeposited on the surface of Au electrode sites using the technique described above. The surface probe consists of two column 32 channels along 3.12 mm in a laminar manner and the diameter and pitch of electrode sites is 20 and 100 μm, respectively (**Supplementary Figs. 13d to f**).

Electrochemical impedance at 1 kHz was measured using Intan RHD2000 USB interface board (Intan Technologies) in 1X phosphate buffer saline (PBS) solution with a stainless-steel needle as a reference electrode (**supplementary Fig. 13g**). The average impedance magnitude of Au electrodes was 739 ± 85.4 kilohms, which was decreased to 33.6 ± 3.21 kilohms after PEDOT:PSS electrodeposition on Au electrodes, with uniform distribution of the impedance across the channels (**supplementary Fig. 13h**).

3. Mechanical characterizations of μSEEG electrodes

3.1. μSEEG insertion benchtop tests

Insertion of the prototype μSEEG was tested on a phantom brain model. A transparent brain phantom gelatin model was prepared by mixing and dissolving a gelatin powder (Knox; Kraft Foods, Inc.) with weight concentration of 5.3 %. Knox gelatin with this concentration was reported to provide similar shear modulus to the mouse brain[7] and its transparency helps in visualization of the μSEEG electrode movement in the gel. We designed and printed a custom-made 3D printed holder that can be attached to the stereotaxic micromanipulator while holding the prototype μSEEG (**supplementary Fig. 7a**). The prototype μSEEG, held by the 3D print holder, was slowly inserted into the gelatin using the z-axis control handle of the stereotaxic micromanipulator. After the prototype μSEEG was inserted, the stainless-steel stylet was manually grasped by a tweezer and extracted from the prototype μSEEG. The implantation of the prototype μSEEG and displacement after stylet extraction were recorded using a camera with a macro lens (**supplementary Fig. 7b**). The prototype μSEEG was implanted without any deformation with help of the stylet. Also, the displacement of the prototype μSEEG before and after stylet extraction was less than 10 μm.

3.2 Pull measurement of μSEEG

We investigated tensile stress of μSEEG using pull measurement to examine the mechanical stability of our electrode and compare it with clinical depth electrode (PMT electrode). The μSEEG was integrated on the pressure sensor system (voice coil-powered linear actuator system with internally integrated force sensor; V-275 PIMag Voice Coil Linear Actuator). A customized 3D printed sample mount was attached onto the actuator (**supplementary Fig. 5a**) and a tip of the μSEEG was placed on the sample mount followed by strong fixation using epoxy. Rest of the electrode was attached on a main body of the system and fixed by epoxy as well (**supplementary Fig. 5b**). We applied force to the actuator to exam tensile strength upon the electrodes break (indicated by red arrow) and obtained that the critical tensile strength. The critical strength of parylene C μSEEG and polyimide μSEEG are 0.6MPa (24 mN with an area of the stress of $4e^{-8}$ m^2) and 1 – 2.5 MPa (16 – 37 mN with an area of the stress of $1.5e^{-8}m^2$), respectively. Meanwhile, the PMT electrode that was anchored on two polyurethane tube regions around a Pt contact was damaged when 14 kPa (48 mN with an area of the stress of $3.5e^{-7}m^2$) was applied to the PMT electrode (**supplementary Fig. 5c**). The illustration of the area of the stress of electrodes is illustrated in **supplementary Fig. 5d**.

Mechanical stress introduced by stylet insertion was investigated using finite element method (FEM) analysis (**supplementary Fig. 9a** and **b**). The analysis indicates that the maximum strength applied to the films during the stylet insertion (0.11 MPa) are lower than the critical strength of the polyimide (1 – 2.5 MPa) and parylene C (0.6 MPa), as shown in **supplementary Fig. 9a.** Deformation of the films are lower than 4 μm, which

can be considered as negligible from the scale of the electrodes, as shown in **supplementary Fig. 9b**. In theory, according to the simulation, the electrode should not sustain damage during stylet insertion. However, in practical scenarios, there are additional variables that can introduce stress to the electrode, such as misalignment of the electrodes in DI water (twisted or curved) and the angle at which the stylet is inserted, which may not be perfectly horizontal to the surface. While the polyimide layers are resilient and can withstand external stress arising from real-world conditions (**supplementary Fig 9c** – **e**), the parylene C layers appear to be approaching their critical limits (**supplementary Fig 9f – h**).

3.3 Endurance of µSEEG

The reliability of µSEEG was evaluated through an accelerated aging test to validate the use of our electrode in semi-chronic applications. The electrode was immersed in 50 °C saline solutions for over 74 days to assess its yield after >150 days of implantation[8]. OM images of the µSEEG before and after the aging test showed negligible changes (**Supplementary Fig 6a** and **6b**), indicating good structural integrity. During the test, impedance measurements at 1 kHz exhibited minor fluctuations in both mean and standard deviation values (**Supplementary Fig 6c**). Prior to the accelerated aging test, we measured 49 functional contacts with an average impedance of 94±26 kΩ. After the test, we observed 52 functional contacts with an average impedance of 96±28 kΩ (**Supplementary Fig 6d**). These results demonstrate the robustness of the µSEEG electrode even under accelerated aging conditions. In addition, we performed 84,000 cycles of lead bend testing, exceeding 90° bends as per EN 45502 standards, to validate the capability of our electrode for general application in active implantable medical devices[5]. A robotic gripper model 2F-140 (Robotiq) was used for the bending tests. After bending, 50 contacts (average impedance of 93±27 kΩ) were functional. A few changes in number of functional channels are attributed to different contact latching between the PCB and the custom ironwood electronics socket that requires latching to form robust electrical connections between PCBs and pins in the socket on the acquisition board and is minimal indicating resilience of our electrodes to bending cycles.

3.4 Mechanical stability of PtNR

PtNR µSEEG electrodes (N = 3) after extraction from the NHP brain was investigated by SEM (**supplementary Fig. 11**). It was observed that PtNRs remained intact underneath the adsorbed tissue that are left on the surface of the electrodes (**supplementary Fig. 11a**). A higher magnification SEM image (**supplementary Fig. 11b**) shows PtNRs morphology similar to that of before implant (**Fig. 1b**).

4. Rat recording

4.1. Acute rat recordings: surgical procedures and sensory stimulation

Acute *in vivo* electrophysiological recordings were performed on the rat primary somatosensory “barrel” cortex (S1) with the µECoG electrode and the µSEEG electrode. The rat was anesthetized and craniotomy was performed under isofluorane anesthesia. The body temperature of the rat was maintained at 37 °C with a heating pad. Craniotomy

and dura removal were performed over the right barrel and surrounding cortical region. Following electrode placement, the rat was transitioned to ketamine/xylazine anesthesia for recording.

Tactile stimulation was performed by delivering air puffs to the whisker pad. Air puffs were pressure-injected through a glass micropipette using a PV830 pneumatic picopump (World Precision Instruments, Inc.) with 1 s pulses (n>10 trials per location). The contralateral (left) whiskers with respect to the recording sites were deflected by air puff (± 2 mm). First, the whole contralateral whiskers (multi-whisker) were stimulated. Then single whiskers (C1-3, D1-3, E1-4) were stimulated by placing the pipette as close as possible to each whisker to avoid deflection of the neighboring whiskers. Recording data were collected for 60 s for each whisker.

4.2. Acute rat recordings: histology of the rat brain

Prior to the insertion to the cortex, the back of the tip of the μSEEG electrode was painted with a fluorescent dye, DiI (1,1′-Dioctadecyl-3,3,3′,3′-tetramethylindocarbocyanine perchlorate, 0.1% in ethanol; Invitrogen) to visualize the μSEEG electrode track in histopathological sections and verify the placement of the μSEEG electrode with respect to cortical depth. Following the electrophysiological recordings, rats were sacrificed and perfused with 4% paraformaldehyde (PFA), and the brains were fixed for 2 hrs in 4% PFA. Brains were transferred to a 30% sucrose solution, and then embedded in OCT matrix and stored at -80. Slices were sectioned on a cryostat at 50 μm. Free-floating sections were washed in phosphate buffered saline (PBS) + 0.1% Triton for 10 min, and then incubated in 1:50 Neurotrace 500/525 (ThermoFisher) for 30 min. Sections were washed in PBS + 0.1% Triton for 10 min, followed by PBS. Sections were mounted on slides and coverslipped using ProLong Gold (ThermoFisher). Slices were imaged using a Keyence BZX-700 at the UCSD Department of Neuroscience Microscopy Core (supported by NS047101). From the histology result (**supplementary Fig. 14**), the tip of the acute μSEEG electrode was estimated to be 1750 μm deep in the cortex, reaching layer VI.

4.3. Chronic rat recordings: implantation of μSEEG electrode, surgical procedures, and sensory stimulation

The short 32 channel μSEEG electrode for chronic rat recordings consists of 32 channels of microcontacts that are spread along the 2-mm-scale μSEEG electrode, which are connected to the metal pads for interfacing with PCB (**supplementary Fig. 22a**). The metal pads and PCB are bonded by Ag epoxy. The back side of the PCB has electrical and mechanical contact with zero-insertion-force (ZIF) connector. The ZIF connector was activated with a lever to close the contact after flat flexible cable (FFC) insertion into the ZIF connector to make secure electrical and mechanical contact.

For implantation of the chronic μSEEG electrode, first, a C-shape mount was fixed onto the skull near the craniotomy using screws and it was then bonded with the headstage using a super glue. Then, the chronic μSEEG electrode with PCB and ZIF with FFC inserted was temporarily attached on the glass slide and the glass slide was connected to the micromanipulator (**supplementary Fig. 22b**). During the implantation, position of the chronic μSEEG electrode was precisely controlled by micromanipulator. After the implantation, FFC was unplugged from the ZIF and the chronic μSEEG electrode with

PCB and ZIF are securely protected by the headstage and fixed onto the skull due to the screw-fixed mount. The craniotomy was sealed by ultraviolet curable medical glue (Tetric EvoFlow). Stimuli to induce neural activity included whisker, paw, and trunk mechanical stimulation including air puffs delivered >10 times/trials and the recording data from each trial were averaged.

During the acute experiment, implanting the μSEEG electrode in the rat barrel cortex was relatively straightforward as we had the flexibility to create a larger craniotomy and position the μECoG arrays to locate the barrel cortex before electrode implantation. However, for chronic implantations, additional preparations are necessary. Firstly, the headstage must be securely fixed to the rat's skull prior to the implantation. Secondly, it is crucial to keep the size of the craniotomy as small as possible to minimize the risk of infections. These requirements increase the complexity of implanting the μSEEG electrode into the rat barrel cortex and resulted in successful detection of strong whisker stimulation-evoked activities in only 3 out of 9 rats.

4.4. Chronic rat recordings: histology of the rat brain

At the termination of the chronic recordings (by four weeks after implant), brains were removed and briefly (2 hrs) fixed in 4% PFA. The cortices were removed and flattened between glass slides in PBS, and then the flattened cortex further fixed in 4% PFA overnight, and then allowed to sink in 30% sucrose. For measuring implantation scar, rats were implanted with a dummy clinical electrode or μSEEG and allowed to recover for two weeks (n = 1 / electrode). Animals were perfused with 4% PFA and then sunk in 30% sucrose. Whole brains or flattened cortices were sectioned on a cryostat in the horizontal plane from at 40 μm. Sections were washed with PBS and stained overnight with one or more of the following: chicken anti-NeuN (1:500, Sigma ABN91), Cy3-conjugated mouse anti-GFAP (1:1000, Sigma C9205), rabbit anti-VGLUT2 (1:500, Abcam ab216463). After wash, slices were incubated in secondaries of goat anti-chicken 488 (Sigma SAB4600039), goat anti-chicken 647 (Sigma SAB2600184), or goat anti-rabbit 488 (ThermoFisher A-11008) at 1:300 for 1 hour, rinsed, and mounted with ProLong with DAPI. Slides were imaged on a Nikon Eclipse Ti2-E with a DS-Q12 CMOS camera at the UCSD Nikon Imaging Core Images were analyzed using ImageJ (**supplementary Figs. 10a** to **d**). In our observations from four chronic (2 weeks) placement, we observed no significant difference in the number of Neun-positive cells surrounding the lesion between the μSEEG and the clinical grid, but there was a small non-significant improvement with the μSEEG electrode (2-way ANOVA, $F(1, 72) = 3.290$, $P = 0.0739$) (**supplementary Figs. 10e** and **10f**).

4.5. Rat recording methods

We successfully gathered depth recordings of all intended stimulus-evoked responses and gathered tissue for histological evaluation. These data were not blinded, and we did not include a randomization of subject selection in this study. The data from the μSEEG electrode was acquired at 15 – 20 kHz and filtered by default Intan settings with cutoffs of 1 Hz to 7.5 kHz. The impedance tests of the electrodes during the experiments and recordings in the animals carried out using the Intan RHD2000 software from Intan Technologies (Los Angeles, CA). Data was extracted and processed using MATLAB (Mathworks, Natick, MA).

5. Pig recording

5.1. Pig surgical details and spinal cord stimulation

The pig experiments were approved by the University of California San Diego (UCSD) Institutional Animal Care and Use Committee. Yucatan pigs were induced with isoflourance and intubated. Once anesthetized, the animal was mounted into a stereotaxic frame in the prone position. Vital signs were monitored including heart rate, blood pressure, EtCO2, respiratory rate, and blood oxygenation. The cranial surgical site was centered over the motor cortex of the frontal lobe and somatosensory cortex of the parietal lobe. After immobilization, a skin incision (2-4 inches long) was made and unilateral craniotomy was performed using a high speed surgical drill. The bone was removed to create a window approximately 25 mm x 15 mm. The underlying dura was incised and reflected medially towards the sagittal sinus. The cortex was hydrated with normal saline solution. A flexible sterile multielectrode implant was then placed on the surface of the exposed cortex. After placement of the electrode into the cortical surface, the electrode ribbon (<1 cm in width) was connected to an Intan recording controller. For spinal exposure, a midline incision and laminectomy were performed with a Kerrison rongeur to sufficiently expose the target thoracolumbar enlargement of the spinal cord. Following laminectomy, a longitudinal incision was made in the dura and arachnoid tissue was dissected to allow for exposure of the spinal cord. Spinal cord stimulation was performed with a handheld Ojemann stimulator with two ball tips (Radionics Inc., Burlington, MA) with 0.5 cm spacing between electrode tips. Isoflurane anesthesia was halted following completion of surgical procedures and was replaced with IV Propofol for the duration of the stimulation testing.

5.2. Pig recording methods

We successfully gathered depth recordings of all intended stimulus-evoked responses. These data were not blinded, and we did not include a randomization of subject selection in this study. The data from the μSEEG electrode was acquired at 15 – 20 kHz and filtered by default Intan settings with cutoffs of 1 Hz to 7.5 kHz. The impedance tests of the electrodes during the experiments and recordings in the animals carried out using the Intan RHD2000 software from Intan Technologies (Los Angeles, CA). Data was extracted and processed using MATLAB (Mathworks, Natick, MA).

6. NHP recording

Experimental procedures on rhesus macaques were carried out in accordance with the Guide to the Care and Use of Laboratory Animals. All efforts were made to minimize discomfort, and the Institutional Animal Care and Use Committee at the Massachusetts General Hospital monitored care and approved all procedures. We tested μSEEG electrodes in two settings: 1) recording from a short μSEEG in an anesthetized NHP the operating room for recording visual cortical dynamics and 2) recording from a long μSEEG in an awake NHP with the electrode lowered through an implanted chamber with a standard Microdrive (**supplementary Table 2**).

An intraoperative, intracranial neurophysiology recording were acquired from one adult male rhesus macaque (*Macaca mulatta*, age 11). The macaque was placed under

general endotracheal anesthesia (isoflurane) and placed into a stereotactic frame (Kopf; Kujunga, CA). A craniotomy over the visual cortex was performed using standard anatomic landmarks, and cortex was carefully exposed and the short μSEEG electrode was implanted. Signals were recorded using a custom Intan Recording System as described previously [4, 9].

In the awake NHP preparation, one adult male rhesus macaque (*Macaca mulatta*, age 14) was implanted with two recording chambers that allowed access parietal lobe, temporal lobe, and thalamic brain regions. A fitted Microdrive was placed on the top of the chamber to allow insertion through the dura. Following recording, trajectories were calculated by mapping the depths calculated from the Microdrive to a preoperative magnetic resonance imaging (MRI) and a postoperative CT of the chamber locations using MANGO (San Antonio, TX). To visualize the locations in 3D, we used the Scalable Brain Atlas with the Calabrese atlas (https://scalablebrainatlas.incf.org/; [10, 11] exported into Blender (https://www.blender.org/). The electrode was lowered acutely to three different depths to record neural activity. No clear adverse behavioral effects were observed before or after electrode implant or explant. Recordings of the long μSEEG involved the use of the 1024 Intan Recording system with a 1024 channel Intan chip clamped device developed for recording thin film microelectrodes [5].

For both preparations, data from the μSEEG electrode was acquired at 30 kHz and filtered by default Intan settings with cutoffs of 1 Hz to 7.5 kHz. The majority of the data was acquired using OpenEphys acquisition graphic-user interface software ([12]; http://www.open-ephys.org/), with the impedance tests of the electrodes during the experiments carried out using the Intan RHD2000 software from Intan Technologies (Los Angeles, CA). Data was extracted and processed using MATLAB (Mathworks, Natick, MA). Data recorded from the μSEEG electrode was down-sampled to 1000 Hz.

7. Human recording

7.1. Recordings in human cortex the operating room

Intraoperative recordings were performed in two participants who underwent a neurosurgical procedure at Massachusetts General Hospital (MGH). This study was approved by the Partners Institutional Review Board (now the Mass General Brigham Institutional Review Board which covers MGH). Both participants were involved voluntarily, provided informed consent, and were informed that participation in the experiment would not alter their clinical treatment in any way and that they could withdraw at any time without altering their clinical care. The patients were approached following already being scheduled to remove a portion of the left anterior temporal lobe for the treatment of epilepsy or tumor removal. The possibility of conducting research recordings were only discussed with each patient after the decision to proceed with the surgery had been made. Neither patient was medically unstable or required emergency or urgent surgery. All decisions to proceed were made following consultation with the treating neurosurgeon and clinical team. Further, we did not enroll patients with clearly impaired decision-making abilities (as determined by the primary clinical team or physician caring for the patient). The time allowed for dedicated research recording was limited per subject to minimize risk. We tested the short μSEEG electrodes, which were inserted into tissue the clinical team identified would be resected following recording. One participant (HS1) was under general anesthesia but underwent clinically indicated stimulation of the cortical

surface prior to resection (**Supplementary Video 1**). The second participant (HS2) underwent awake cognitive testing under monitored anesthesia care (MAC) with electrocorticography (intracranial EEG) during surgery.

Neural signals were recorded using a custom Intan Recording System as described previously [9, 13, 14]. Data from the μSEEG electrodes were acquired at 30 kHz and filtered by default Intan settings with cutoffs of 1 Hz to 7.5 kHz using the OpenEphys acquisition graphic-user interface software ([12] http://www.open-ephys.org/), with the impedance tests using the Intan RHD2000 software from Intan Technologies (Los Angeles, CA).

7.2 Auditory Task in the Operating Room

The Auditory M-sequence block involves 100 trials where each trial involves a red fixation cross on a grey background while one of either two tones are played in the background. The choice of tone, whether 250 Hz or 500 Hz, per trial was randomly sampled from sequences of black or white designations pulled from an m-sequence distribution [12, 15, 16]. These frequencies and tones have been used before to demonstrate auditory specificity intracranially in humans [17].

8. Neural Data Analysis

Data was extracted and processed using MATLAB R2020a (Mathworks, Natick, MA). Data recorded from the μSEEG electrode was down-sampled to 1000 Hz. To remove noise, the data were re-referenced by subtracting the median signal of all the channels. Local field potentials (LFPs), multi-unit activity power (300-2000 Hz) high gamma activity (HGA; 65-200 Hz) evoked by tactile stimuli were investigated. Power spectral analyses to examine the dynamics in the different conditions were performed by taking the real value of the Morlet wavelet coefficient (power) at a 1-Hz spectral resolution using a moving window of 0.5 sec moving every 10 ms, calculated using the Fieldtrip toolbox (www.ru.nl/fcdonders/fieldtrip, [18]). In the case of direct electrical stimulation, stimulation artifact was removed using a Tukey-windowed median filter in the 20 ms around the onset of the pulse for the single pulses [19]. Other measures of multi-unit activity involved measuring high gamma power (70-190 Hz) by taking the absolute value of a Hilbert transform following band pass filtering.

Current source density (CSD) provides information on the distribution of synaptic inputs for the generators [20]. Here, CSD was calculated from LFP using the δ-source inverse CSD (iCSD) method, refined by Petterson et al. [21]:

$$(1)\ C = F^{-1}\Phi$$

where C and Φ represents matrix for CSD and LFP, respectively. The transformation matrix F is described by

$$(2)\ F_{ji} = \frac{h^2}{2\sigma}\left(\sqrt{(j-i)^2 + (R/h)^2} - |j-i|\right)$$

where h is the spacing between adjacent electrode, σ is the conductivity of the cortex and R is the radius of infinitely thin current-source discs. Here we set the σ and R as 0.3 S/m and 0.25 mm, respectively. Since CSD is calculated from LFP data of adjacent electrodes, each column was separated for calculation of CSD and the column that included a greater number of low impedance (<500 kΩ) channels (30 out of 32) was selected for the CSD analysis.

We detected bursts and calculated the burst suppression ratio (BSR) using an automated method [22] (https://github.com/drasros/bs_detector_icueeg). On the per-channel basis, this method labels each time sample as either burst or suppression. Briefly, the method uses the previous data with each channel and applies the following equations:

$$(3)\ \mu t = \beta\ \mu t\text{-}1 + (1\text{-}\beta)\ xt$$
$$(4)\ \sigma t2 = \beta\ \sigma t\text{-}12 + (1\text{-}\beta)\ (xt - \mu t)2$$
$$(5)\ zt = \delta[\sigma t2 < \theta]$$

Where xt is the value of the normalized signal of one channel at time t, μt and σt2 are current values of the recursively estimated local mean and variance, respectively. Finally, zt is an indicator function that labels each data point as either a burst (0) or suppression (1). The value of β determines the balance between the effect of recent and past data set based on previously trained data [22]. The classification threshold θ (i.e., the value above which a data point should be classified as burst) was adjusted to evaluate our dataset visually with values of θ = 100, 2000, 4000. The value of θ = 2000 was selected to reliably identify burst and suppression induced by general anesthesia. The burst suppression ratio for each recording in an anesthetized patient (N = 1) and NHP (N = 1) was evaluated as the proportion of suppression-labeled samples in a moving window (1 s duration, no overlap).

Spike sorting was performed on the long μSEEG recordings from an NHP using Kilosort 2.5 [23]; https://github.com/MouseLand/Kilosort) with further determination of single units versus multi-unit activity performed in post processing using Phy (https://github.com/cortex-lab/phy) and then manually curated using in-house MATLAB code to visually inspect the template as well as the waveforms assigned to each cluster. The Kilosort 2.5 parameters included: Nblocks = 0 – as no additional registration was needed according to spiking activity after the manual registration; Threshold [10, 11]. Clusters were separated into single units and MUA. Clusters of waveforms were classified as MUA if there was a mixture of distinct waveforms (examined in Phy) as well as a complicated (and abnormal) autocorrelogram. For all clusters, we measured the spike duration, peak-trough ratio, and amplitude measures (**Fig. 4**; code adapted from [24]; https://github.com/jiaxx/waveform_classification).

9. Statistical Analysis

All statistical comparisons were performed using non-parametric measures, so we did not test for normality. We tested comparisons with the Kruskal–Wallis test for non-equivalence of multiple medians followed by the use of the *post hoc* Tukey-Kramer method to determine statistically separable groups. We used the Wilcoxon rank-sum test (two-sided) for comparisons between individual medians. We tested if values were significantly different from zero using the Wilcoxon signed rank test. We corrected by adjusting the target p-value (0.05) with a Bonferroni correction for the number of comparisons being done.

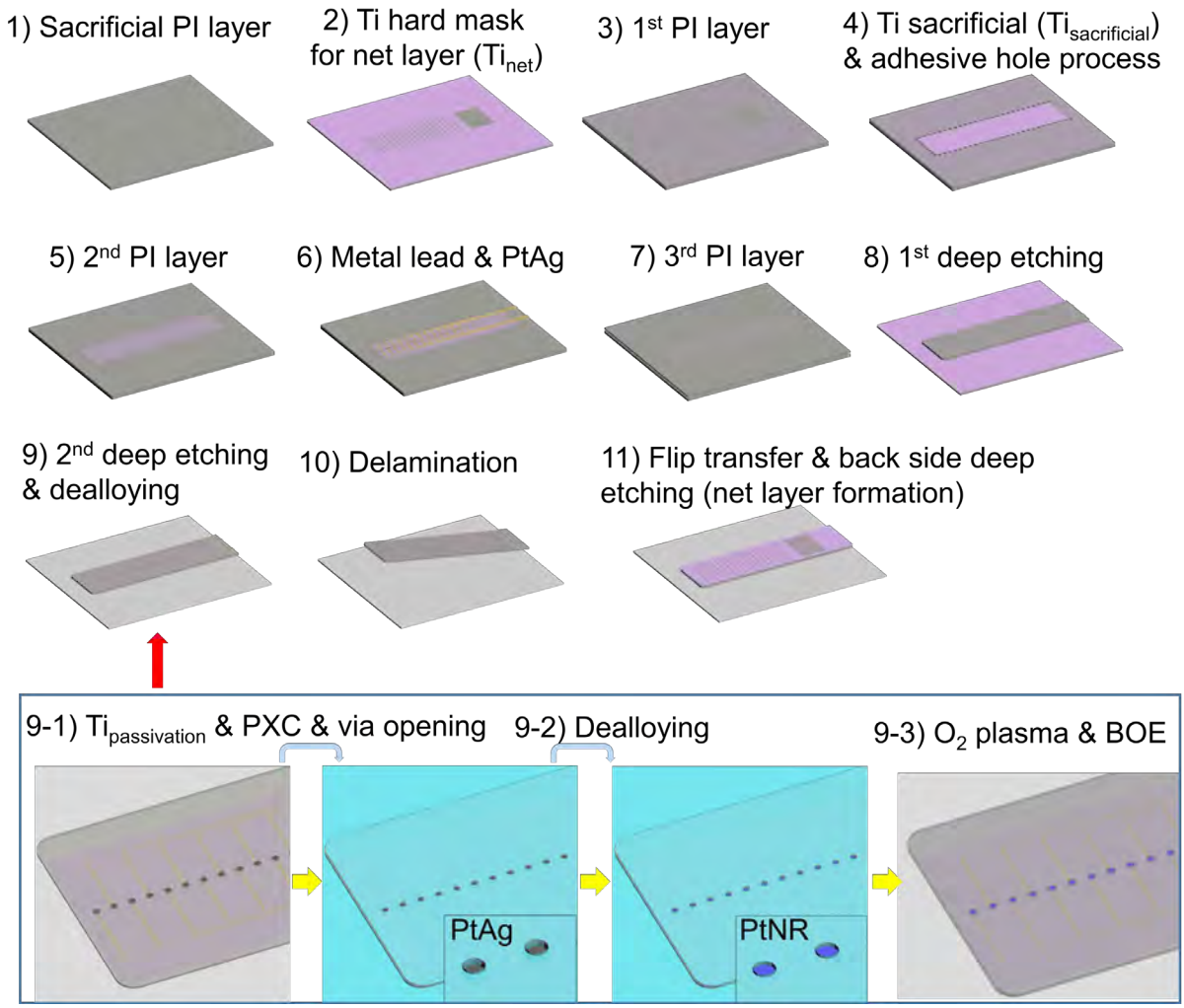

Supplementary Fig. 1. Fabrication process of μSEEG electrode.

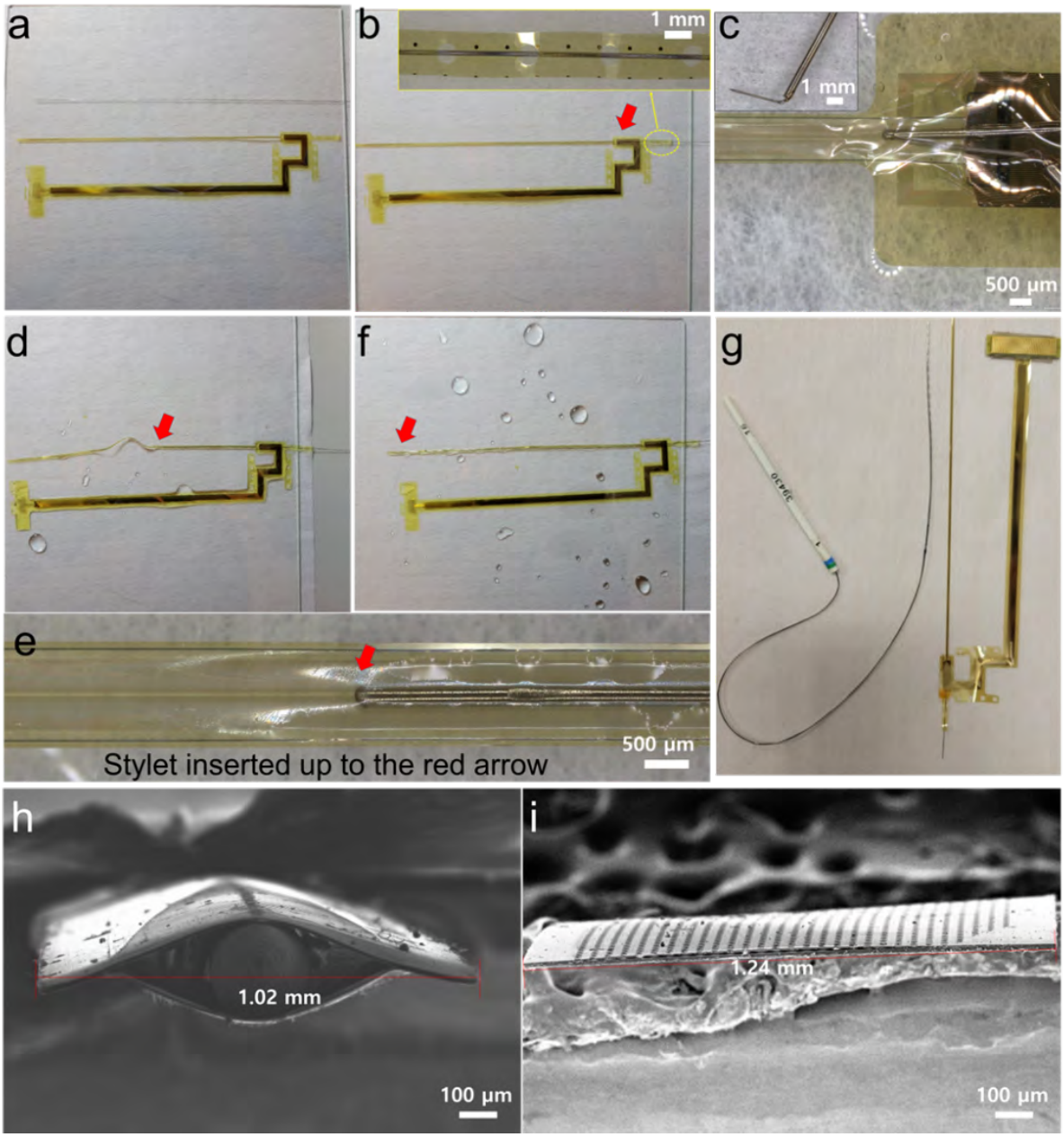

Supplementary Fig. 2. **Stylet insertion into the µSEEG electrode**. (**a**) Before insertion. (**b**) Stylet aligned to the sheath. Inset shows stitch holes with the stylet interweaved. (**c**) Zoom-in image of the sheath and the stylet inserted with support from tungsten probe for opening the sheath. (**d**) During insertion. (**e**) Zoomed-in image of the µSEEG during stylet insertion. (**f**) Stylet insertion all the way to the tip. (**g**) Scale comparison with conventional SEEG. Cross-sectional SEM image of the (**h**) µSEEG and (**i**) µSEEG after stylet retraction. The tip of the µSEEG electrode was deliberately opened by a razor blade to observe cross-sectional details of the µSEEG electrode with bio-materials remained on. In (i), the µSEEG deflated after stylet retraction. The dotted surface corresponds to the net layer on the back of the µSEEG.

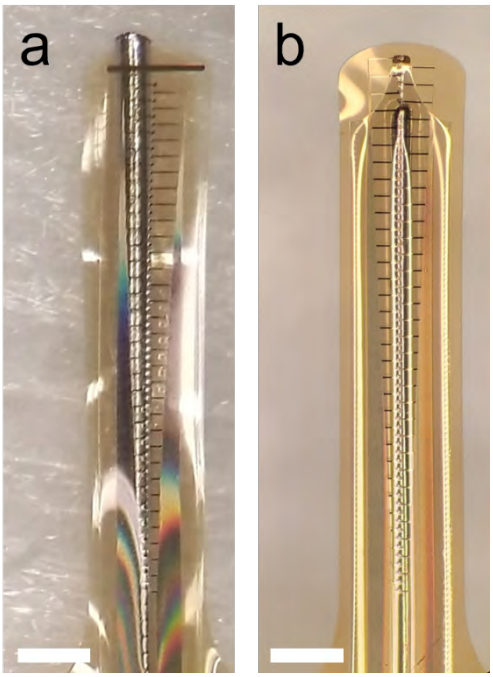

Supplementary Fig. 3. OM image of μSEEG electrode tip after stylet insertion. (a) Without interlocking hole arrays and (b) with interlocking hole arrays. Without interlocking hole arrays, the PI layers were separated and the stylet pierced the tip. Scale bars are 500 μm.

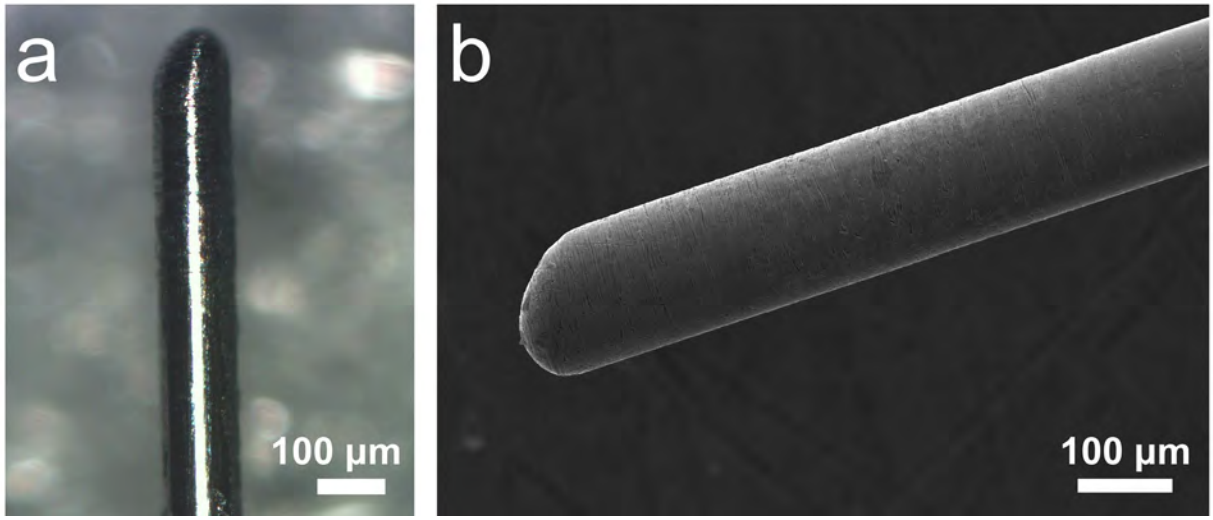

Supplementary Fig. 4. **Medical grade stainless-steel stylet tip.** (**A**) OM image and (**B**) SEM image of a polished stainless-steel stylet.

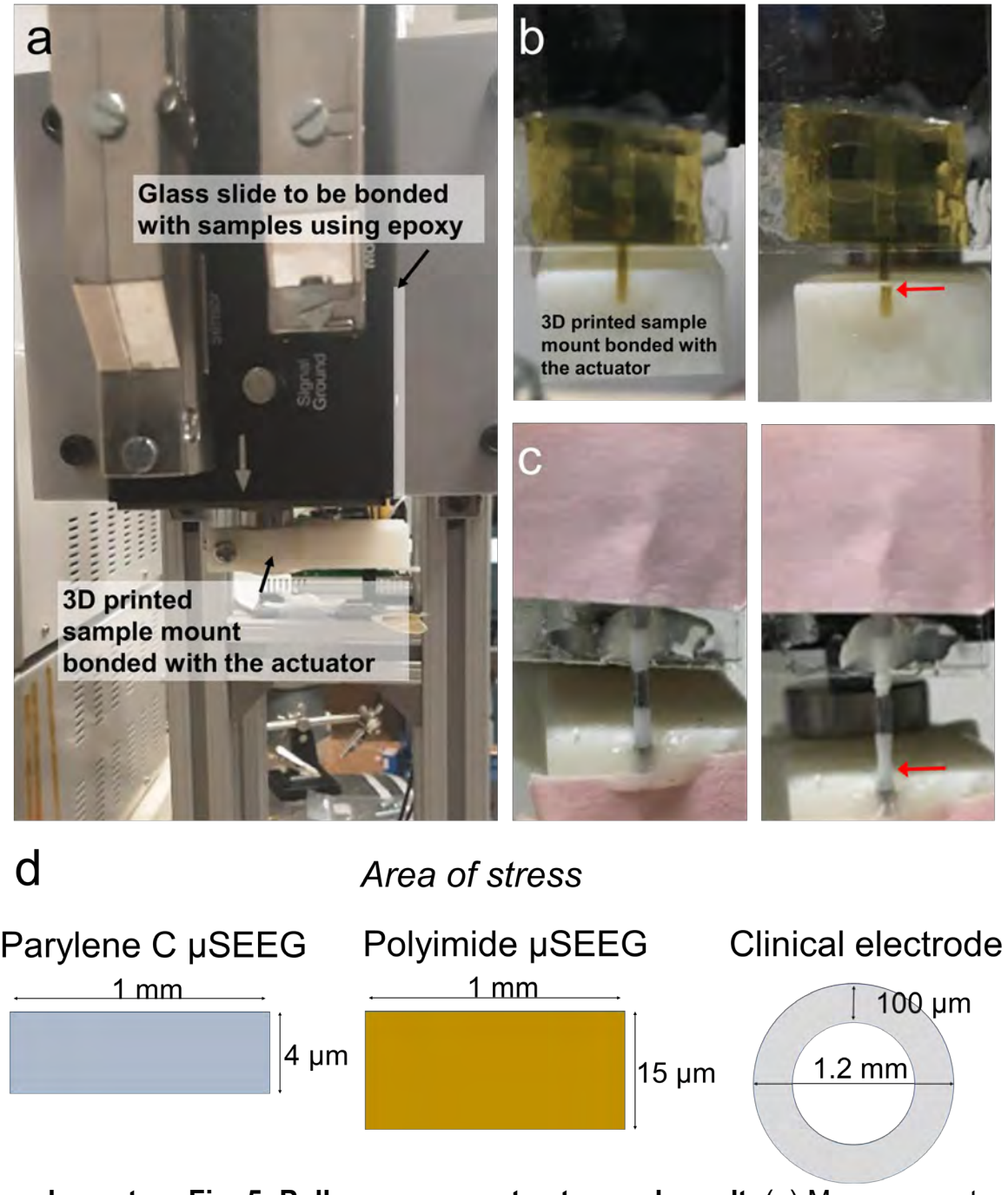

Supplementary Fig. 5. Pull measurement setup and result. (**a**) Measurement setup. (**b**) Our µSEEG and (**c**) 1.2 mm diameter PMT depth electrode integrated on the measurement setup. (**d**) illustrations of area of stress (cross-sectional illustrations of the tested electrodes)

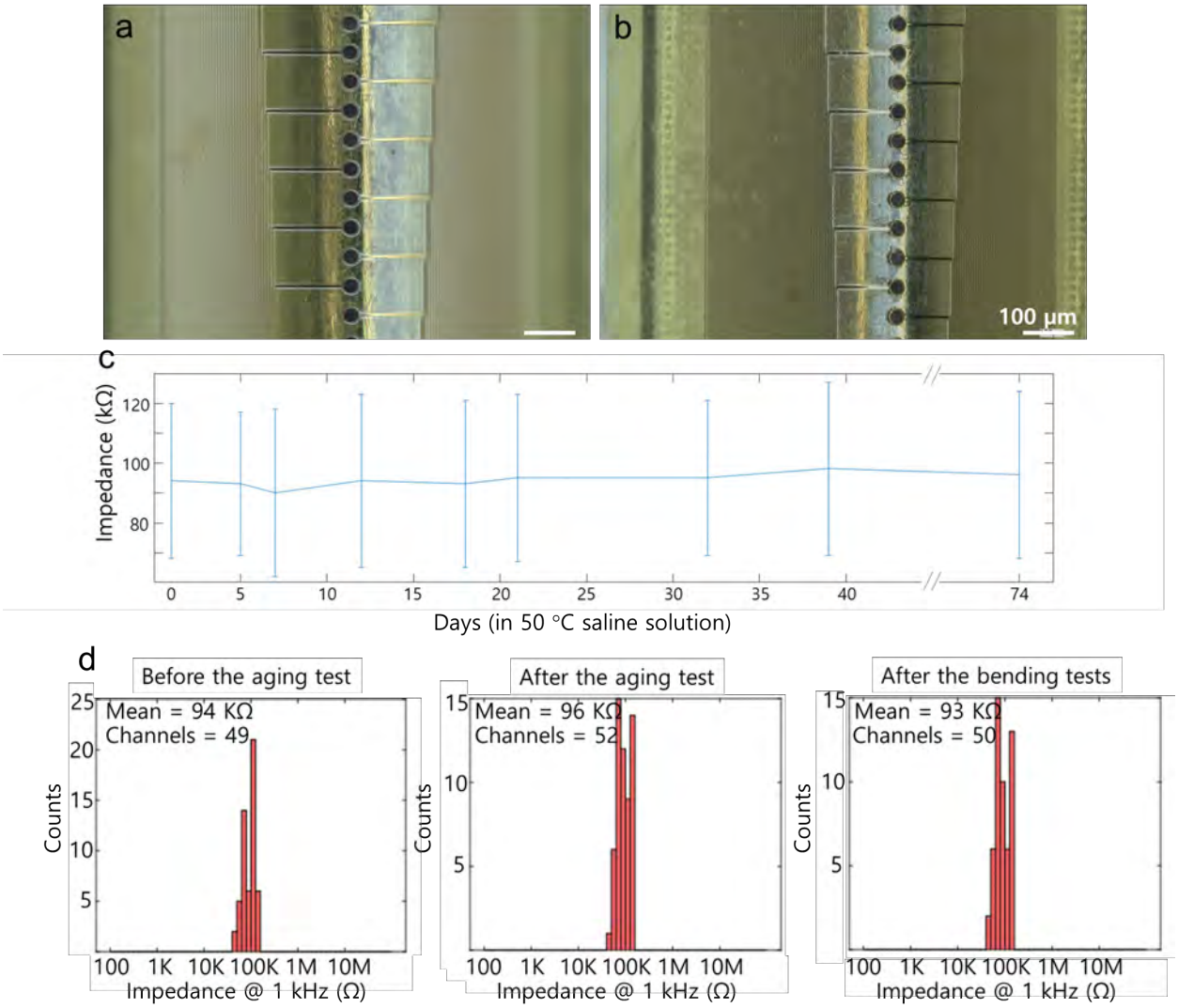

Supplementary Fig. 6. Reliability of our µSEEG for long term implantation. OM images of our µSEEG (**a**) before and (**b**) after the accelerated aging test. (**c**) Impedance of our µSEEG at 1 kHz during the accelerated aging test. (**d**) Impedance histogram of our µSEEG before, after the aging test, and after the bending tests.

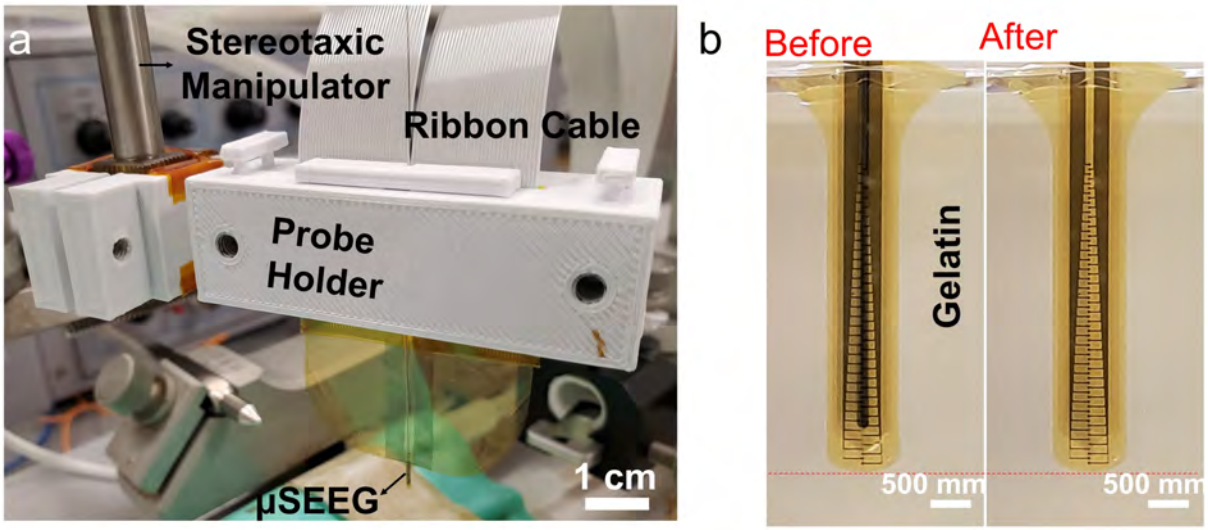

Supplementary Fig. 7. Acute insertion into a phantom brain model. (**a**) An optical image of the 3D printed holder and the μSEEG electrode attached to the stereotaxic manipulator. Scale bar is 1 cm. (**b**) An optical image of the μSEEG electrode tip inserted in the gelatin model, before and after stylet extraction. Scale bar is 500 μm.

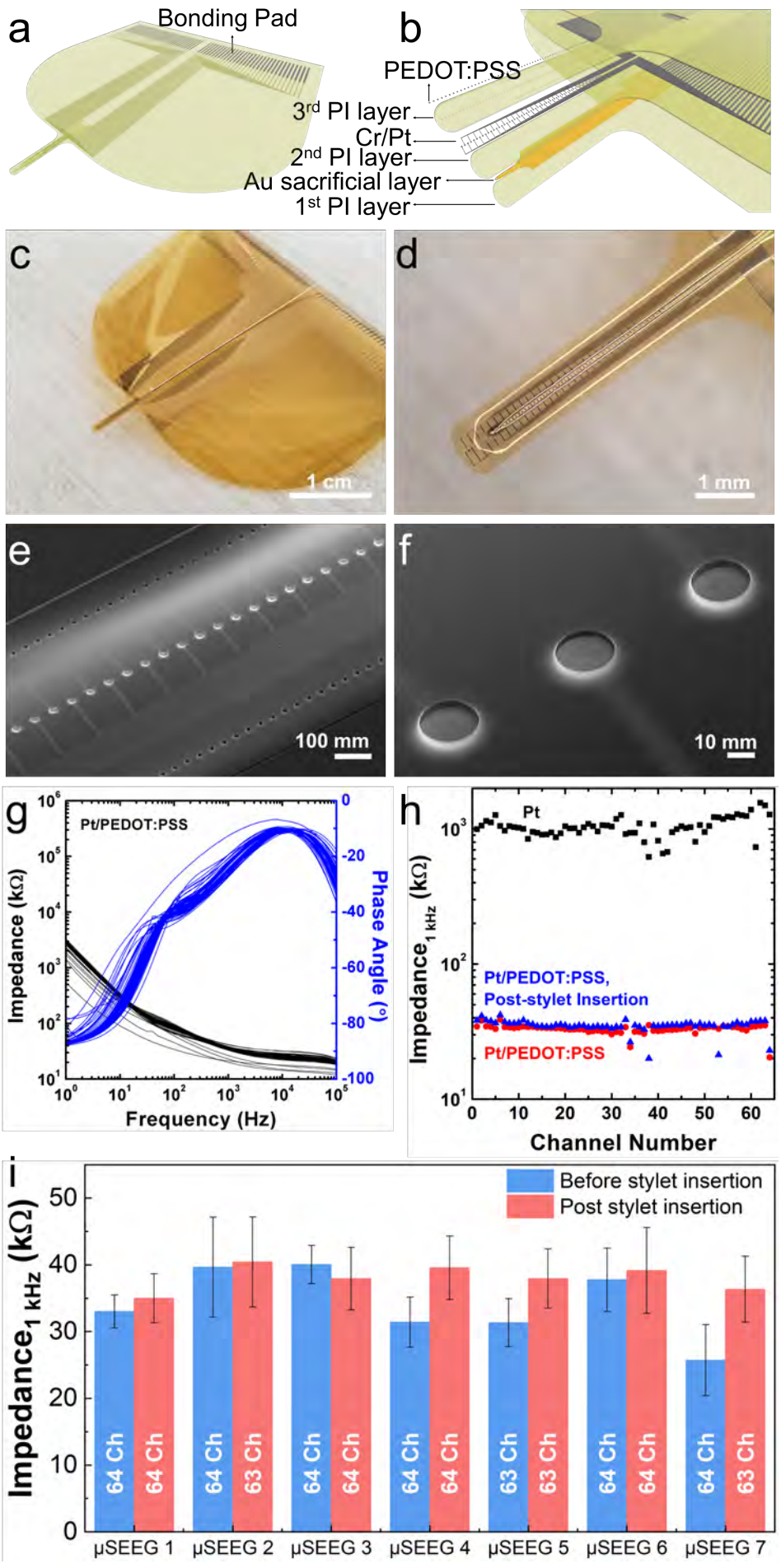
a
Bonding Pad
b
PEDOT:PSS
3rd PI layer
Cr/Pt
2nd PI layer
Au sacrificial layer
1st PI layer
c
1 cm
d
1 mm
e
100 mm
f
10 mm
g
Pt/PEDOT:PSS
Impedance (kΩ)
Phase Angle (°)
Frequency (Hz)
h
Pt
Pt/PEDOT:PSS,
Post-stylet Insertion
Pt/PEDOT:PSS
Impedance1 kHz (kΩ)
Channel Number
i
Before stylet insertion
Post stylet insertion
Impedance1 kHz (kΩ)
64 Ch
63 Ch
μSEEG 1
μSEEG 2
μSEEG 3
μSEEG 4
μSEEG 5
μSEEG 6
μSEEG 7

Supplementary Fig. 8. Manufacture and validation of the short PEDOT:PSS μSEEG in polyimide (PI). (**a**) A schematic illustration of a prototype 64 channel μSEEG electrode layout. (**b**) Exploded view of the layout at the electrode sites region. (**c**), (**d**) Optical images of the μSEEG electrode after stylet insertion. (**e**), (**f**) SEM image of μSEEG electrode showing PEDOT:PSS on Cr/Pt after stylet insertion. (**g**) Electrochemical impedance spectra of Pt/PEDOT:PSS recording electrodes. (**h**) Electrochemical impedance magnitude at 1 kHz of each channel before and after stylet insertion and comparison with Pt. (**i**) averaged impedance magnitude at 1 kHz for 7 PEDOT:PSS μSEEG electrodes, before and after stylet insertion.

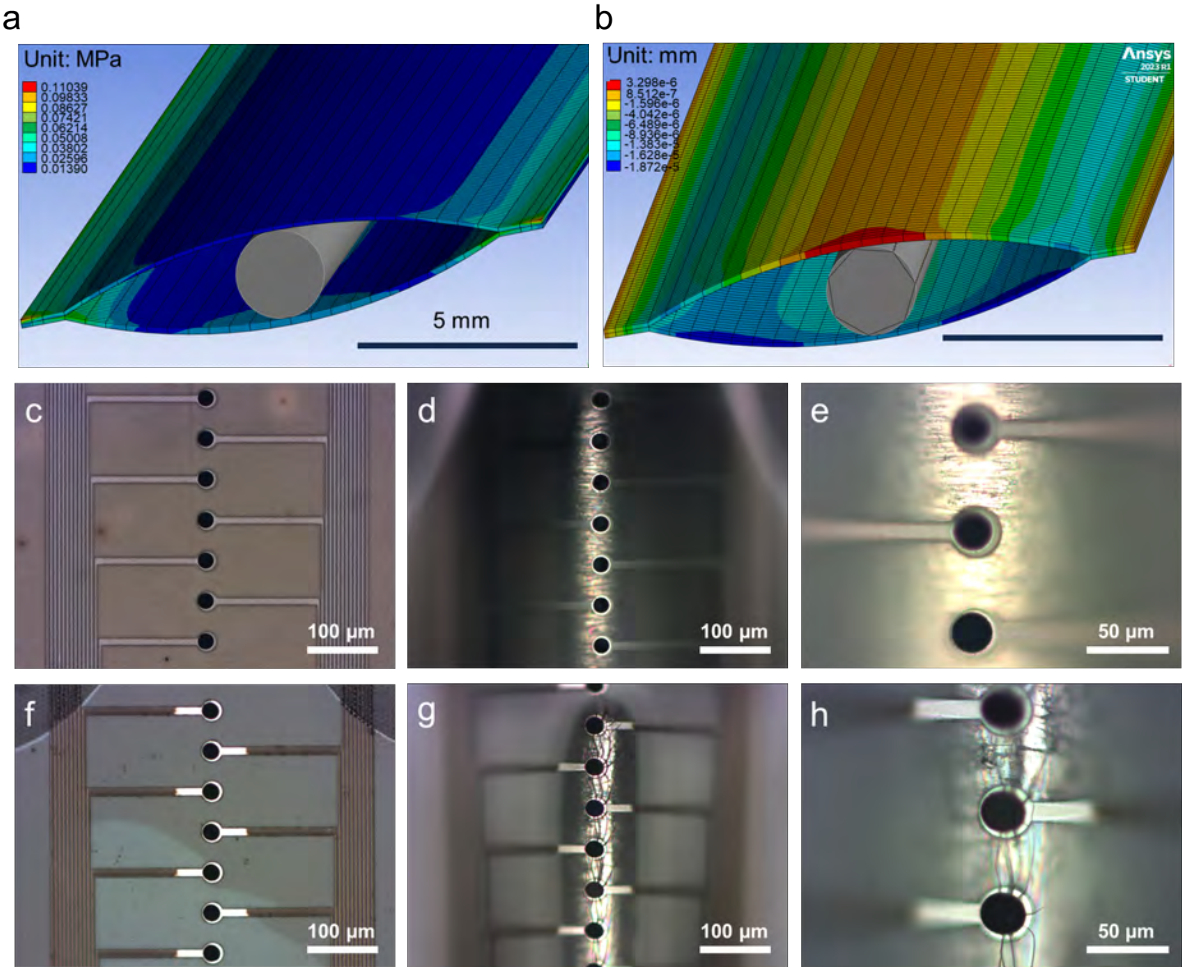

Supplementary Fig. 9. FEM analysis results showing (**a**) external strength and (**b**) deformation introduced by stylet insertion. OM images of the PEDOT:PSS/polyimide (**c** – **e**) and (**f** – **h**) PEDOT:PSS/parylene C electrodes before and after stylet insertion.

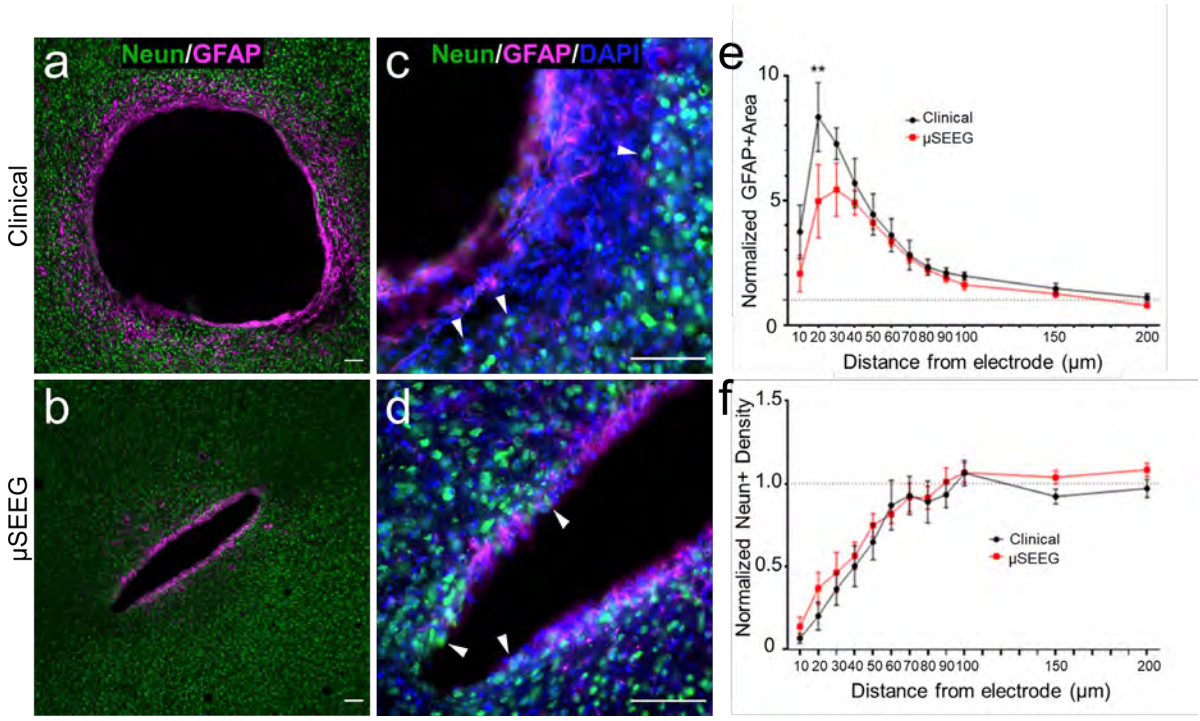

Supplementary Fig. 10. GFAP and NeuN reactivity folloing two weeks of electrode implantation. Wide-field view of horizontal cortical section following (**a**) clinical or (**b**) μSEEG electrode implantation. NeuN is pseudocolored green, GFAP magenta, and DAPI blue. (**c**) and (**d**) are magnifications of the boxed areas in (**a**) and (**b**) to show NeuN reactivity adjacent to electrode placement. Represnetative NeuN-positive cells are indicated by arrows. (**e**) Average GFAP area, normalized to each animal (2-way ANOVA, $F(1,72) = 8.749$, $P=0.0042$; N=4/electrode, 1-4 sections per animal). (f) Normalized NeuN+ density (2-way ANOVA, $F(1, 72) = 3.290$, $P=0.0739$, N=4/electrode, 1-4 sections per animal). Data are plotted as mean ± SEM, **** $P < 0.0001$, ** $P < 0.01$ by 2-way ANOVA followed by Sidak's multiple comparisons test. Scale bar is 100 μm.

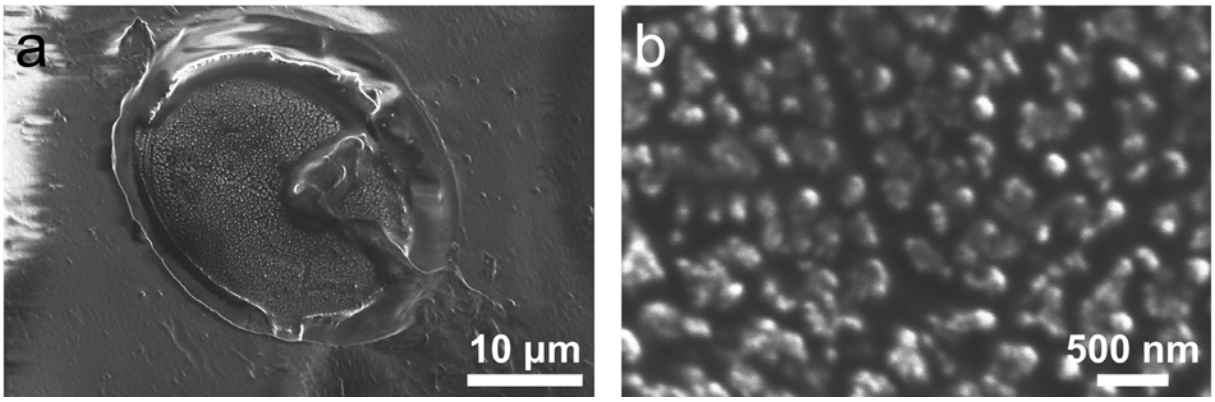

Supplementary Fig. 11. SEM images of µSEEG electrodes upon extraction. (**a**) Low magnification image showing whole single PtNRs contact and biological tissue and (**b**) High magnification image of PtNRs contact.

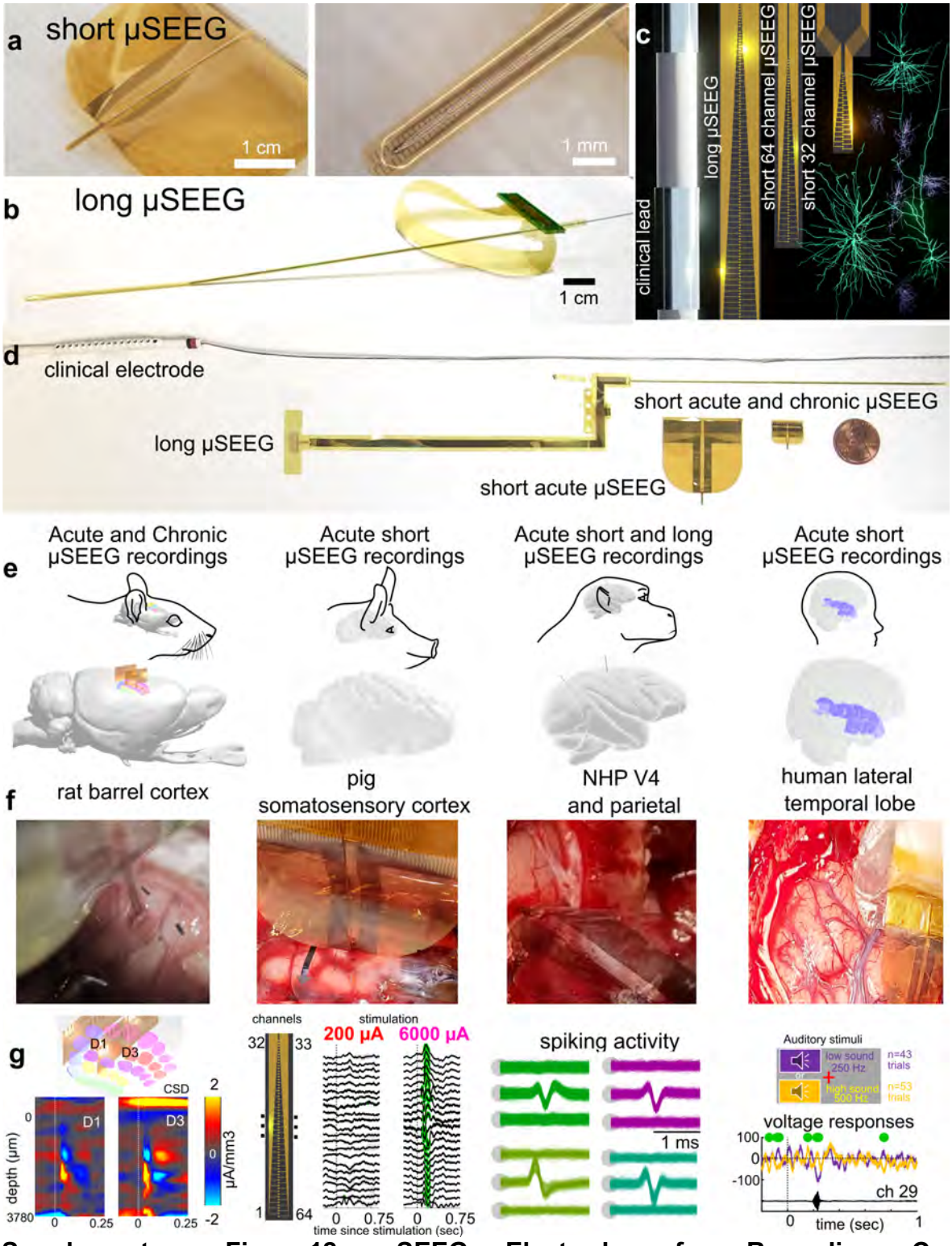

Supplementary Fig. 12. µSEEG Electrodes for Recording Cortical Neurophysiological Activity in Multiple Species. (**a**). The short µSEEG with 64 microelectrode contacts at 60 µm contact to contact spatial resolution. (**b**) The long µSEEG with 128 microelectrode contacts at 60 µm contact to contact spatial resolution. (**c-d**) Diagram and photo of the relative scale of human cortical neurons relative to a clinical SEEG lead and a short µSEEG electrode [25-27]. (**e**) Different species and brains

along with the locations of the electrodes for neural recordings in this study. (**f-g**) Images of the different preparations inserted into cortex with example neurophysiological recordings below the images.

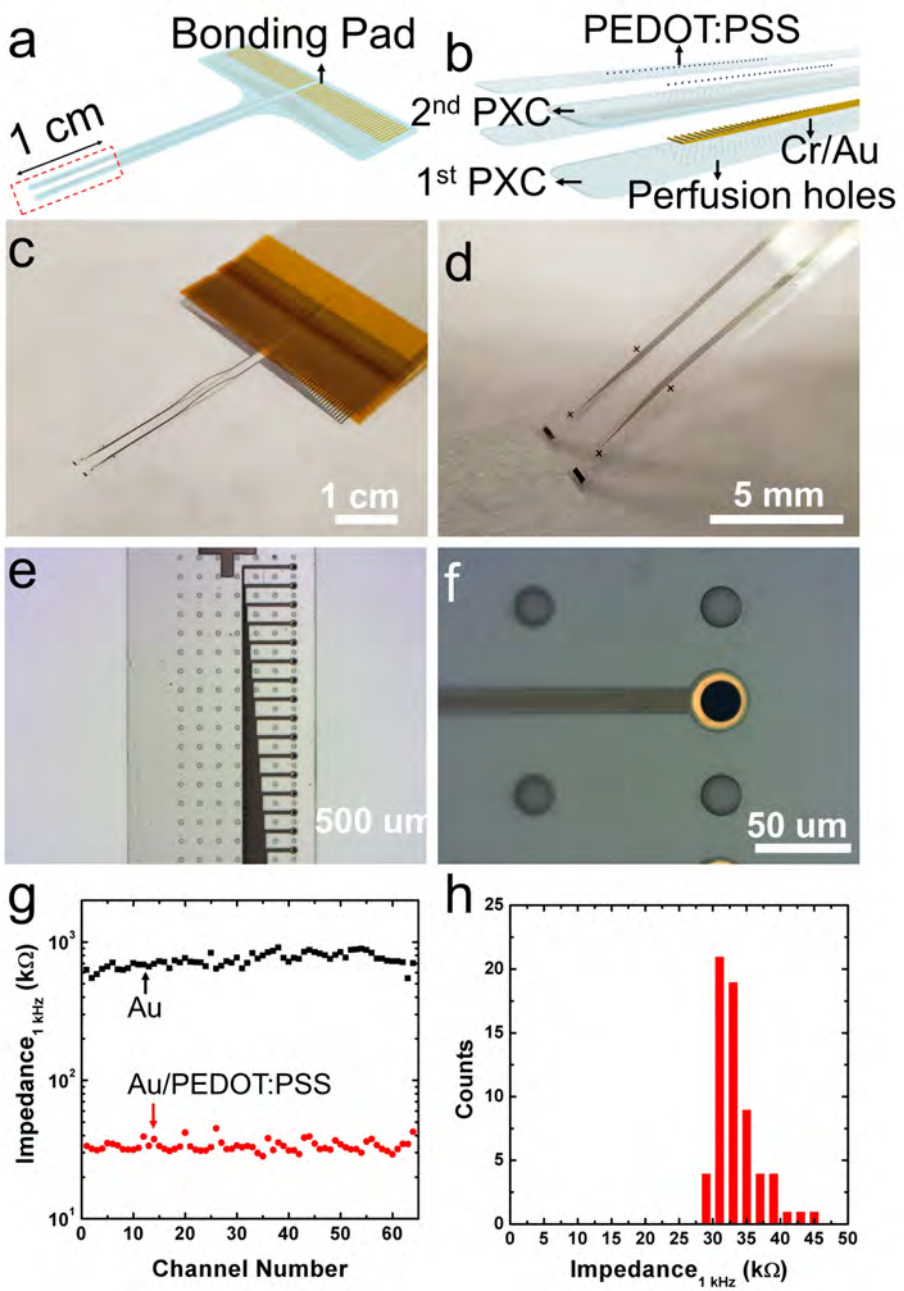

Supplementary Fig. 13. Manufacture and characterization of the μECoG for comparing surface to depth electrode capabilities. (**a**) A schematic illustration of μECoG electrode layout. Red dotted square indicates electrode sites region. (**b**) Exploded view of the layout at the electrode sites region. (**c**), (**d**) Optical images of the μECoG electrode. Scale bar is (**c**) 1 cm and (**d**) 5 mm. (**e**) Top-view optical microscopic image of the electrode sites region. (**f**) Magnified top-view optical microscopic image showing PEDOT:PSS on Cr/Au electrode sites and perforation holes. (**g**) Electrochemical impedance magnitude at 1 kHz of each channel of μECoG electrode before and after PEDOT:PSS electrodeposition. (**h**) Electrochemical impedance magnitude at 1 kHz histogram of Au/PEDOT:PSS.

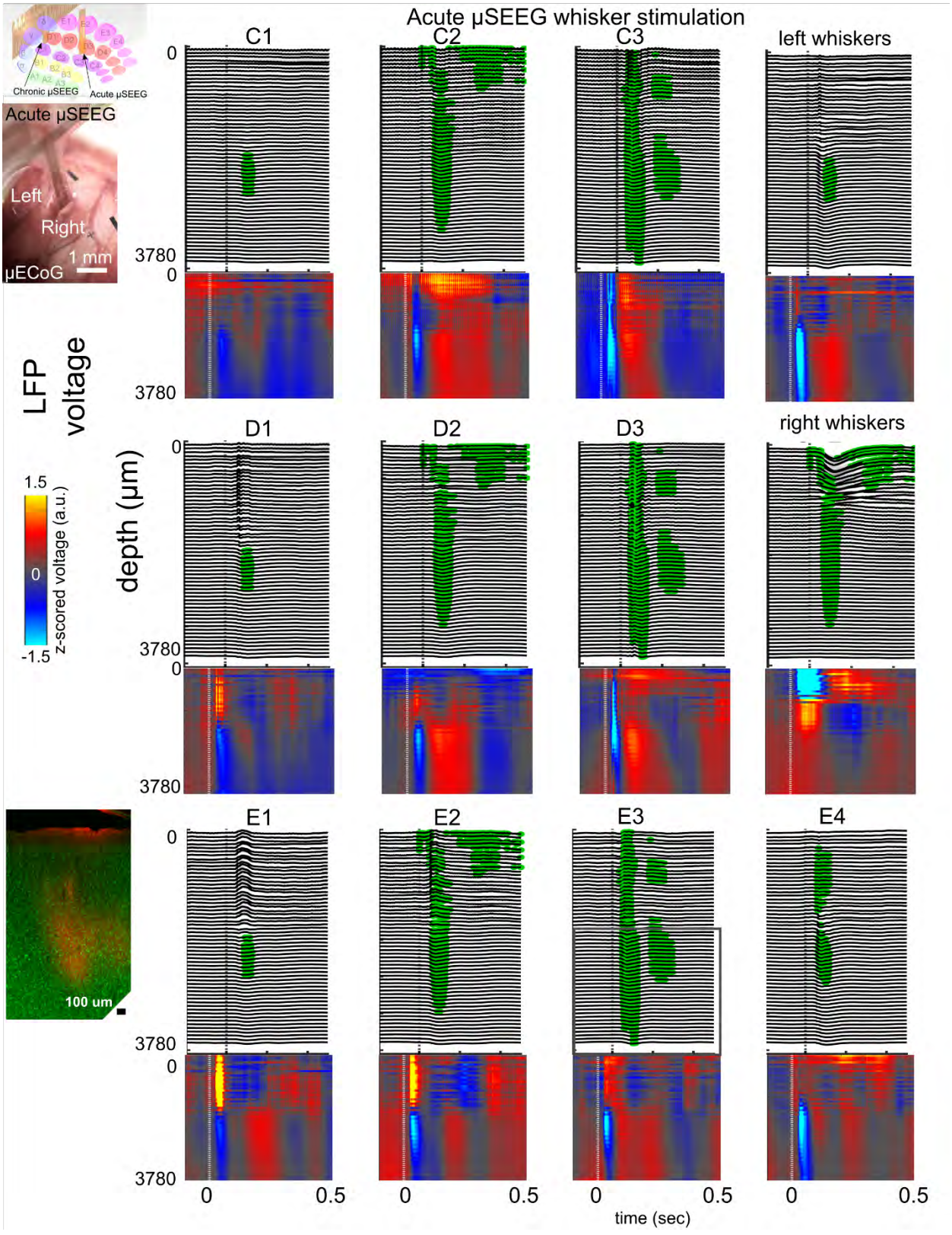
Acute µSEEG whisker stimulation
Chronic µSEEG
Acute µSEEG
Acute µSEEG
Left
Right
1 mm
µECoG
LFP voltage
1.5
0
-1.5
z-scored voltage (a.u.)
depth (µm)
C1
C2
C3
left whiskers
D1
D2
D3
right whiskers
E1
E2
E3
E4
0
3780
100 um
0
0.5
time (sec)

Supplementary Fig. 14. Acute laminar voltage recordings in the rat barrel cortex with the μSEEG with sensory stimulation. Upper left: Location and 3D reconstruction of possible locations of the acute and chronic implantation of μSEEG electrodes for recording from the rat barrel cortex and images of the implanted μECoG electrode (left) and the μSEEG electrode (right). First, the μECoG electrode was placed on the cortical surface. At the gap between two columns of the μECoG electrode, the μSEEG electrode was implanted, and the stylet was removed using the previously described technique. Note some contacts are outside brain tissue on the μSEEG electrode. Voltage responses across the μSEEG electrode to whisker stimulation at different whisker locations for the voltages (local field potential or LFP). Green dots indicate significantly different from 0.5 sec before (which is baseline) air puff stimulation to the whisker (Wilcoxon rank-sum test) per channel and across trials. Number of trials >10.

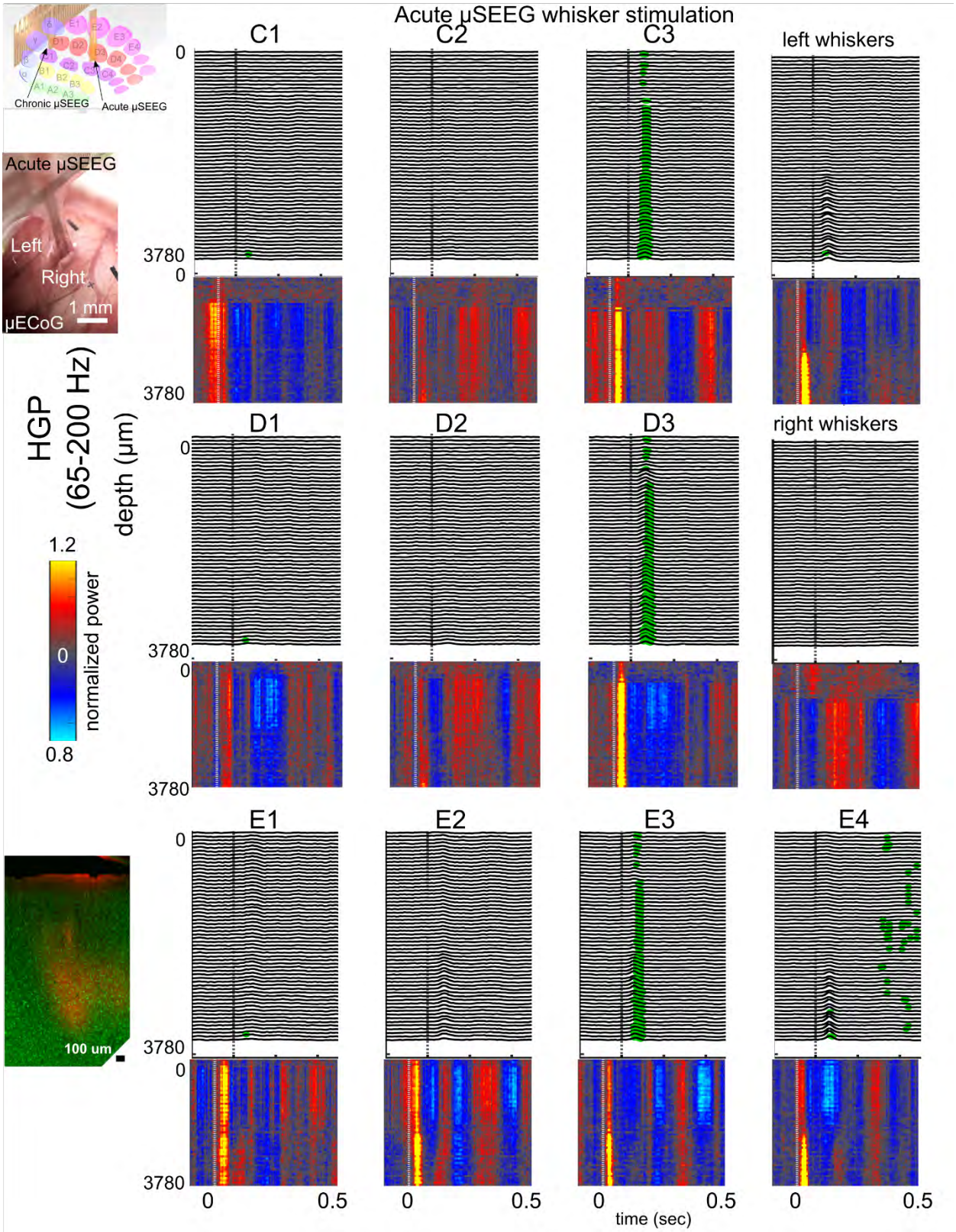

Supplementary Fig. 15. Acute laminar high gamma power recording in the rat barrel cortex with the µSEEG with sensory stimulation. Upper left: Location and 3D reconstruction of possible locations of the acute and chronic implantation of µSEEG electrodes for recording from the rat barrel cortex and images of the implanted µECoG

electrode (left) and the μSEEG electrode (right). First, the μECoG electrode was placed on the cortical surface. At the gap between two columns of the μECoG electrode, the μSEEG electrode was implanted, and the stylet was removed using the previously described technique. Note some contacts are outside brain tissue on the μSEEG electrode. Responses across the μSEEG electrode to whisker stimulation at different whisker locations for the high gamma power (HGP). Green dots indicate significantly different from 0.5 sec before (which is baseline) air puff stimulation to the whisker (Wilcoxon rank-sum test) per channel and across trials. Number of trials >10.

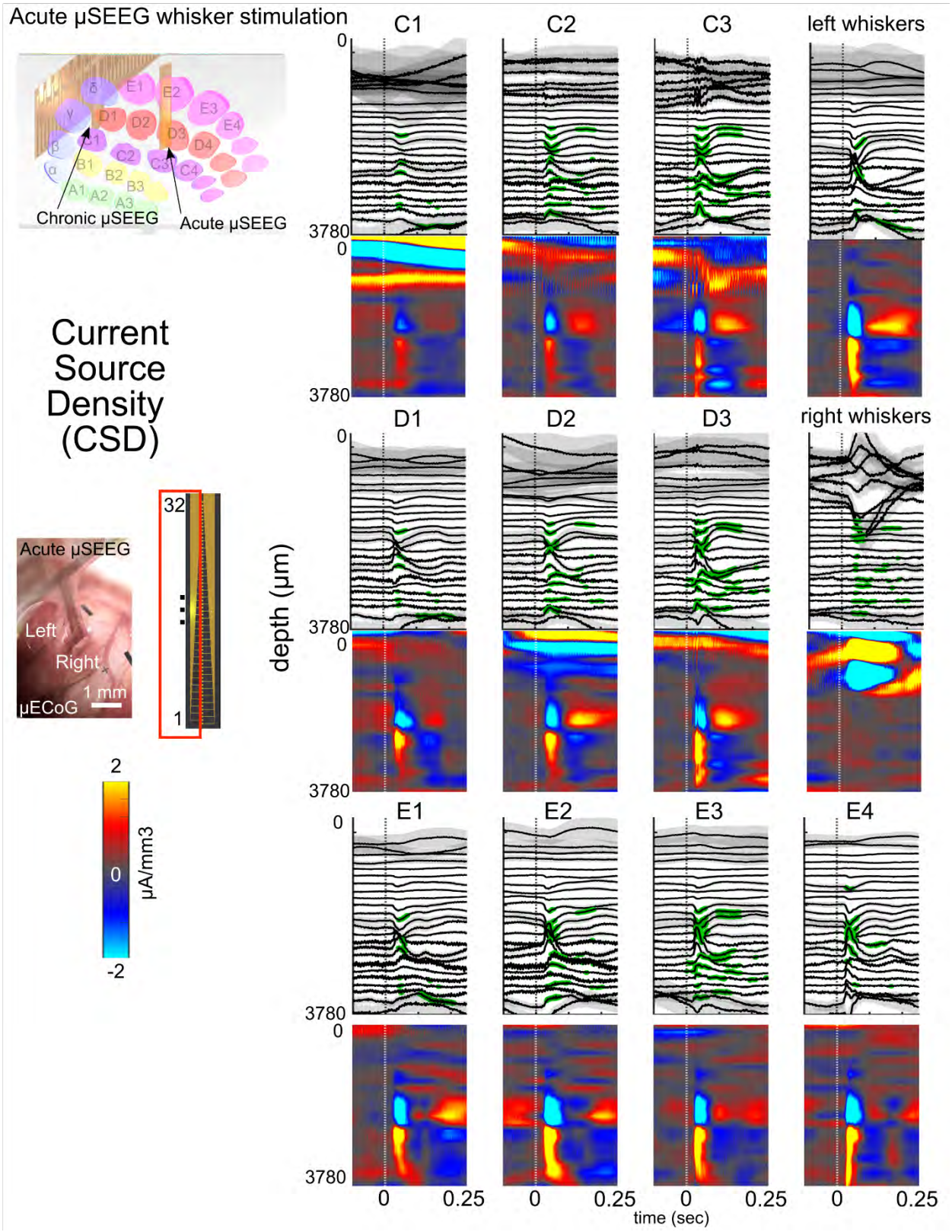

Supplementary Fig. 16. Acute laminar recording of current source density (CSD) for the leftmost channels in the rat barrel cortex with the µSEEG with sensory stimulation. Upper left: Location and 3D reconstruction of possible locations of the acute

and chronic implantation of μSEEG electrodes d for recording from the rat barrel cortex and images of the implanted surface μECoG electrode and the μSEEG electrode. Note some contacts are outside brain tissue on the μSEEG electrode. Current source density (CSD) responses across half the μSEEG electrode (left side) to whisker stimulation at different whisker locations. Green dots indicate significantly different from 0.5 sec before (which is baseline) air puff stimulation to the whisker (Wilcoxon rank-sum test) per channel and across trials. Number of trials >10.

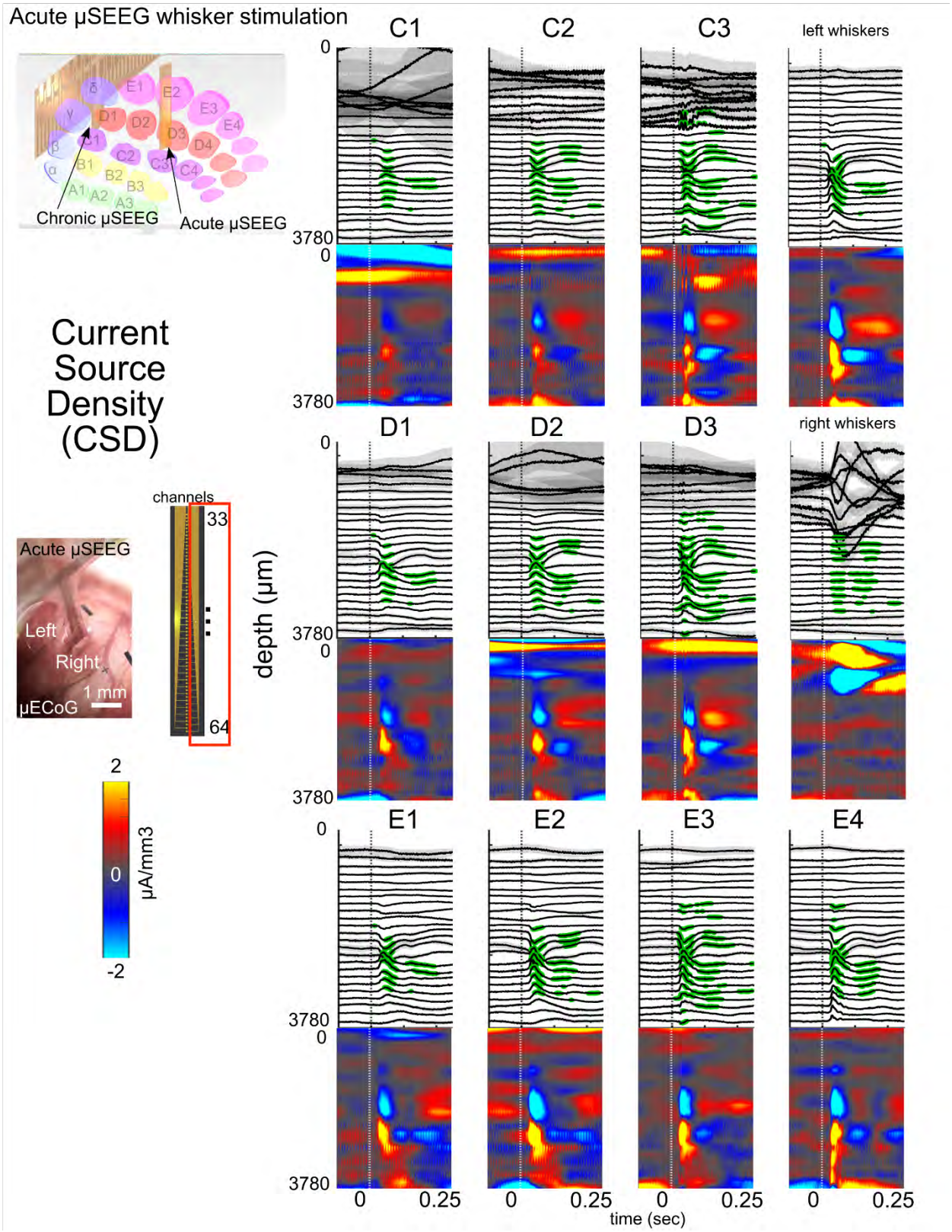

Supplementary Fig. 17. Acute laminar recording of current source density (CSD) for the rightmost channels in the rat barrel cortex with the μSEEG with sensory stimulation. Upper left: Location and 3D reconstruction of possible locations of the acute and chronic implantation of μSEEG electrodes d for recording from the rat barrel cortex

and images of the implanted surface µECoG electrode and the µSEEG electrode. Note some contacts are outside brain tissue on the µSEEG electrode. Current source density (CSD) responses across half the µSEEG electrode (righ side) to whisker stimulation at different whisker locations. Green dots indicate significantly different from 0.5 sec before (which is baseline) air puff stimulation to the whisker (Wilcoxon rank-sum test) per channel and across trials. Number of trials >10.

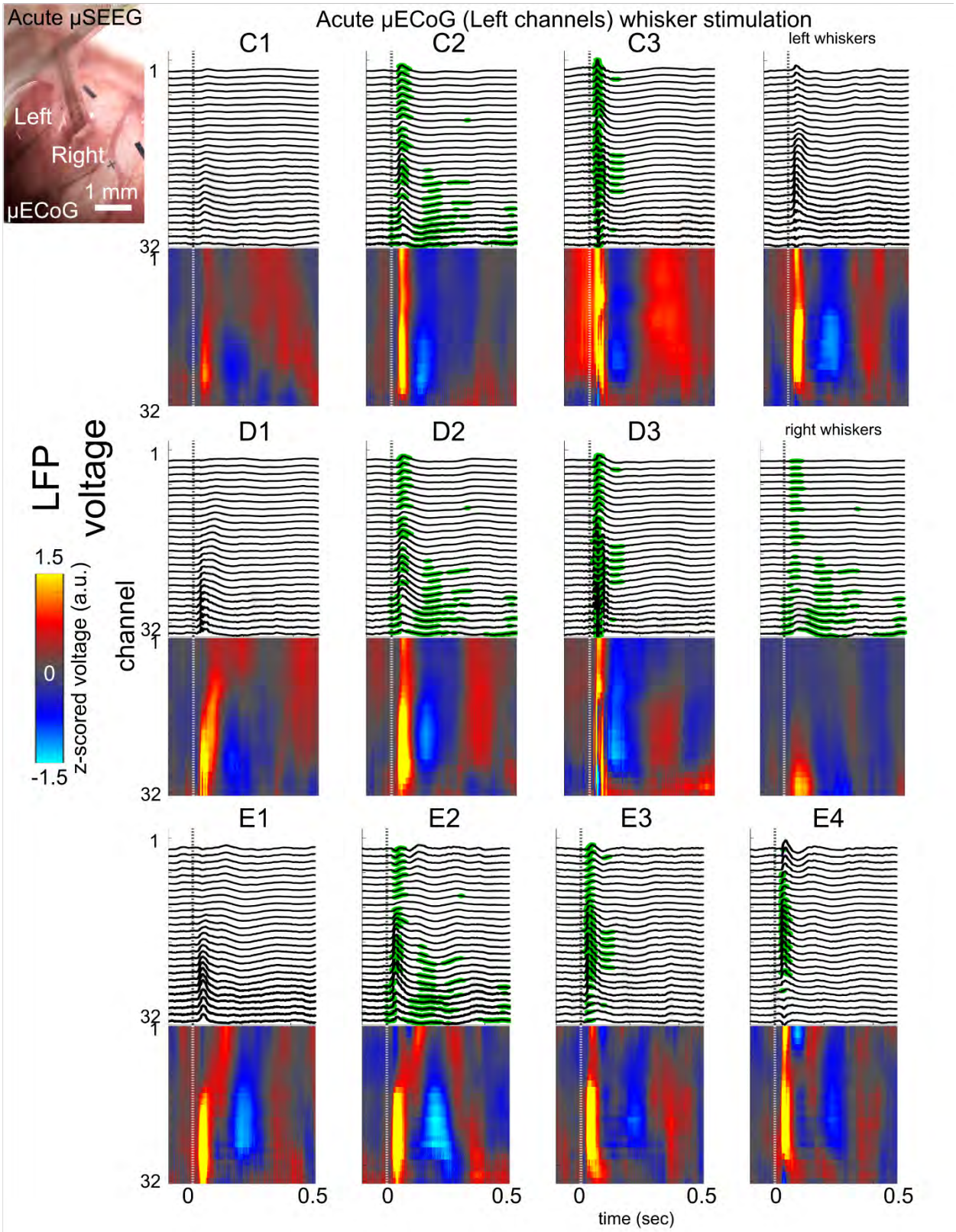

Supplementary Fig. 18. Acute surface local field potential (LFP) voltage recording with a strip of the μECoG over the rat barrel cortex with sensory stimulation. Upper left: Location and 3D reconstruction of possible locations of the acute and chronic implantation of μSEEG electrodes for recording from the rat barrel cortex and images of

the implanted μECoG electrode (left) and the μSEEG electrode (right). Note some contacts are outside brain tissue on the μSEEG electrode. Voltage responses across the left ribbon of the μECoG electrode to whisker stimulation at different whisker locations for the voltages and multi-unit activity (MUA). Green dots indicate significantly different from 0.5 sec before (which is baseline) air puff stimulation to the whisker (Wilcoxon rank-sum test) per channel and across trials. Number of trials >10.

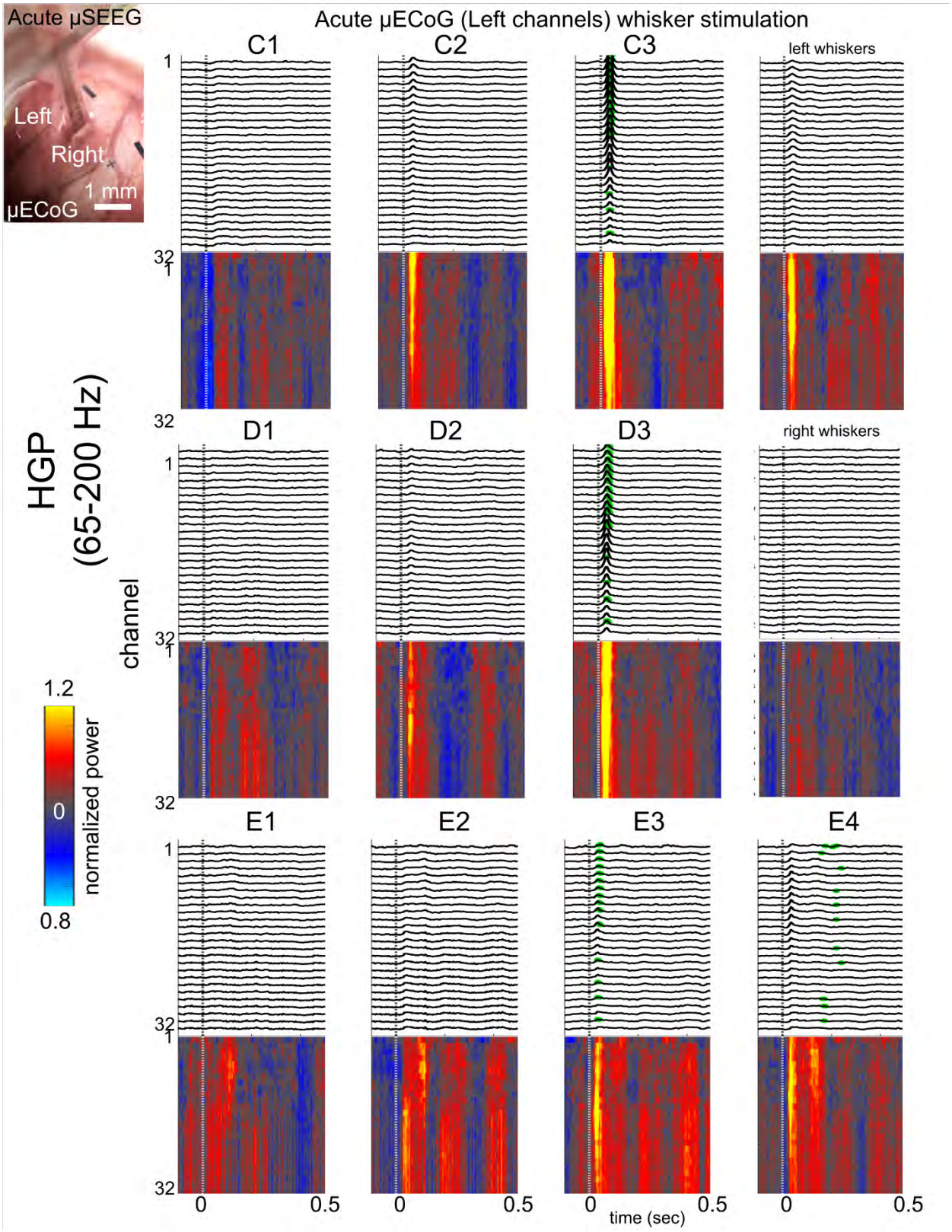

Supplementary Fig. 19. Acute surface high gamma power (HGP) recording with a strip of the μECoG over the rat barrel cortex with sensory stimulation. Upper left: Location and 3D reconstruction of possible locations of the acute and chronic implantation of μSEEG electrodes for recording from the rat barrel cortex and images of the implanted

μECoG electrode (left) and the μSEEG electrode (right). Note some contacts are outside brain tissue on the μSEEG electrode. Responses across the left ribbon of the μECoG electrode to whisker stimulation at different whisker locations for the high gamma power (HGP). Green dots indicate significantly different from 0.5 sec before (which is baseline) air puff stimulation to the whisker (Wilcoxon rank-sum test) per channel and across trials. Number of trials >10.

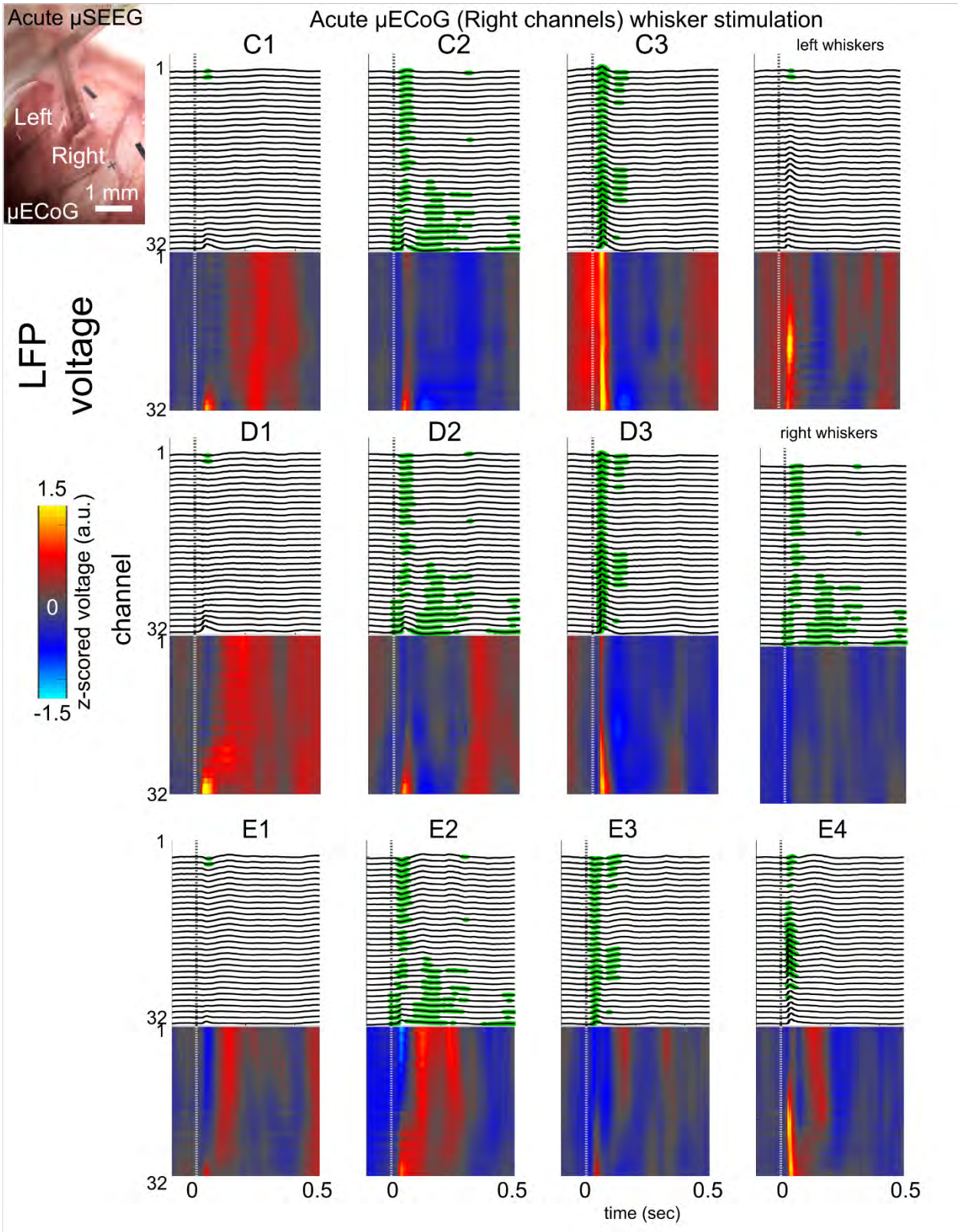

Supplementary Fig. 20. Acute surface local field potential (LFP) voltage recording with a strip of the μECoG over the rat barrel cortex with sensory stimulation. Upper left: Location and 3D reconstruction of possible locations of the acute and chronic implantation of μSEEG electrodes for recording from the rat barrel cortex and images of

the implanted μECoG electrode (left) and the μSEEG electrode (right). Note some contacts are outside brain tissue on the μSEEG electrode. Voltage responses across the right ribbon of the μECoG electrode to whisker stimulation at different whisker locations for the voltages. Green dots indicate significantly different from 0.5 sec before (which is baseline) air puff stimulation to the whisker (Wilcoxon rank-sum test) per channel and across trials. Number of trials >10.

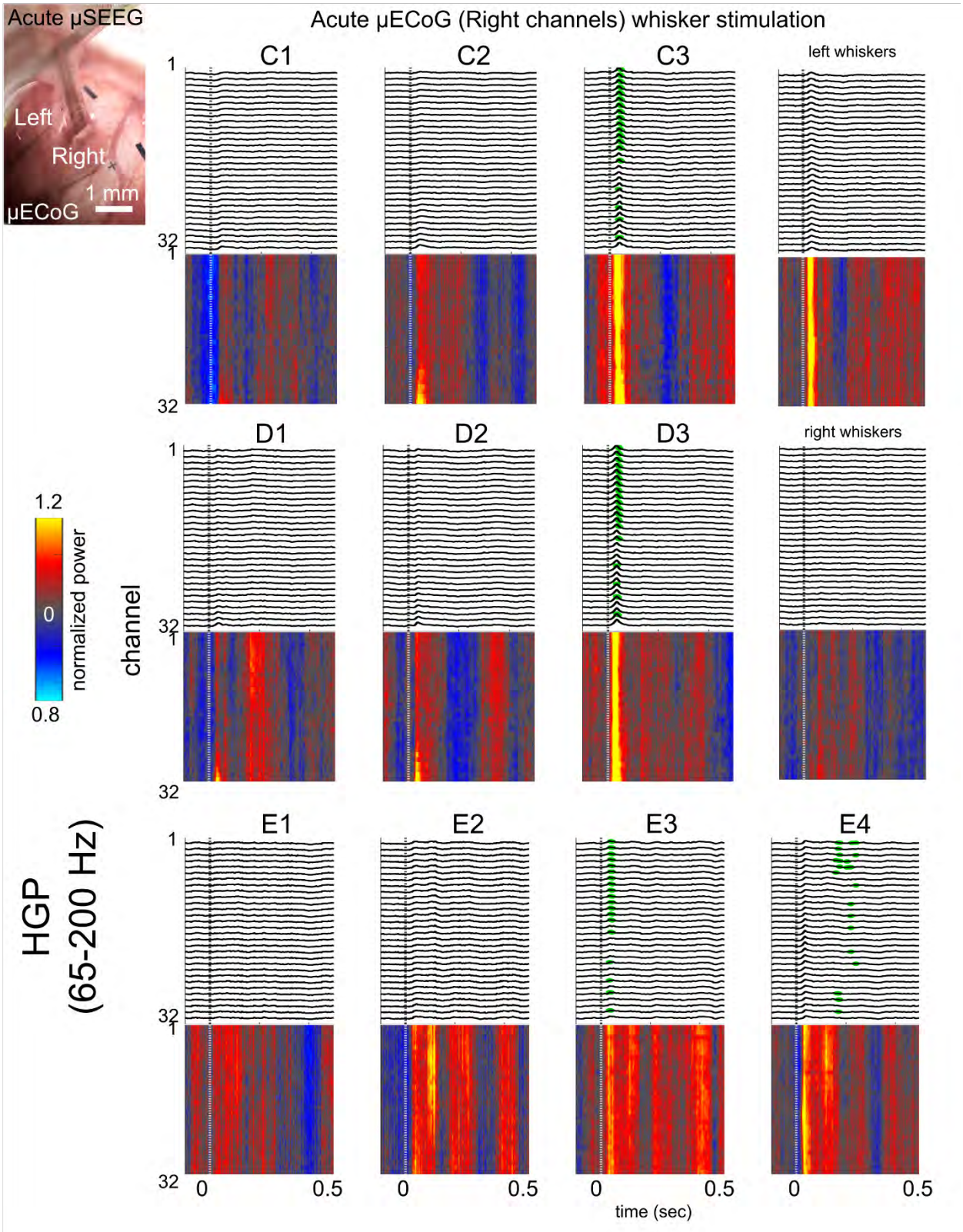

Supplementary Fig. 21. Acute surface high gamma power (HGP) recording with a strip of the μECoG over the rat barrel cortex with sensory stimulation. Upper left: Location and 3D reconstruction of possible locations of the acute and chronic implantation of μSEEG electrodes for recording from the rat barrel cortex and images of the implanted

μECoG electrode (left) and the μSEEG electrode (right). Note some contacts are outside brain tissue on the μSEEG electrode. Responses across the right ribbon of the μECoG electrode to whisker stimulation at different whisker locations for the voltages and multi-unit activity (MUA). Green dots indicate significantly different from 0.5 sec before (which is baseline) air puff stimulation to the whisker (Wilcoxon rank-sum test) per channel and across trials. Number of trials >10.

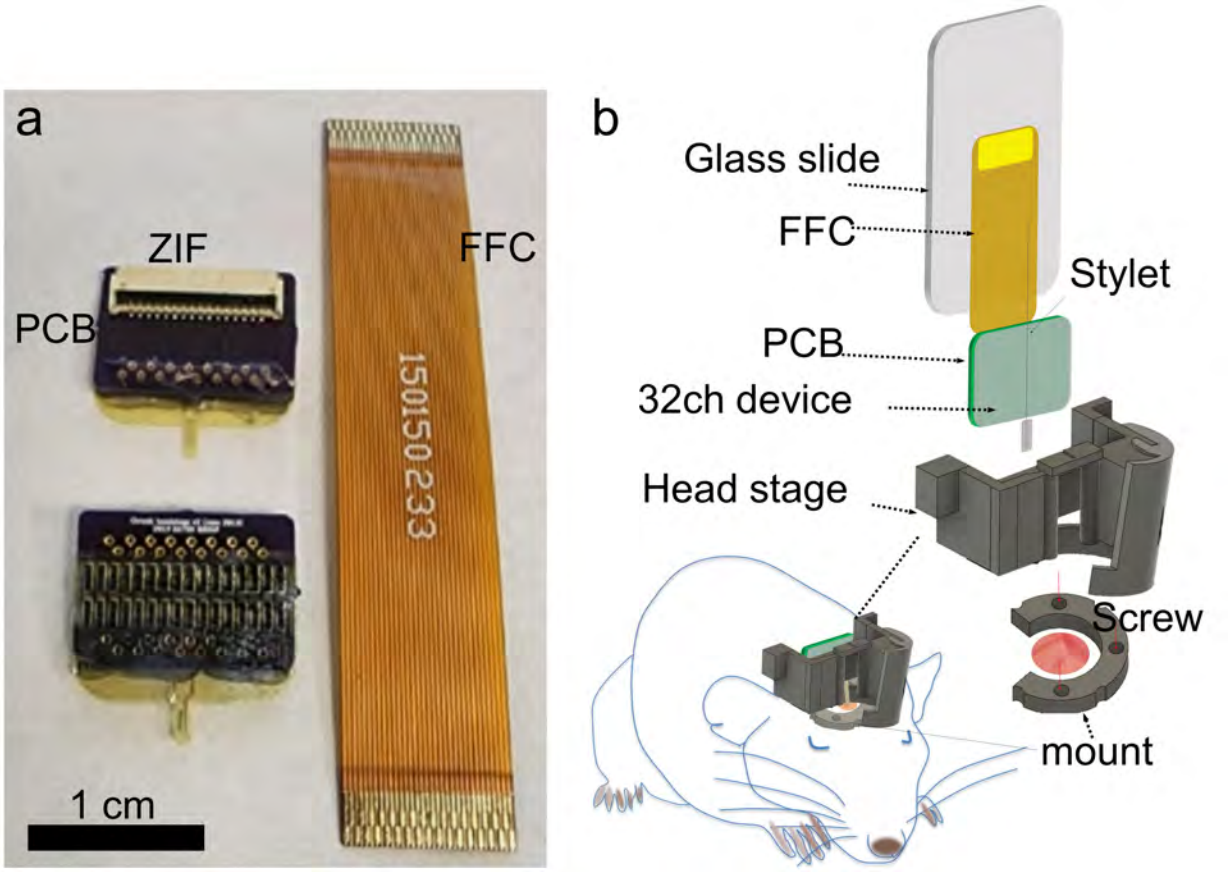

Supplementary Fig. 22. Chronic implantation of the μSEEG electrode and recordings. (**a**) Hardware components and (**b**) Illustrations of the chronic μSEEG electrode implantation procedures.

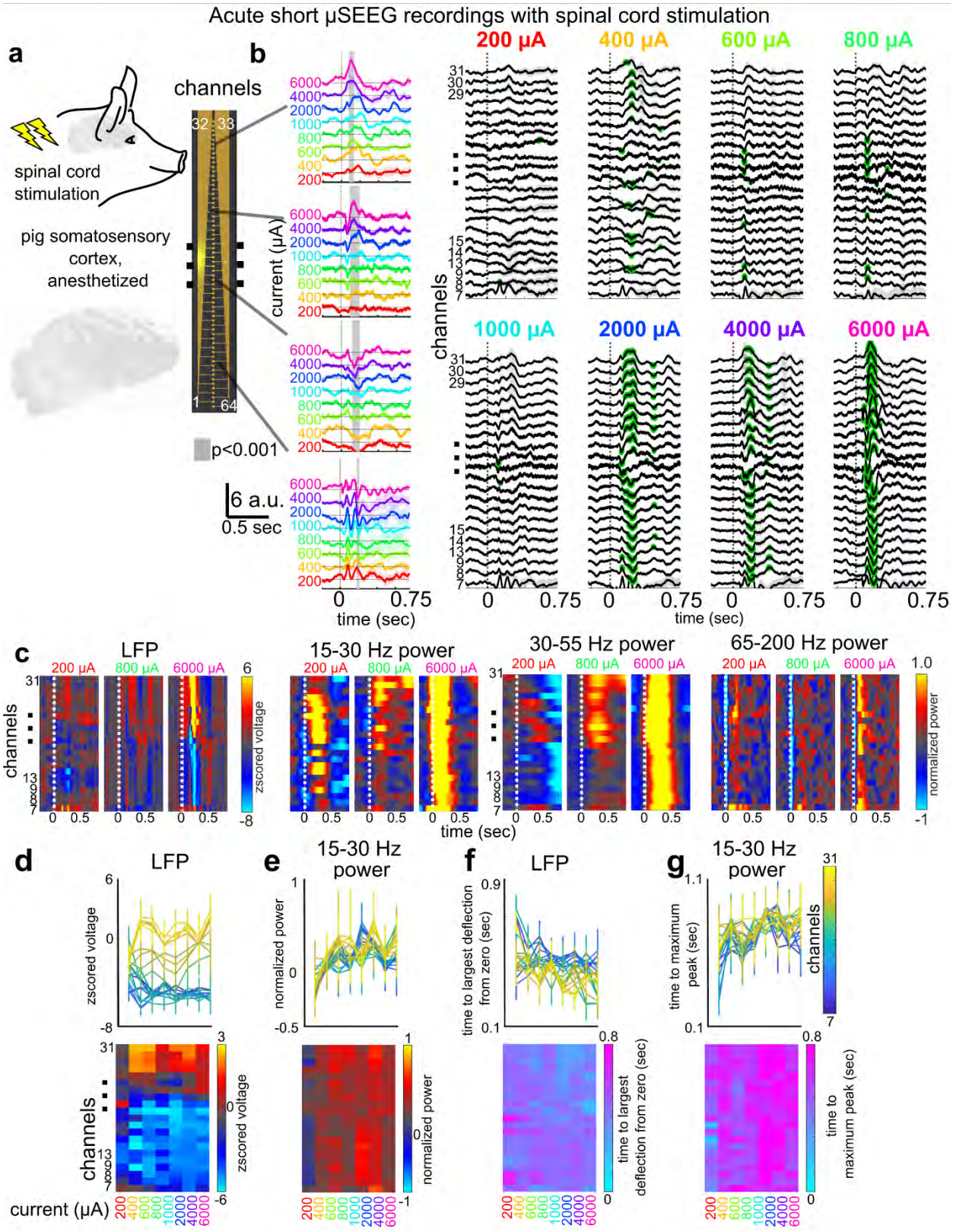

Supplementary Fig. 23. Acute short 64 channel µSEEG recordings in an anesthetized pig. (**a**) Direct electrical stimulation of the spinal cord while doing an acute short 64 channel µSEEG electrode recording from the pig cortex, with responses increasing with increasing injected current. Grey bar indicates significantly different

between current steps, Wilcoxon rank sum test. (**b**) Voltage responses along the electrode depth with more responses significantly different to baseline (0.5 sec before stimulation) occurring more with higher current levels (green dots, Wilcoxon rank sum test). (**c**) Average responses to stimulation in different frequency bands to different levels of injected current across channels. (**d**) Top: zscored voltage and Bottom: Two dimensional map of the time to zscored voltage per channel and per current step. (**e**) Top: 15-30 Hz power and Bottom: Two dimensional map of the time to 15-30 Hz power per channel and per current step. (**f**) Top: time to peak voltage and Bottom: Two dimensional map of the time to peak deflection from baseline per channel and per current step (**g**) Top: time to maximum deflection in 15-30 Hz power and Bottom: Two dimensional map of the time to maximum deflection in 15-30 Hz power per channel and per current step.

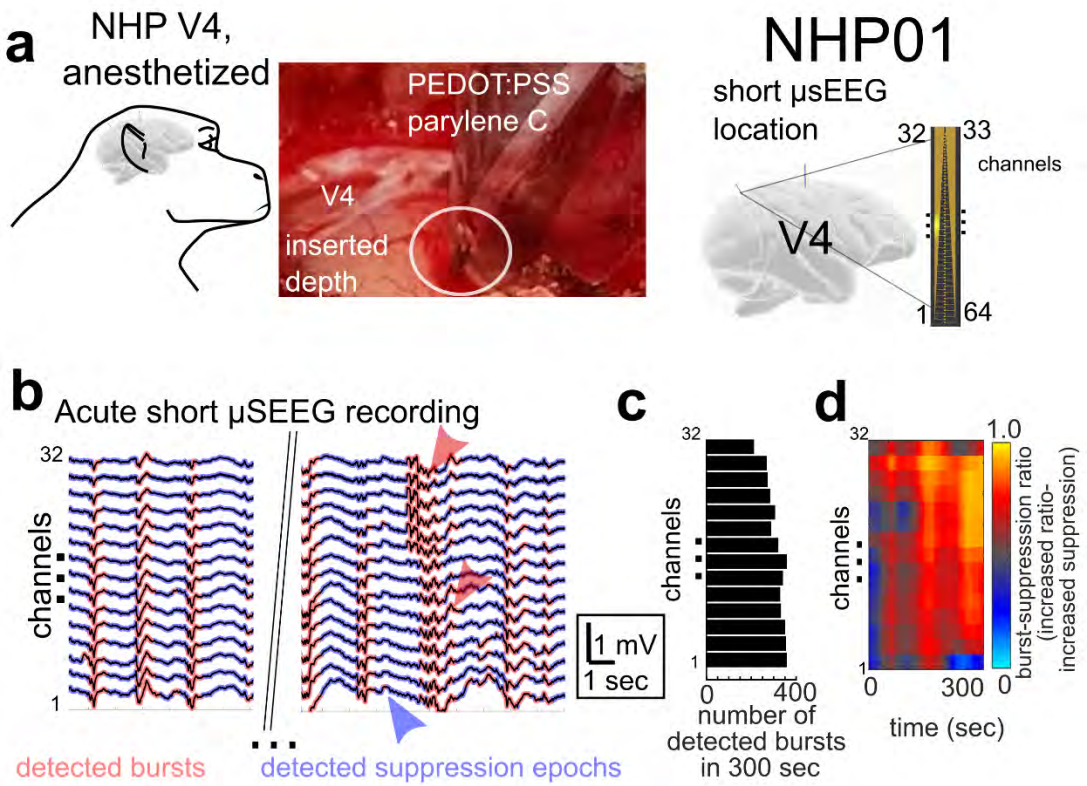

Supplementary Fig. 24. Acute short 64 channel μSEEG recordings in an anesthetized non-human primate (NHP). (**a**) Acute implant of the short μSEEG electrode into V4 in an anesthetized NHP and ongoing evidence of burst suppression detected using automated approaches per channel. Arrowheads indicate detected bursts. (**b**) Number of detected bursts in 300 seconds per channel, with a correlation between channel depth and the number of bursts r= 0.72; p=0.0021 (Pearson's linear correlation). (**c**) burst-suppression ratio changes over time during the recording across channels.

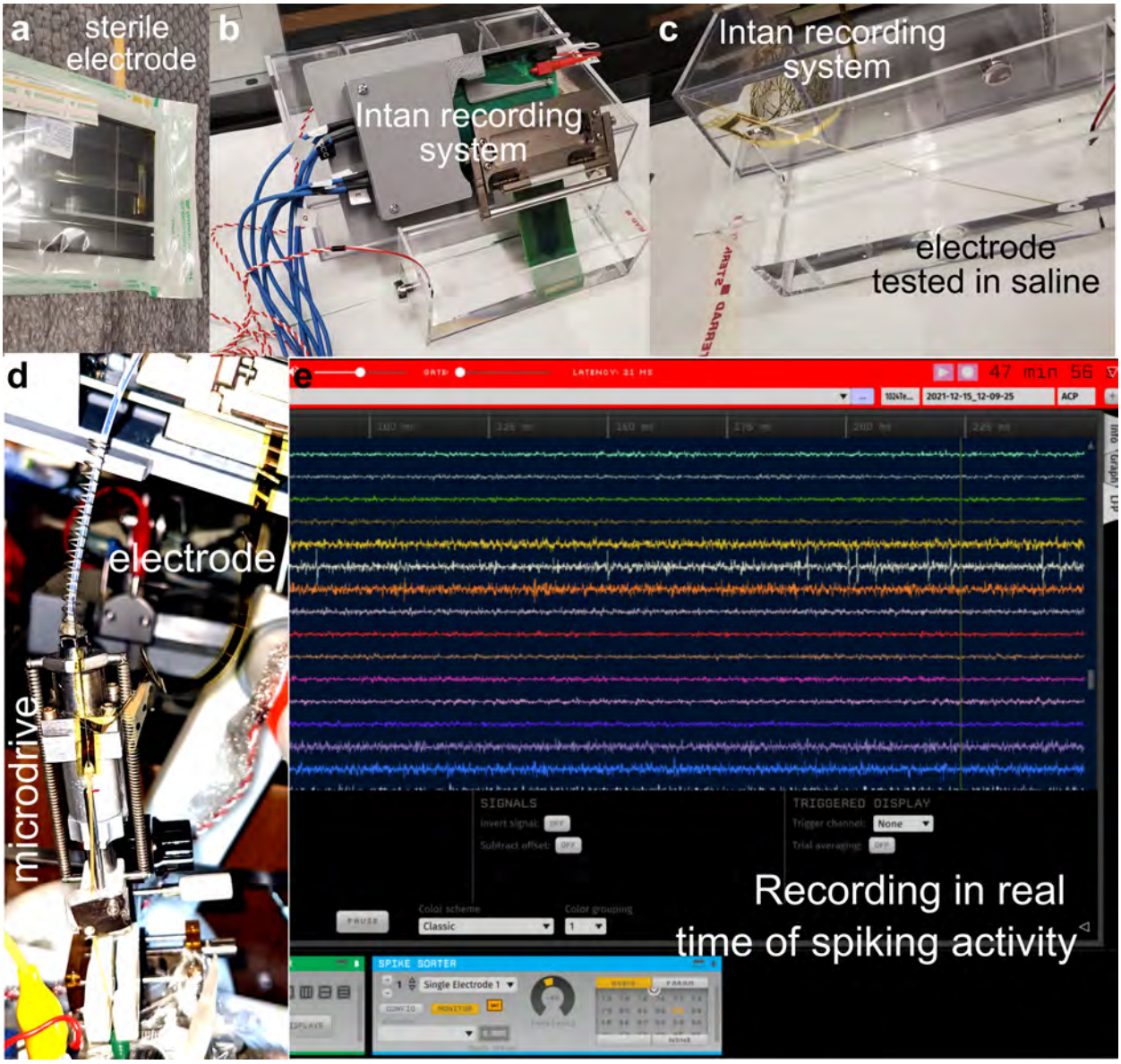

Supplementary Fig. 25. Set up and Microdrive recording using the long µSEEG electrode to record ongoing activity. (**a**) Sterile electrode used in recording, sterilized using Ethylene Oxide gas. (**b**) 1024 channel Intan system used to record activity, testing in saline. (**c**) Testing of the long µSEEG electrode in saline. (**d**) Microdrive used to deliver the microelectrode. The same microdrive was used to drive tungsten electrodes to record activity. (**e**) Recording of real-time spiking activity using the long µSEEG electrode.

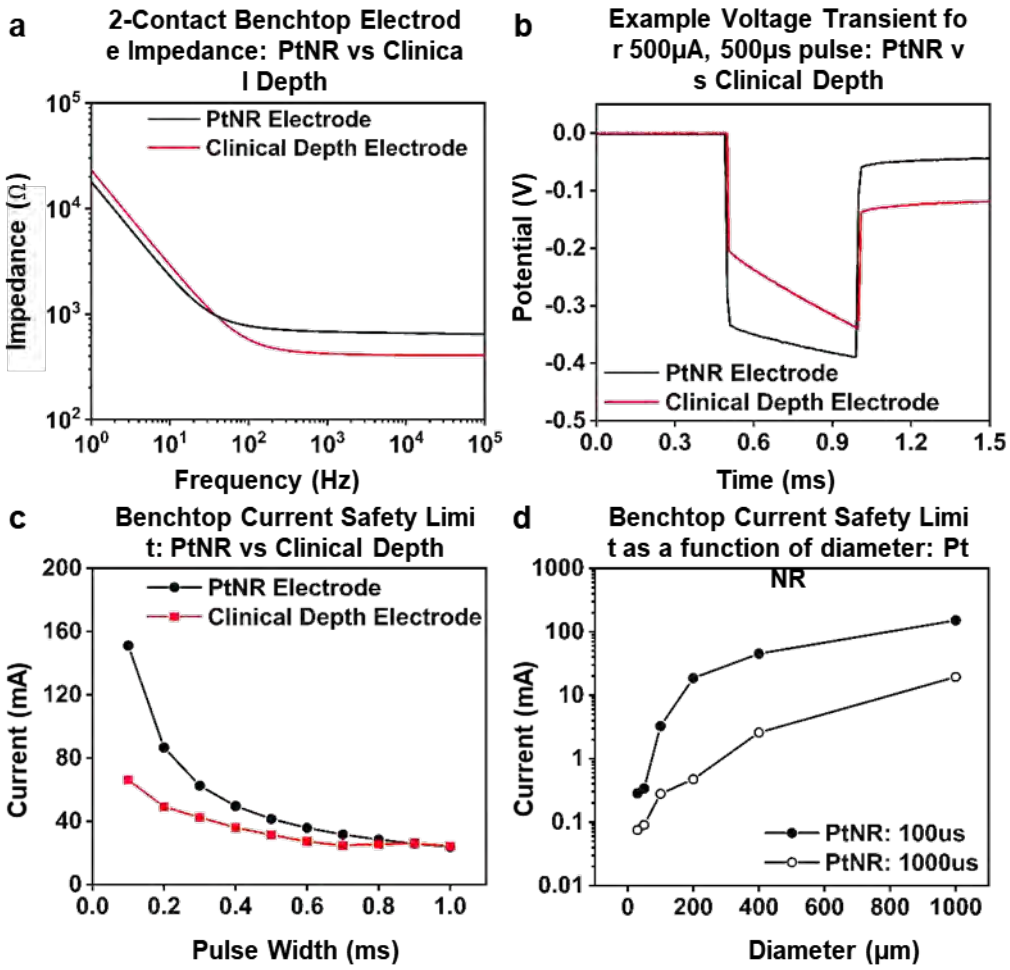

Supplementary Fig. 26. Electrochemical characterization of an AdTech Medical Spencer depth that is 1.12 mm diameter with contacts that are 2.41 mm long and 5 mm spaced and a PtNR electrode with 1 mm diameter during stimulation. (**a**) Two-contact electrochemical impedance spectra (where another contact is used as both ground and reference to simulate impedances that appear in bipolar stimulation). The PtNR contact with 28.8 times smaller area than the PMT electrode exhibited higher capacitance and therefore lower reactance than the PMT electrode. The 1 kHz impedance that is typically overwhelmed with series resistances of metallization traces for macro-contacts is larger of the PtNR contact than the PMT electrode. (**b**) Example voltage transient across the two types of electrodes, exhibiting a lower potential drop across the electrode-tissue interface (non-instantaneous potential drop) for the PtNR contact compared to the PMT depth contact. (**c**) Benchtop electrochemical safety limits for the two types of electrodes when tested in the bipolar configuration (see ref. [28] for methods), showing superior performance for the PtNR contact, particularly at small pulse widths. (**d**) The benchtop electrochemical safety limits for two pulse widths for the PtNR contacts as a function of contact diameter.

Supplementary Video 1. Movement of the implanted short thin film μSEEG relative to the brain. The electrode is shown before and after insertion, where the short depth was inserted into brain tissue and activity was recorded for a short period of time. The gauze and other stabilizing features are largely for the ribbon cables which form the connections, but the thin film components (which are largely transparent and flexible) move with the brain tissue movements in the craniotomy.

Supplementary Table 1. Comparison of the electrode form factor with previously reported studies using rolled solutions. (D: diameter, Parylene: Parylene C, EIROF: electrodeposited iridium oxide film, PEDOT: PEDOT:PSS, PtNR: Platinum nanorods.)

	Total channel count	Metal lead spacing	Electrode site size & material	Impedance (kΩ) @ 1 kHz	Probe material	Probe shape	Subject, implant site
van der Puije et al. (1989)	9	N/A	890 μm x (1370 ~ 2180 μm), Pt	~ 1	Polyimide/ silicone rubber	Rolled (cylindrical)	N/A (benchtop)
Kang et al. (2015)	20	N/A	D: 100 μm, EIROF on Pt	1.941 - 2.026	Parylene	Rolled (self-closed)	Rat, sciatic nerve
Pothof et al. (2016)	32, 64 (prototype: 128)	N/A	D: 35 μm, Pt	354 ± 31	Polyimide	Rolled (cylindrical)	NHP, cortex
This work (2023), PEDOT	32, 64	3 μm	D: 20 μm, PEDOT on Pt	35.0 ± 3.7	Parylene, polyimide	Inflatable sheath	Rat/NHP/ pig/human, cortex
This work (2023), PtNR	32, 128	3 μm	D: 30 μm, PtNR	94.0 ± 2.6	Polyimide	Inflatable sheath	Rat/NHP, cortex

Supplementary Table 2. Electrode usage and species tested. Sp. – species, NHP-Non-Human primate, PEDOT-PEDOT:PSS, PI-Polyimide, PC-Parylene C.

label	Sp.	Brain region	Electrode	PEDOT or PtNR	PI or PC	Acute or chronic
HS1	Human	Left anterior temporal lobe	Short 64 channel µSEEG	PEDOT	PC	Acute
HS2	Human	Left anterior temporal lobe	Short 64 channel µSEEG	PEDOT	PI	Acute
MM1	NHP	Visual cortex	Short 64 channel µSEEG	PEDOT	PC	Acute
MM1	NHP	Visual cortex	Surface µECoG	PtNR	PC	Acute
MM1	NHP	Visual cortex	Surface µECoG	PEDOT	PC	Acute
MM2	NHP	Parietal lobe/dlPFC and auditory cortex	Long µSEEG	PtNR	PI	Acute
MM2	NHP	Parietal lobe/dlPFC and auditory cortex	Tungsten electrode	-	-	Acute
RN1	Rat	Near barrel cortex	Short 32 channel µSEEG	PEDOT	PI	Chronic
RN2	Rat	Near barrel cortex	Short 32 channel µSEEG	PEDOT	PI	Chronic
RN3	Rat	Near barrel cortex	Short 32 channel µSEEG	PEDOT	PI	Chronic
RN4	Rat	Near barrel cortex	Short 32 channel µSEEG	PtNR	PI	Chronic
RN5	Rat	Near barrel cortex	Short 32 channel µSEEG	PtNR	PI	Chronic
RN6	Rat	Near barrel cortex	Short 32 channel µSEEG	PtNR	PI	Chronic
RN7	Rat	Near barrel cortex	Short 32 channel µSEEG	PtNR	PI	Chronic

RN8	Rat	Barrel cortex	Short 32 channel µSEEG	PtNR	PI	Chronic
RN9	Rat	Barrel cortex	Short 32 channel µSEEG	PtNR	PI	Chronic
RN10	Rat	Near barrel cortex	Short 64 channel µSEEG	PEDOT	PI	Acute
RN10	Rat	Near barrel cortex	Surface µECoG	PEDOT	PC	Acute
SS1	Pig	Brain	Short 64 channel µSEEG	PEDOT	PC	Acute
SS2	Pig	Brain	Short 64 channel µSEEG	PEDOT	PI	Acute
SS2	Pig	Brain	Surface µECoG	PEDOT	PC	Acute
SS3	Pig	Brain	Short 64 channel µSEEG	PEDOT	PI	Acute
SS3	Pig	Brain	sEEG electrode	-	-	Acute
SS3	Pig	Brain	Surface µECoG	PEDOT	PC	Acute

Supplementary Table 3. Electrode details.

Electrode	Number of channels	Diameter (µm)	Center to center spacing (µm)	Recording length (mm)	PEDOT:PSS or PtNR	Polyimide (PI) or parylene C (PC)
Short 32 channel µSEEG	32	30	60	1.89	PEDOT:PSS, PtNR	PI
Short 64 channel µSEEG	64	20	60	3.80	PEDOT:PSS	PI, PC
Long µSEEG	128	30	60	7.65	PtNR	PI
Surface µECoG	32 x 2	20	100	3.12	PEDOT:PSS	PC

5

1. Kozai, T.D.Y. & Kipke, D.R. Insertion shuttle with carboxyl terminated self-assembled monolayer coatings for implanting flexible polymer neural probes in the brain. *Journal of neuroscience methods* **184**, 199-205 (2009).
2. Buzsáki, G., Anastassiou, C.A. & Koch, C. The origin of extracellular fields and currents—EEG, ECoG, LFP and spikes. *Nature reviews neuroscience* **13**, 407-420 (2012).
3. Khodagholy, D. et al. NeuroGrid: recording action potentials from the surface of the brain. *Nature neuroscience* **18**, 310-315 (2015).
4. Ganji, M. et al. Selective formation of porous Pt nanorods for highly electrochemically efficient neural electrode interfaces. *Nano letters* **19**, 6244-6254 (2019).
5. Tchoe, Y. et al. Human brain mapping with multithousand-channel PtNRGrids resolves spatiotemporal dynamics. *Science translational medicine* **14**, eabj1441 (2022).
6. Khodagholy, D. et al. Organic electronics for high-resolution electrocorticography of the human brain. *Science Advances* **2**, e1601027 (2016).
7. Atay, S.M., Kroenke, C.D., Sabet, A. & Bayly, P.V. Measurement of the dynamic shear modulus of mouse brain tissue in vivo by magnetic resonance elastography. (2008).
8. Hukins, D., Mahomed, A. & Kukureka, S. Accelerated aging for testing polymeric biomaterials and medical devices. *Medical engineering & physics* **30**, 1270-1274 (2008).
9. Hermiz, J. et al. in 2016 38th Annual International Conference of the IEEE Engineering in Medicine and Biology Society (EMBC) 4511-4514 (IEEE, 2016).
10. Bakker, R., Tiesinga, P. & Kötter, R. The scalable brain atlas: instant web-based access to public brain atlases and related content. *Neuroinformatics* **13**, 353-366 (2015).
11. Calabrese, E. et al. A diffusion tensor MRI atlas of the postmortem rhesus macaque brain. *Neuroimage* **117**, 408-416 (2015).
12. Ephys, O. an open-source, plugin-based platform for multichannel electrophysiology; JH Siegle, AC López, YA Patel, K Abramov, S Ohayon, J Voigts. *Journal of Neural Engineering*.
13. Paulk, A.C. et al. Microscale physiological events on the human cortical surface. *Cerebral Cortex* **31**, 3678-3700 (2021).
14. Yang, J.C. et al. Microscale dynamics of electrophysiological markers of epilepsy. *Clinical Neurophysiology* **132**, 2916-2931 (2021).
15. Buračas, G.T. & Boynton, G.M. Efficient design of event-related fMRI experiments using M-sequences. *Neuroimage* **16**, 801-813 (2002).
16. Tabuchi, H. et al. Study of the visual evoked magnetic field with the m-sequence technique. *Investigative ophthalmology & visual science* **43**, 2045-2054 (2002).
17. Dykstra, A.R. et al. Widespread brain areas engaged during a classical auditory streaming task revealed by intracranial EEG. *Frontiers in human neuroscience* **5**, 74 (2011).
18. Oostenveld, R., Fries, P., Maris, E. & Schoffelen, J.-M. FieldTrip: open source software for advanced analysis of MEG, EEG, and invasive electrophysiological data. *Computational intelligence and neuroscience* **2011** (2011).
19. Chang, J.-Y. et al. Multivariate autoregressive models with exogenous inputs for intracerebral responses to direct electrical stimulation of the human brain. *Frontiers in human neuroscience* **6**, 317 (2012).
20. Mitzdorf, U. Current source-density method and application in cat cerebral cortex: investigation of evoked potentials and EEG phenomena. *Physiological reviews* **65**, 37-100 (1985).
21. Pettersen, K.H., Devor, A., Ulbert, I., Dale, A.M. & Einevoll, G.T. Current-source density estimation based on inversion of electrostatic forward solution: effects of finite extent of neuronal activity and conductivity discontinuities. *Journal of neuroscience methods* **154**, 116-133 (2006).
22. Westover, M.B. et al. Real-time segmentation of burst suppression patterns in critical care EEG monitoring. *Journal of neuroscience methods* **219**, 131-141 (2013).
23. Pachitariu, M., Steinmetz, N.A., Kadir, S.N., Carandini, M. & Harris, K.D. Fast and accurate spike sorting of high-channel count probes with KiloSort. *Advances in neural information processing systems* **29** (2016).
24. Jia, X. et al. High-density extracellular probes reveal dendritic backpropagation and facilitate neuron classification. *Journal of neurophysiology* **121**, 1831-1847 (2019).
25. Shi, Y., Kirwan, P. & Livesey, F.J. Directed differentiation of human pluripotent stem cells to cerebral cortex neurons and neural networks. *Nature protocols* **7**, 1836-1846 (2012).

26. Deshpande, A., Mina, E., Glabe, C. & Busciglio, J. Different conformations of amyloid β induce neurotoxicity by distinct mechanisms in human cortical neurons. *Journal of Neuroscience* **26**, 6011-6018 (2006).
27. Miskinyte, G. et al. Direct conversion of human fibroblasts to functional excitatory cortical neurons integrating into human neural networks. *Stem cell research & therapy* **8**, 1-18 (2017).
28. Vatsyayan, R., Cleary, D., Martin, J.R., Halgren, E. & Dayeh, S.A. Electrochemical safety limits for clinical stimulation investigated using depth and strip electrodes in the pig brain. *Journal of Neural Engineering* **18**, 046077 (2021).